UNIVERSIDAD COMPLUTENSE DE MADRID
FACULTAD DE CIENCIAS FÍSICAS

TESIS DOCTORAL

Desintegración β del 8B a los estados excitados del 8Be: contribuciones en mezcla de isospín y halo de protón

β-decay of 8B into highly excited states of 8Be: Isospin mixing and proton-halo contributions

MEMORIA PARA OPTAR AL GRADO DE DOCTOR

PRESENTADA POR

Sílvia Viñals i Onsès

Directores

Olof Tengblad
Enrique Nácher

Madrid

UNIVERSIDAD COMPLUTENSE DE MADRID

FACULTAD DE CIENCIAS FÍSICAS

TESIS DOCTORAL

Desintegración β del 8B a los estados excitados del 8Be: Contribuciones en mezcla de isospín y halo de protón

β-decay of 8B into highly excited states of 8Be: Isospin mixing and proton-halo contributions

MEMORIA PARA OPTAR AL GRADO DE DOCTOR

PRESENTADA POR

Sílvia Viñals i Onsès

DIRECTOR

Olof Tengblad
Enrique Nácher

Universidad Complutense de Madrid

Facultad de Ciencias Físicas

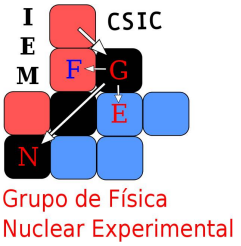

Tesis Doctoral

Desintegración β del ^{8}B a los estados excitados del ^{8}Be:
Contribuciones en mezcla de isospín y halo de protón

β-decay of ^{8}B into highly excited states of ^{8}Be:
Isospin mixing and proton-halo contributions

Memoria para optar al grado de Doctor
Presentada por

Sílvia Viñals i Onsès

Directores

Prof. Olof Tengblad
Dr. Enrique Nácher

In a dream, you can cheat architecture into impossible shapes. That lets you create closed loops, like the Penrose Steps. The infinite staircase. A closed loop like this helps you disguise the boundaries of the dream you've created.

Inception, 2010

Per a tots els que s'han esquitxat d'aquest somni.

ACKNOWLEDGEMENT

The main important thing when doing a thesis is all the people next to you that helps, teaches and guides you during this process. Of course, this must be recognised, so let me start and forgive me for the changes in the language.

Me gustaría empezar agradeciendo el gran esfuerzo de mis directores, Olof y Kike. Olof, gracias por haberme dado la oportunidad de empezar con esto hace tres años y medio. Gracias por los consejos, por las explicaciones y por las reuniones discutiendo sobre la electrónica y el análisis. Gracias, también, por ser un apoyo cuando, por ejemplo, durante el experimento la presión pudo conmigo. Espero que esto que entrego hoy llegue a la altura de lo esperado.

Kike, la verdad es que no sé ni como empezar. Has sido mi director, mi apoyo, mi amigo, mi referente y mi consejero. Me faltarían páginas para agradecerte todo lo que has hecho por mí, ya no solo en estos últimos meses, sino desde que decidiste involucrarte y ayudarme a sacar fuerzas de donde ya no había. Gracias por las mil y una correcciones (y prefiero ponerlo así que contar las miles de correcciones) de estos últimos meses. Gracias por preocuparte, por los fines de semana trabajando, por dejarme crecer y desarrollarme. Gracias por darme la oportunidad de dirigir un trabajo de grado contigo en la sombra, por pensar siempre en lo mejor para mí. Gracias por los skypes de *charleta*. Podría seguir pero no acabaría, así que mejor lo dejo aquí y te invito a una cena el próximo día que vengas.

No solo mis directores han ayudado. Gracias, María José, por aconsejar y enseñar. Por tu experiencia y por siempre tener el paper adecuado para todas las dudas. Gracias por leerte y corregir esta tesis y por el apoyo en los momentos cruciales de este periodo. Me has enseñado a ser crítica y dudar de todo, a revisar las cosas y a estar segura de cada paso, cualidades muy importantes en investigación.

Thanks to our friends and collaborators in Aarhus: Karsten, Hans, Michael, Jesper and Andreas. Thanks for the physics talks, always productive and illuminating. Thanks for being always there in the distance, answering an email and reading reports. Especially, I would like to thank Andreas, who always have

been available for my hundred questions about how to proceed with ORM.

Thanks to all the marvellous people that I met at CERN. I'm sure I will not be able to write all your names here, but thanks for the welcoming and including me in all your works and plans. Most of you became more than colleagues.

Por supuesto no me olvido de los de aquí. Para empezar: gracias, Javi. Me has aguantado en el despacho, cantando en silencio y arreglándome la silla cada día. Has sido un apoyo, un amigo y mi persona favorita para ir de conciertos. Esto no se acaba, pero me pongo sentimental y voy a echar de menos desayunar contigo (entre otras muchas cosas). No me despido porque he tenido la suerte de que seas mi amigo y sé que nos veremos este fin de semana para unas cañas (aplicable a cualquier semana). Briz, ¡ha sido increible trabajar contigo! Siempre dispuesto a ayudar, con una sonrisa y con una implicación absoluta por todo. Para mí, ha sido todo un placer compartir este último año contigo y he aprendido muchísimo. Aunque ya no estéis porque hayáis volado, gracias Irene y Víctor. Me acogisteis al llegar al grupo como una más y espero que podamos celebrar mi final de tesis como celebramos el vuestro.

Gracias a mis (dejadme que me tome la licencia) GFNitos. Habéis sido iluminadores, todos vosotros, sobre todo (aunque no solo) en este último periodo. Gracias por incluirme y dejarme ser una más del grupo. Después de tres años, creo que puedo decir que he encontrado mi sitio en Madrid.

Gracias Víctor, por haber sido, en los primeros años, el motor impulsor de esto. Siempre positivo y nunca dejando que me rindiera. Sería hipócrita no agradecer tu aportación a este proyecto.

Gràcies familia. Sempre ploro quan em toca agrair-vos algo. Mama, Papa, gràcies per ser sempre el vent que impulsa les meves veles. Gràcies per animar sempre, incondicionalment. Gràcies per tot el que m'heu ensenyat i deixeu-me agrair-vos, per avançat, tot el que encara em queda per aprendre de vosaltres. Sempre esteu i sempre estareu. Tot aquest esforç és per a vosaltres. Pati, si els papes han estat el vent, tu has estat el timó. Gràcies per sempre estar, per sempre animar, per sempre lluitar per mi. Sempre has estat el meu referent i ho seguiràs sent per molt lluny que estem. Ferran, has estat sempre per qualsevol cosas que he necessitat. Gràcies per riure sempre, de mi i amb mi, per treure ferro a les coses que a mi em capficaven massa. Gràcies per obrir-me sempre les portes de casa teva. Als meus nebots, en especial a la Blanca. Gràcies petits

meus per estimar-me en la distància. Als meus cunyats, Javi i Mary, gràcies per tot, per sempre ser-hi també. Us estimo a tots!

Por último, te he dejado a ti. Gracias Fer. Cualquier cosa que te diga o te escriba no va a llegar a agradecerte ni una milésima de lo que has hecho por mí. Eres mi apoyo diario, siempre atento, siempre pendiente. Este final de tesis no sabría decir quién lo ha gestionado mejor, si tu o yo, aunque por mi parte no imagino haberlo hecho sin ti. Esto se queda corto, lo sé, pero también sé que pesan más los actos que las palabras. Te quiero.

Gracias a todos.
Gràcies a tots.
Thank you.

Contents

List of Tables

List of Figures

Abstract

This thesis work deals with the study of the decay of the proton-halo nucleus ^{8}B. The data were obtained in an experiment performed at ISOLDE@CERN. The goal of this study is to determine the β-strength to highly excited states of ^{8}Be. Of particular interest is the isospin mixing of the 2^{+} doublet at 16.6 and 16.9 MeV excitation energy. The β-decay process is the only one that allows to simultaneously address the two isospin components of the states (T=1 and T=0). This has not been measured before. Also, the second objective is the so far unobserved electron-capture delayed-proton-emission branch expected to proceed via the 17.6 MeV state. The states of interest are unbound. After the β-decay: the doublet in ^{8}Be breaks up into two α and the 17.6 MeV state in ^{8}Be preferentially decays via proton emission to ^{7}Li.

We have measured α-α coincidences from the break-up of ^{8}Be with a compact detector set-up comprised of 5 DSSD detectors, 4 of them backed by a Silicon pad to perform particle identification. We have corrected the α-α spectrum for different effects and it has been analysed within the R-matrix formalism. In addition, we have implemented a technique to unfold alpha spectra.

From the R-matrix analysis we have estimated the isospin mixing of the two aforementioned states, it was found that each of the states has almost 50% mixture of isospin T=0 and T=1. Furthermore, using Monte Carlo simulations and a thorough analysis of the low part of the spectrum, we have been able to establish an experimental upper limit for the proton decay branch of 2.5×10^{-6} with a confidence level of 99.9%, improving the existing limit by a factor of ten.

Introduction 1

The structure of a nucleus is tightly related with the interaction between the nucleons that conform the nucleus and their time evolution. The latter allows to differentiate between stable and unstable nuclei. The stable nuclei are those that have enough binding energy to keep together all the nucleons permanently or during a large time interval. Primordial nuclei are those that existed in their current form before the Earth was formed, for example 4.5 billion years ago. The unstable nuclei are also called radioactive nuclei. The non-stability implies that after a certain time, the nucleus suffers a change of nucleon (protons and neutrons) configuration or undergo a change in energy or both towards a more bound system.

The different mechanisms for the nuclei to evolve towards the valley of stability are the so called decay modes and can be:

- β-decay (explained in detail in the following).
- Fission; where the nucleus breaks in two parts while evaporating 1 or more neutrons.
- Emission of a particle as proton, neutron, α-particle...

With each decay mode, the nucleus becomes more stable and, therefore, comes closer to the valley of the stability. The Segré chart (Fig. 1.1) shows, in a 2-dimension plot, the proton (Z) versus neutron (N) number of all nuclei according to our present knowledge. The different decay modes are indicated by

color-code, being the stable nuclei in black, in pink the β^-, in blue the β^+/EC, in yellow the α-decay, in orange the proton emission, in purple the neutron emission and in green the spontaneous fission. Most of the nuclei are radioactive through β-decay (β^+/EC or β^- depending of the proton/neutron ratio) and, for heavy nuclei, the α emission and nuclear fission start to be the dominant decay modes.

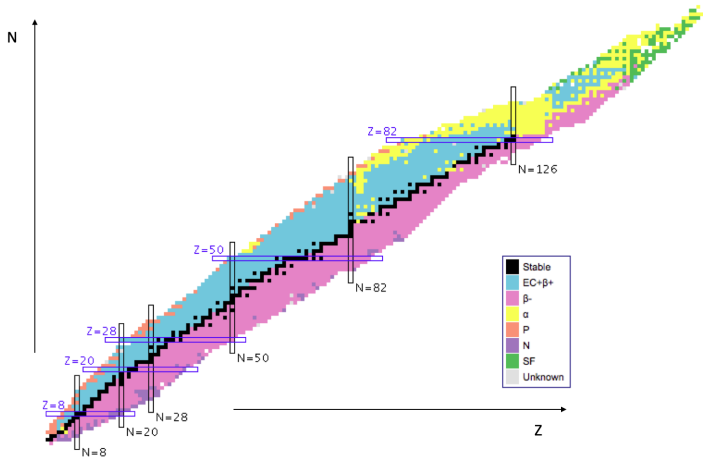

Figure 1.1: The Segré chart where all the known nuclei are display in a proton number (Z) versus neutron number (N) plot. Each decay mode is indicated by a colour.

In the following, the details of the β-decay process will be explained as it is the decay mode that occurs in the nucleus of this study: the ^{8}B.

1.1 β-DECAY PROCESS

The β-decay process occurs inside a nucleus. It implies that one of the nucleons suffers a transformation into the other type of nucleon. The possible transformation, then, is from a neutron to a proton or vice-versa. When a nucleus suffers a change of a neutron to a proton, an electron and a neutrino are emitted and the process is called β^-. This process can occur in vacuum for a free neutron. For the proton to neutron decay, two competitive process can

occur: the emission of a positron, process called β^+, and the capture of an electron from the inner atomic shell (EC). Each of these processes can be described as the following, where ${}^A_Z X_N$ is a certain nucleus:

$$\beta^- : \quad {}^A_Z X_N \rightarrow {}^A_{Z+1} X'_{N-1} + e^- + \bar{\nu} \tag{1.1}$$

$$\beta^+ : \quad {}^A_Z X_N \rightarrow {}^A_{Z-1} X'_{N+1} + e^+ + \nu \tag{1.2}$$

$$EC : \quad {}^A_Z X_N + e^- \rightarrow {}^A_{Z-1} X'_{N+1} + \nu \tag{1.3}$$

Each of these exothermic processes has associated a certain quantity of energy available to be released, the Q-value. In the decay process, the energy released will always be equal or lower than the Q-value. For each decay mode, the Q-value depends on the difference in mass balance and it is defined in terms of the atomic mass:

$$Q_{\beta^-} = [M({}^A_Z X_N) - M({}^A_{Z+1} X'_{N-1})]c^2 \tag{1.4}$$

$$Q_{\beta^+} = [M({}^A_Z X_N) - M({}^A_{Z-1} X'_{N+1})]c^2 - 2m_{e^-}c^2 \tag{1.5}$$

$$Q_{EC} = [M({}^A_Z X_N) - M({}^A_{Z-1} X'_{N+1})]c^2 - B_e \tag{1.6}$$

where m_{e^-} is the mass of the electron and B_e is the binding energy of the atomic shell from where the electron is captured. The three processes are energetically allowed within the respective Q-windows. As far as the β^- is concerned, the Q-window is defined by the atomic masses of the daughter and the parent nuclei. As for EC, the binding energy term of an electron with the atomic shell is in the order of few keV, and compared to the difference in atomic masses can be neglected. In the case of β^+, the difference in mass between the parent and the daughter nucleus must be larger than twice the electron mass at rest: 1022 keV.

The energy released in the decay process is calculated subtracting the excitation energy of the daughter nucleus to the Q-value. This energy is shared by the outgoing particles (β-particle and neutrino) and the recoiling of the daughter nucleus, so for the β-decay, since the final state is made up of three particles, the electron (or positron) spectrum is a continuous distribution ranging from zero up to the maximum available energy.

In this thesis we have studied the decay of ^{8}B. Due to the proton-to-neutron ratio, this nucleus gains stability by decaying via β^+/EC. Therefore, from now

on, when we mention the β-decay of ^{8}B we will be always referring to β^+/EC decay.

1.1.1 Selection rules

The β-decay process is one of the many facets of the weak interaction. In the following, the possible changes in parity ($\Delta\pi$) and angular momentum (ΔJ) for a general β-decay process (β^+ or β^-) are shown, where l and s are the angular momentum and the spin of the outgoing particles: e for the electron/positron and ν for the neutrino/antineutrino.

$$\Delta J = l_e + l_\nu + s_e + s_\nu = l_\beta + s_\beta \tag{1.7}$$

$$\Delta\pi = (-1)^{l_e+l_\nu+s_e+s_\nu} = (-1)^{l_\beta+s_\beta} \tag{1.8}$$

Let us consider the β^+-decay, the spin of a positron is $1/2$ so it can only couple with the neutrino with parallel or anti-parallel spins. This allows to classify the transition mode being Fermi if anti-parallel ($S_\beta = 0$) and Gamow-Teller if parallel ($S_\beta = 1$). Both modes are the most favourable ones and a β-decaying source may produce a mixture of relative spins.

The transition can also be classified depending on the orbital angular momentum of the outgoing particles. The most likely, and therefore most probable to be observed, transition is the one where the outgoing particles carry zero angular momentum. These transitions are called *allowed transitions*. When the outgoing angular momentum is different from zero, the transitions are called *forbidden transitions*, less probables than the allowed ones. They are classified as first forbidden, second forbidden and so on depending on the units of angular momentum that is taken by the emitted particle.

Moreover, nuclei have one more quantum number called isospin (T_z) which was introduced to distinguish between proton and neutron in absence of Coulomb and weak interaction. The eigenstates of the isospin operator are defined as a spin vector where being a proton or a neutron are possible states of a general particle called nucleon. Arbitrarily choosing a z-axis, the neutrons are defined by its isospin projection as $T_z = +1/2$ and the protons as $T_z = -1/2$[1]. For

[1]This definition follows the usual convention for Nuclear Physics [BM69]

a certain nucleus with N neutrons and Z protons, the third component of the isospin vector is calculated for the ground state as follows (expressed in $\hbar$ units):

$$T_z = \frac{1}{2}(N - Z) \tag{1.9}$$

and then, for a β-decay, $\Delta T_z = \pm 1$. The isospin of the ground state is defined as T=$|T_z|$

All these conditions are called selection rules and are summarised in Tab. 1.1.

Table 1.1: Selection rules of β-decay. ΔJ is the change in angular momentum for Fermi and Gamow-Teller (GT) modes, l_β the angular momentum carried out by the outgoing particles and ΔT_z the third component of the isospin vector. $\Delta\pi$ is the parity.

Transition	ΔJ_{Fermi}	ΔJ_{GT}	l_β	$\Delta\pi$	ΔT_z
Allowed	0	0, $\pm$1 (except 0→0)	0	0	$\pm$1
First Forbidden	0, $\pm$1	0, $\pm$1, $\pm$2 (except 0→0)	1	1	$\pm$1
Second Forbidden	$\pm$1,$\pm$2	$\pm$1, $\pm$2, $\pm$3	2	0	$\pm$1

1.1.2 The Fermi theory

The Fermi theory [Fer34] of β-decay was developed in 1934 to calculate the transition probability (λ) caused by a weak interaction that forms quasi-stationary states. It starts from the general expression of Fermi's Golden rule:

$$\lambda = \frac{2\pi}{\hbar}|V_{fi}|^2\rho(E_f) \tag{1.10}$$

where $\rho(E_f)$ is the density of final states and V_{fi} is the matrix element of the interaction V between the initial and the final quasi-stationary states, which can be rewritten for the particular case of β-decay as:

$$V_{fi} = \int \psi_f^* V \psi_i du = g \int [\psi_f^* \phi_e^* \phi_\nu^*] O_X \psi_i du \tag{1.11}$$

being ϕ_e and ϕ_ν the wave functions of the electron[2] and neutrino, O_X one of the five mathematical operators and g a constant value that represents the strength of the interaction. In the Fermi theory framework, O_X adopts the form of V-A, where V stands for polar vector operator and A stands for axial vector operator.

The electron and antineutrino wave functions take the form of a free-particle normalized within the volume V:

$$\phi_e(r) = \frac{1}{\sqrt{V}} e^{i\mathbf{p}\cdot\mathbf{r}/\hbar} \tag{1.12}$$

$$\phi_\nu(r) = \frac{1}{\sqrt{V}} e^{i\mathbf{q}\cdot\mathbf{r}/\hbar} \tag{1.13}$$

In the allowed transitions (or allowed approximation) only the first term of the Taylor's expansion of the exponential part is kept, as the only factors that depend on the electron or antineutrino energy come from the density of states. Knowing this, the partial decay rate (from Eq. 1.10) is rewritten as follows:

$$d\lambda = \frac{2\pi}{\hbar} g^2 |M_{fi}|^2 (4\pi)^2 \frac{p^2 q^2}{h^6} \frac{dpdq}{dE_f} \tag{1.14}$$

where $M_{fi} = \int \psi_f^* O_X \psi_i du$ is the nuclear matrix element. For the forbidden transitions, higher order terms in the Taylor expansion must be added. The degree to which a transition is forbidden is determined by how far the expansion of the plane wave must go to find a non-vanishing nuclear matrix element. For the allowed transition, the transition rates for both Fermi and Gamow-Teller can be written as:

$$B_F = |<\psi_f| \sum_{k=1}^{A} \tau_k^{\pm} |\psi_i>|^2 \equiv <\tau>^2 \tag{1.15}$$

$$B_{GT} = |<\psi_f| \sum_{k=1}^{A} \vec{\sigma_k} \tau_k^{\pm} |\psi_i>| \equiv <\sigma\tau>^2 \tag{1.16}$$

where $\tau^{\pm}$ is the operator that rises (β^+) or lowers (β^-) the isospin in the interaction and σ is the Pauli spin operator which produces a change in angular

[2]For simplicity, only electron and antineutrino will be written but the same reasoning applies for positron and neutrino

momentum. Eq. 1.15 and Eq. 1.16 are commonly named Fermi and Gamow-Teller strength or reduced transition probabilities as do not depend on the phase space available in the final state. For a general decay, with a mixing of Fermi and Gamow-Teller modes, the operator is written as a lineal combination of both transition rates including the coupling constants G_V from the polar vector and G_A from the axial vector.

$$B_\beta = G_V^2 B_F + G_A^2 B_{GT} = G_V^2 (B_F + g_a^2 B_{GT}) \tag{1.17}$$

In order to integrate Eq. 1.14 over all the possible states, the quantity called Fermi integral is defined. This quantity includes the function $F(Z, E_e)$ which is related to the absolute square of the Coulomb wave function at the origin and defines the kinematic of the decay (see chapter 5 of [Won99] for more details):

$$\begin{aligned} f(Z, E_0) &= \frac{1}{(m_e c)^3 (m_e c^2)^2} \int_0^{p_{max}} F(Z,p) p^2 q^2 dp = \\ &= \frac{1}{(m_e c)^3 (m_e c^2)^2} \int_0^{p_{max}} F(Z,p) p^2 (E_0 - E_e)^2 dp \end{aligned} \tag{1.18}$$

With the Fermi integral, λ can be rewritten as

$$\lambda = \frac{g^2 |M_{fi}|^2}{2\pi^3 \hbar^7 c^3} (m_e c)^3 (m_e c^2)^2 f(Z, E_0) \tag{1.19}$$

and from the transition probability (λ), the expression of the half-life for a β-decay is obtained:

$$T_{1/2} = \frac{ln2}{\lambda} = \frac{1}{f(Z, E_0)} \frac{2\pi^3 \hbar^7}{m_e^5 c^4} \frac{ln2}{B(\beta)} \tag{1.20}$$

Often the β-decay rates are not given by half-lives but in terms of ft-values, which is the product of the Fermi integral $f(Z, E_0)$ and the comparative half-life t. This quantity is a more meaningful physical quantity in β-decay studies as it is directly related to the square of the nuclear transition matrix element. However, for the study of the ^8B β-decay, this is not a useful magnitude due to the width of the resonance as will be explained in Sec. 5.4.

$$ft = \frac{K}{B_F + g_a^2 B_{GT}} \tag{1.21}$$

where the vector coupling constant G_V is included with the other universal constants into the K constant:

$$K = \frac{2\pi^3 \hbar^7 ln2}{m_e^5 c^4 G_V^2} = 6143.6(17)s \quad \text{[HT09]} \tag{1.22}$$

From the measured value of the K constant, the value of G_V and then g_a can be obtained. This was obtained from superallowed decays (purely Fermi decays $0^+ \rightarrow 0^+$ with the same isospin) after applying such corrections as the finite size and the charge distribution of the nucleus.

$$G_V = 1.41556(74) \times 10^{-62} Jm^3 \tag{1.23}$$

$$g_a = \frac{G_A}{G_V} = -1.2695(29) \quad [\text{YAA}^+06] \tag{1.24}$$

1.2 THE β^+/EC DECAY OF ^{8}B

In this section, the motivation to study the ^{8}B and ^{8}Be nuclei and the advantages of doing it through the β^+ mechanism will be presented.

The β^+/EC-decay of ^{8}B is one of the steps in the hydrogen-burning processes that takes place in the sun and, moreover, this decay is the main source of high-energy solar neutrinos, above 2 MeV. For this reason, ^{8}B has been studied in detail as it is the largest contributor to the so-called "solar neutrino problem": the measured flux of solar neutrinos [DJHH68] was too small compared to the predictions of the solar model [BCDJR85], being the seed to discover the neutrino flavour oscillation [RSP80]. The main contribution to the neutrino spectrum comes from the decay to the 3 MeV level therefore it has been massively studied. In this work, we will not enter into this topic, since our aim is not to obtain the neutrino spectrum but the nuclear structure of the daughter nucleus.

Apart from the astrophysical interest, the β^+-decay of ^{8}B gives access to the nuclear structure of ^{8}Be. The ^{8}Be nucleus has a sort of continuum of 2^+ states due to a broad resonance at 3 MeV, which has been, for many years, subject of R-matrix analysis [Bar69]. The two states at 16.6 and 16.9 MeV form a 2^+ doublet being the only case in Nuclear Physics in which one can expect more than a few percent of isospin mixing. Moreover, ^{8}Be presents an α-α cluster structure. All this aspects of the nuclear structure of ^{8}Be are detailed in the next subsection (Sec. 1.2.3).

In addition, from the nuclear perspective ^{8}B is also interesting. The ^{8}B nucleus is the only nucleus known for showing a proton-halo configuration in its ground state, which is one of the types of halo nucleus. The discussion about this type of exotic nucleus can be found in Sec. 1.2.2.

But before we start discussing theses points, the decay scheme of the ^{8}B nucleus into the ^{8}Be is presented in Fig. 1.2. The Q_{EC} of the β-decay of the ^{8}B nucleus is calculated using Eq. 1.6 and the mass excess of the nucleus form [WAW$^+$12] being the result what follows.

$$Q_{EC} = M(8,5) - M(8,4) = \Delta M(8,5) - \Delta M(8,4) = 17979.9(10)keV \quad (1.25)$$

where $\Delta M(^8B) = 22921.6(10)keV$ and $\Delta M(^8Be) = 4941.67(4)keV$.

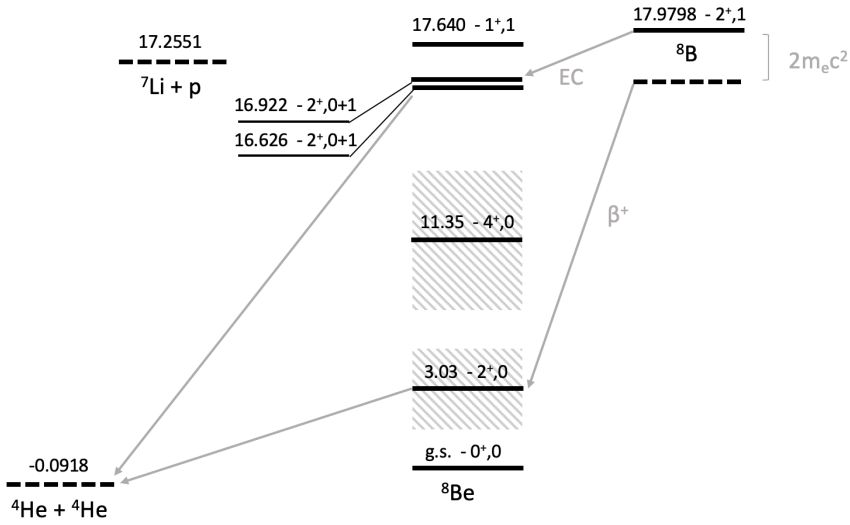

Figure 1.2: Decay scheme of the ^{8}B nucleus into the ^{8}Be. Each level is labelled with the energy above the ^{8}Be ground state in MeV. The spin, parity and isospin are written in the standard way: J^π, T. The energies and quantum numbers are from [Tea04].

As a starting point, first the experimental measurements of the β-decay of ^{8}B will be presented. In the following subsections, the different parts of the decay scheme will be referred and explained.

1.2.1 Historical background of ^{8}B β-decay experiments

The first experimental study of the β-decay of the ^{8}B nucleus was done by Gilbert in 1954 [Gil54]. This experiment was focused on measuring for the first time the range distribution of the α particles of ^{8}B and the already measured ^{8}Li. It was motivated by the large number of tracks of these isotopes when bombarding beryllium with 375 MeV α particles and had two purposes: to check the similarity of the two mirror nuclei and to search for a possible new level in

the excited ^{8}Be nucleus. The results were extrapolated from 100 ^{8}B disintegrations and conclude that roughly 15% of the decays found should be explained by higher excitation-levels in the ^{8}Be nucleus, above the well-known 3 MeV state.

Six years later, Farmer et al. [FC60] performed a new experiment to measure with more statistics and precision, the α-spectra from the decays of ^{8}Li and ^{8}B. In this experiment, the technique was improved compared to the previous experiment and 2×10^4 α-particles from the ^{8}B decay were identified in the range from 1 to 15 MeV. From these results, it was confirmed the symmetry in the decay schemes of the mirror nuclei (^{8}Li and ^{8}B) and was stated that the ^{8}B-decay spectrum could not be reproduced following the expression of Wheeler [Whe41], who theorised the shape of the continuous α spectrum. It was proposed for the first time an alternative description of the α spectrum, involving two 2^+ levels in ^{8}Be, the known one at 3 MeV and a new one at 16.7 MeV (which lately was modified to 16.6 MeV). This experiment was the first to introduce one level at higher excitation energy in the description of the β-decay of ^{8}B. However, the isospin assigned to this level was wrong, as it was demonstrated in 1964 by Matt et al. [MPRS64].

Matt et al. [MPRS64] demonstrated the existence of the 16.6 MeV state assigning spin and parity 2^+. Otherwise, it was not possible to describe this state within the Breit-Wigner formalism. In the experiment it was measured the single α spectrum emphasising the region above 7.5 MeV. The width of the 16.6 MeV state found in the experiment supported the assignment of T=1 but with a small T=0 admixture, being the first time where the isospin mixing in this state was proposed.

It was Browne and collaborators [BCE66] in 1966 who, via reactions mechanism, fitted the experimental data with Barker's interference formula [Bar66] to the 2^+ doublet, being a proof that the states that conform the 2^+ doublet are strongly intermixed by the Coulomb interaction.

1.2.2 Halo structure of ^{8}B

A halo nucleus is characterised by having an inert core where all the nucleons are tightly bound and one or two extra nucleons surrounding the core, as a halo [Tan90] [Jon95]. Halo nuclei can be proton-halo or a neutron-halo depending on the particle orbiting the core. This particular structure originates in the

low binding energy of the last nucleon(s) and it manifests by a large scattering cross section due to the large matter radius. It is studied through the nuclear radius. Fig. 1.3 shows the radius of different nuclei measured experimentally for some of the best known halo nuclei: ^{6}He, ^{11}Li and ^{11}Be. The radii of these nuclei were determined from the interaction cross section of these nuclei at high energies when traversing a light target.

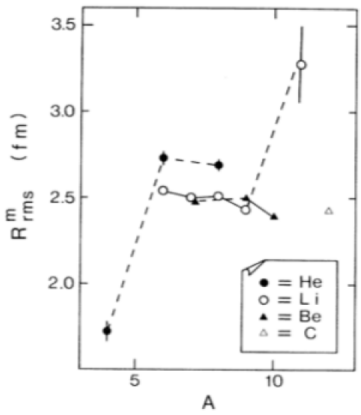

Figure 1.3: Nuclear matter radii of helium, lithium, beryllium and carbon isotopes. Picture from [THH^{+}85].

The nuclear structure of ^{8}B has been probed via elastic scattering [KaAIA^{+}18], inelastic scattering [CGMA^{+}02] and through the measurement of the reaction cross section of ^{8}B + ^{58}Ni [AMQL^{+}09].

The β^{+}/EC-decay of ^{8}B mainly populates the 2^{+} states due to the selection rules explained in the previous section (Sec. 1.1). Decays to the 0^{+} and 4^{+} states are second forbidden and hence strongly suppressed. The decay to the 1^{+} 17.6 MeV state is expected to be enhanced by the proton-halo structure of ^{8}B through EC.

The 1^{+} 17.6 MeV state is situated 385 keV above the p + ^{7}Li threshold (see Fig. 1.2 and is known from reaction studies [Wea95] that the only decay-channel is proton emission. Following the discussion in [BFF^{+}13], the EC decay rate can be estimated if one assumes the proton halo configuration of ^{8}B as a ^{7}Be core

plus a proton orbiting. The EC would occur in the ^{7}Be-core and the transition matrix element can be estimated to be the same as for the ground state of ^{7}Be decaying into the ground state of ^{7}Li. Scaling by the half-life, an upper limit of the branching ratio of the population of this state can be set to 2.3×10^{-8}.

1.2.3 Nuclear structure of ^{8}Be

α-cluster and shell model description

For many years, physicist have tried to describe the nuclear structure using different models. In particular, two different approaches have proven very useful: the independent particle and the collective models.

In the former, the most relevant is the well-known shell model, which consists in a quantum mechanical variant of the independent particle model. This model was described in analogy to the atomic shell model and could predict the magic numbers [GM48]. In this approach, the nuclear properties are determined by the least bound nucleons moving in a mean-field potential, independent of the close shell part of the nucleus.

In the latter, the nuclear motion and excitations are correlated (collective). For our purpose, the cluster model will be the example of collective models. It consists on describing the nucleus as one or more groups of nucleons that can be treated as individual particles. The α particle is the relevant cluster structure for many light nuclei [Fre07].

^{8}Be is one of the so-called α-conjugate nuclei which has the same number of neutrons and protons. Another nucleus with the same characteristics is the famous ^{12}C with its Hoyle state, which can be described as a stable nucleus while the three α are bound together but once one of the α is removed, the system is unstable and breaks into three α. Within the cluster models, the ground state of both ^{8}Be and ^{12}C are well described but not the excited states (except for the Hoyle state).

The ^{8}Be nucleus is unbound and its ground state is 91.8 keV above the 2α emission threshold. Myo et al. [MUH$^+$14] discussed in 2014 the α cluster structures in ^{8}Be dividing the nuclear structure of the nucleus in two groups: the ground-state band of 0^+ (g.s.), 2^+ (E=3 MeV) and 4^+ (E=11.4 MeV) as the

rotational band and the highly excited states above the 2^+ 16.6 MeV state.

These states decay into two α particles and are understood to be two α cluster states in their intrinsic structure. For the excited states, many spin states have been observed and their decay is not only via α emission but also via proton or γ emission [MUH+14].

The continuum of 2^+ states

From the β^+-decay of the ^{8}B a continuum of 2^+ states are populated. The most intense transition is the decay to the broad resonance at 3.03 MeV (see [RFHJ15]).

Since 1968, the continuous spectrum of ^{8}Be has been discussed many times. Barker proposed the existence of broad 0^+ and 2^+ states in ^{8}Be around 6 and 9 MeV respectively [Bar69] by performing simultaneous fits to inelastic scattering, reaction and decay data. The proposed states can be interpreted as intruder states in order to obtain a good parametrization within R-matrix analysis.

However, the main problem of this interpretation has been that the broad resonances are overlapping and still unresolved and none of the intruder states are seen in the spectrum as a peak. Moreover, these intruder states have not been predicted theoretically via shell-model or *ab initio* calculations.

The isospin mixing in the 2^+ doublet at 16 MeV

The two states at 16.6 and 16.9 MeV form a 2^+ doublet, being the only case in which one can expect more than a few percent of isospin mixing. In the work of [vB96] the doublet is described by two interacting isospin eigenstates.

Each of the states that form the 2^+ doublet have dominant configurations as ^{7}Li + p and ^{7}Be + n, respectively. The lower state, the 16.6 MeV, is 332 keV below the Q_{β^+} value and the 16.9 MeV state is 36 keV below, as can be seen in Fig. 1.4.

The ratio of the feeding via β^+ between the two states of the doublet results to be 1.5×10^{-5}. Experimentally it has been shown that this ratio is three orders

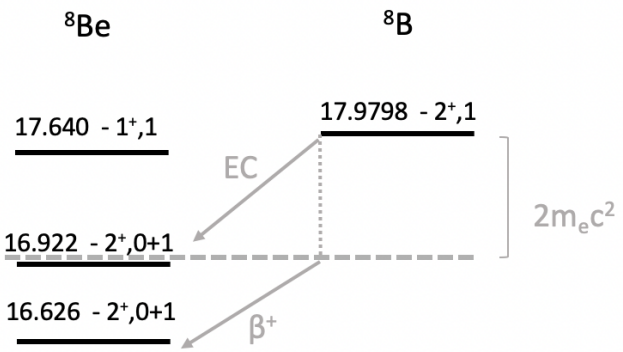

Figure 1.4: Zoom on the high energy region of the decay scheme of ^{8}B into ^{8}Be. Energies are given in MeV and referred to the ground state of ^{8}Be.

of magnitude higher [Kir10]. This discrepancy is explained as follows: the β-decay phase space grows with the fifth power of the E_β, being highly suppressed at high excitation energies close to the Q_{EC}. Therefore, it is mandatory to include the electron capture phase space to obtain the right feeding-ratio between the two levels.

In the work of von Brentano [vB96], it is assumed 100% isospin mixing between the doublet to be able to explain the population of these two states via reactions. The β-decay is a very selective tool and we should be able to determine the feeding to these two states and from there deduce the isospin mixing.

Facility and detectors 2

2.1 ISOLDE - CERN

One of the main factors to perform an experiment in a certain facility is the capability it has to provide a pure and intense radioactive beam. This was one of the reasons why the ISOLDE facility, at CERN, was chosen for the experiment.

CERN is one of the most important basic research centers in the world. It sits astride the Franco-Swiss border near Geneva. Since 1954, CERN has been the cradle of great discoveries in physics, such as the W and Z bosons or in the last decade the Higgs. CERN is a collaboration of 23 member states that support financially the facility. At CERN, apart from the high-energy particle physics there are also other activities in nuclear, fixed target and anti-proton research. The main activity is of course the LHC (Large Hadron Collider) where in detectors like CMS and ATLAS the Higgs boson have e.g. discovered.

Here we are more concerned with the low-energy activity and especially the ISOLDE facility that takes its seed from the PS-Booster (see Fig. 2.1). Other facilities of this low-energy experiments connected to other rings of the accelerator complex are, for example, n_TOF, anti-protons and fixed target experiments. Fig. 2.1 shows a detailed scheme of the accelerators and facilities at CERN.

The β-decay study of ^{8}B, the topic of this thesis work, was performed at

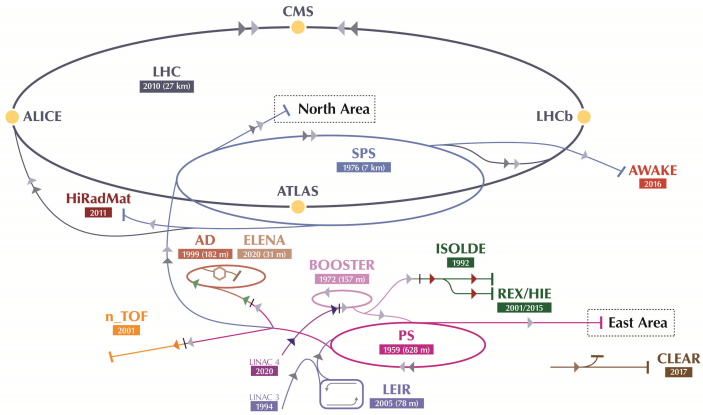

Figure 2.1: Diagram of the accelerators and facilities of the CERN complex. Picture taken from CERN webpage.

ISOLDE. This is the acronym of **I**sotope **S**eparator **O**n-**L**ine **De**vice and, as its name indicates, is based on the ISOL technique. The technique consists in producing the radioactive beam of interest by colliding a high energetic light-particle beam, usually protons (although heavier ions can be used), with a thick target kept at high temperature. The reaction products are produced in the thick target. Due to the high temperature they diffuse out via a transfer line into the ion-source. They are ionised to 1^+ charge state, extracted using a high voltage electrode and separated in mass with a magnetic dipole. Depending on the beam desired, different combinations of targets and ion-sources are being used.

ISOLDE was inaugurated in 1967 and has the power to produce more than 1100 isotopes and 300 isomers of more than 70 elements from Z=2 to Z=88. It is connected to the PS-Booster accelerator (**P**roton-**S**ynchroton **Booster**) and the proton beam that impinges on the target is presently of 1.4 GeV with an intensity of $\sim 3 \times 10^{13}$ p^+/pulse.

The ISOLDE target area has two different target stations coupled to one of the two separators available at ISOLDE, the **G**eneral **P**urpose **S**eparator (GPS) and the **H**igh **R**esolution **S**epator (HRS). Both are magnetic spectrometers and as their names indicate they have different mass resolution capabilities. The

GPS has one bending magnet and an electrostatic switch-yard that can extract simultaneously three mass separated beams within ±5.15% of central mass setting. The HRS consists of two bending magnets one after the other that together with an ion-optical system for higher order corrections can offer the selection of a single mass with a resolution of up to $M/\Delta M = 5000$ while the GPS is about 1000.

The production of the nucleus of interest takes place by spallation, fission or fragmentation reactions induced by the collision of the protons in the target. Some of the targets used at ISOLDE consist of molten metals kept at high temperature (from 700°C up to 1400°C) which are characterized by a relatively long release time. For faster release times of the produced isotopes, the target material can be in the form of metal powder, metals or carbides at temperatures above 2000°. The details of the target used and the beam production of our experiment (IS633 [BCF+16]) are explained later in Sec. 3.1.

The ISOLDE target unit (see Fig. 2.2) includes the target material encapsulated in a cylinder of Ta of 2 cm diameter 20 cm long, coupled at 90° with a transfer line followed by the ion-source. The ionization can be done in different ways; surface ionizer, electron-plasma ion-source or via an external laser-system that via mirrors shines 3 high intense lasers into the transfer line to take the atom from the ground state to the ionisation. The surface ion source is the simplest setup that can be heated up to 2400° to ionize the atoms produced in the target. The plasma ion source is used to ionize the elements that cannot be surface-ionized producing the plasma by a gas mixture that is ionized by accelerated electrons. The laser ion source creates ions inside a hot cavity surface via the three step aforementioned resonance lasers.

The ISOLDE facility itself can be divided in two sections: the low energy part and the post acceleration part (HIE-ISOLDE). In the former, mainly decay processes and fundamental properties of the nuclei in their ground or isomeric states are studied; as the mass, the radius, the spin or the electromagnetic properties using lasers. In the latter, the beam is post accelerated to a few MeV per nucleon opening the door to nuclear reactions studies. The layout of the ISOLDE experimental hall is shown in Fig. 2.2.

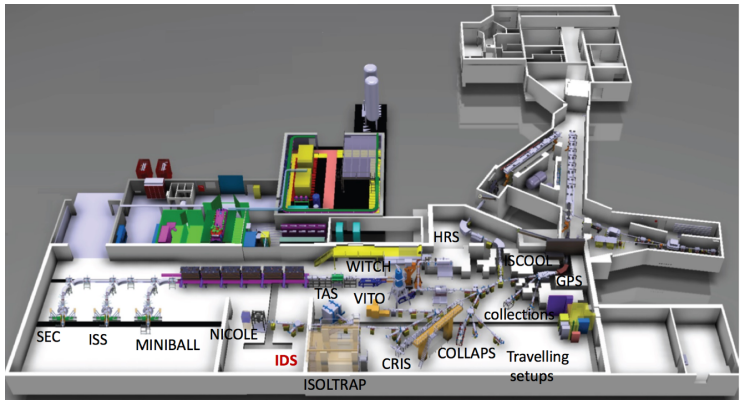

Figure 2.2: ISOLDE's hall layout, including the HIE-ISOLDE stations. The ISOLDE Decay Station is labelled in red. Picture taken from ISOLDE webpage.

2.1.1 ISOLDE Decay Station for IS633

The experiment core of this thesis work was performed at the **I**SOLDE **D**ecay **S**tation (IDS) which is a permanent setup for β-decay studies. IDS is a modular station that has allowed the users the realization of β-decay experiments using different setups for gamma and conversion electron spectroscopy studies, fast timing measurements, neutron time-of-flight studies or particle detection as in our case.

Although it is a modular station, it has permanently an array of four **h**igh **p**urity **Ge**rmanium detectors (HPGe). This array is composed by four clovers each containing four HPGe crystals of 50 mm diameter and 70 mm length encapsulated in the same cryostat. The detection system offers a very good efficiency and energy resolution for γ detection, with a relative efficiency of each crystal of a clover of 20% [Lic17]. The energy resolution of the summed 4 HPGe clovers using the Nutaq DAQ (default acquisition system of the station) is 2.40(5) keV for the ^{152}Eu peak at 1407 keV (see [Lic17] for more details) which is a better value than for non-segmented HPGe arrays of the same volume. The four HPGe Clovers are placed in a polyhedron frame at 75 mm to the implantation point.

The position of the four clovers with respect to the beam, allows to couple different implantation chambers. For the IS633 experiment, a cylinder extension

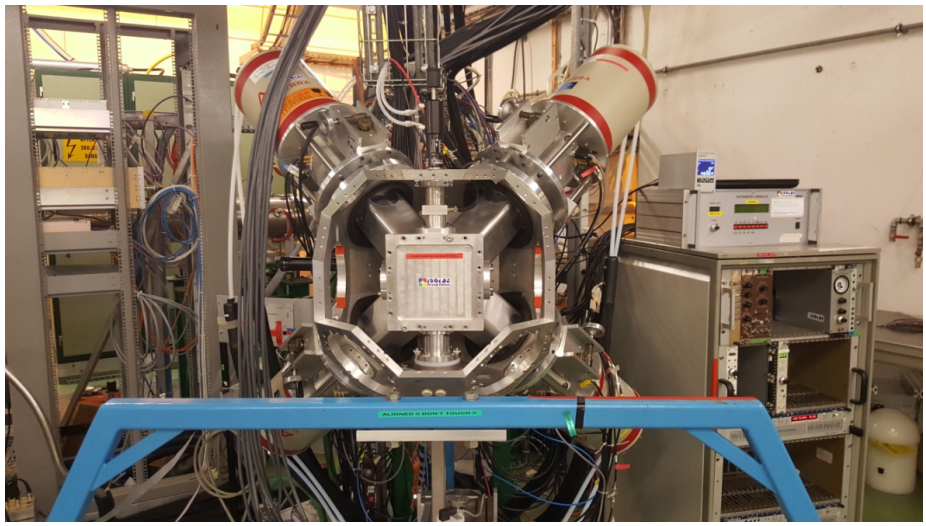

Figure 2.3: IDS line with the permanent HPGe clovers in their position.

was fixed at the end of the line, removing the metallic lid that can be seen in Fig. 2.3. The cylinder extension was used to have the particle-detection setup just after the line connected to an electronic board to reduce cables and have the full setup in vacuum. Fig. 2.4 shows two pictures of the experiment: the first one shows the end of the line opened without the cylinder extensions that hosts the Si-detector setup and the electronic board used in the experiment without the detectors. The second picture shows the cylindrical extension fixed at the end of the line and the electronic board. There, some detectors were placed for calibration measurement.

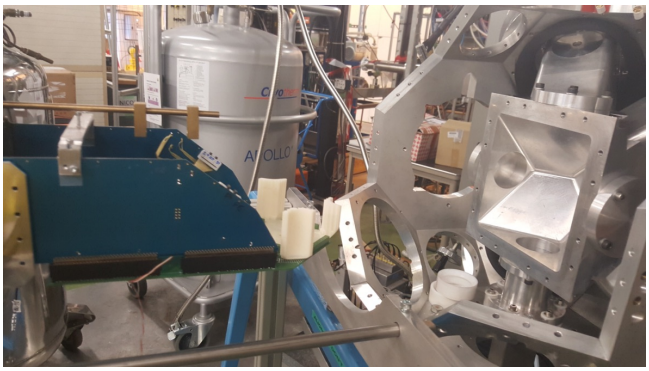

(a) End on the IDS line opened without the cylinder extension.

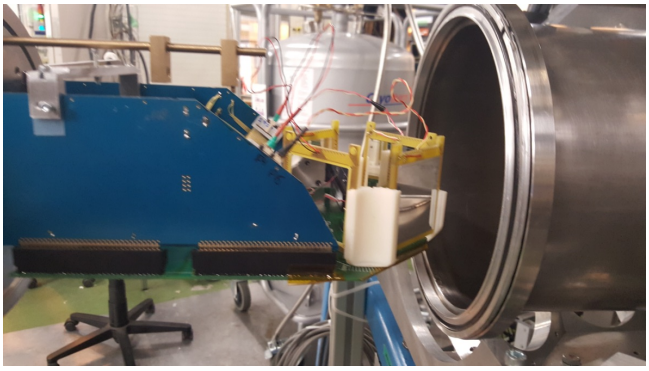

(b) The cylindrical extension fixed at the end of the line. There, some detectors were placed for a calibration measurement.

Figure 2.4: Two pictures of the IS633 experiment.

2.2 DETECTORS AND TECHNIQUE

2.2.1 Silicon Detectors

Silicon detectors are a type of semiconductor detectors. This type of detectors are based on a p-n junction in whose depletion region the particles loose their energy creating electron-hole pairs that are collected via metallic ohmic contacts. Silicon detectors are mainly used for charged particles due to its low Z number [Kno79]. They show a great linearity between the energy of the particle and the signal produced.

In the following, a general description of the detectors used in the experiment will be presented: the DSSD and the PADs.

DSSD

DSSD is the acronym of **D**ouble sided **S**ilicon **S**trip **D**etector.

The main characteristic of these detectors is the segmentation created with the spatial configuration of the doping implanted as strips: on the front, verticals bands, and on the back, horizontal ones. These contacts are of silicon material and are doped to make the p-n junction, being so-called strips type p or type n if are doped with p^+ or with n^+. Between the two sets of contacts it is found the active volume where the particles loose their energy. These contacts can be considered as a dead layer, which is a region where the particle looses energy but the charge generated is not collected. In the case of the IS633 experiment, the segmentation is of 256 pixels obtained with 16 strips type p^+ (horizontals) and 16 strips type n^+ (verticals). Fig. 2.5 shows a general view of a DSSD with the two sides, where the strips can be seen with the orthogonal distribution mentioned.

Between each strip, an insulator of SiO_2 is used to avoid the charge sharing between contiguous strips. To transport the charge collected and process it by the electronics, a metallic ohmic contact of aluminium is used. This contact is also considered a dead layer and, depending on the type of DSSD, its shape can be a grid or a layer covering the doping.

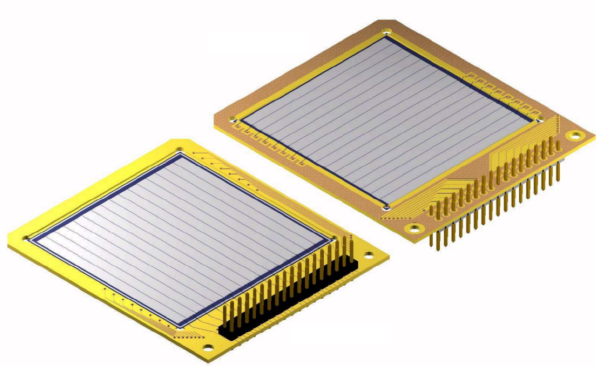

Figure 2.5: General view of a DSSD W1 (Double sided Silicon Strip Detector). Picture provide by Micron Semiconductor Ltd.

The characteristics mentioned are for the DSSD type W1 from Micron Semiconductor Ltd. The active area of this detector is 49.5×49.5 mm^2. In Tab. 2.1 there is a summary of the different front window configurations and doping thickness that Micron offers for this type of detectors. Another important parameter that can be chosen is the type of metallisation for the front window. The possible metallisation of the detectors used in the experiment are:

- M: A continuous metal coverage of standard thickness (0.5 μm) over the whole active area.

- G: Grid coverage, typically of 3% over the whole active area and contact pads for wire bonding, of standard thickness metallisation of 0.5 μm.

The combinations are between the window type and the metallisation, as for example, W1 2M or W1 9G. The back window is usually the same: 2M, which consists on an aluminium layer of 0.5 μm that covers all the doping. Combining the previous list and the Tab. 2.1 we can obtain the general characteristics of the detectors but in Sec. 4.3.3 the specifications for the detectors used in IS633 experiment will be detailed, which where of type W1 9G.

Table 2.1: Configuration of front window for a DSSD W1 offered by Micron Semiconductor Ltd (2015).

Window type	Dead layer
2	0.5 μm
7	0.1 μm
9	0.05 μm

PAD

PAD detectors are silicon detectors with no segmentation. The size of the PAD is 50×50 mm^2 in a frame of 55×55 mm^2. Fig. 2.6 shows a top view of one of the PADs (model MSX25) used in the experiment.

The front window of the PADs can be configured with the same types than for a DSSD (Tab. 2.1). The back window is usually 2M and the ones used in the experiment had the configuration of 2M for both windows.

For our experiment, the PADs were used as a VETO for the β-particles in a telescope configuration. The telescope configuration offers the possibility of complete the information of the particles detected merging the information of two (or more) detectors placing one of the detectors backing the other. This configuration is often used for particle identification by comparing the energy deposited in the front detector with the deposited in the second (or with the sum of the energy in the first and the second detector) in the so-called $\Delta E - E$ plot. In the IS633 experiment, the telescope configuration was used to have the DSSD as an α-detector and the PAD as a β-detector. The setup of the experiment will be explained in detail in Sec. 3.4.

2.2.2 Readout electronics

The chamber used in the IS633 experiment includes a PCB (**P**rinted **C**ircuit **B**oards) acting as feed-through between the vacuum inside the chamber and the atmosphere outside, and transmitting the electrical signals between the detectors inside and the pre-amplifiers connected outside the chamber. From the 5 DSSDs used in the experiment a total of 160 signals are collected in each read out (1 signal per strip, 32 strips per DSSD). Fig. 2.7 shows three pictures of

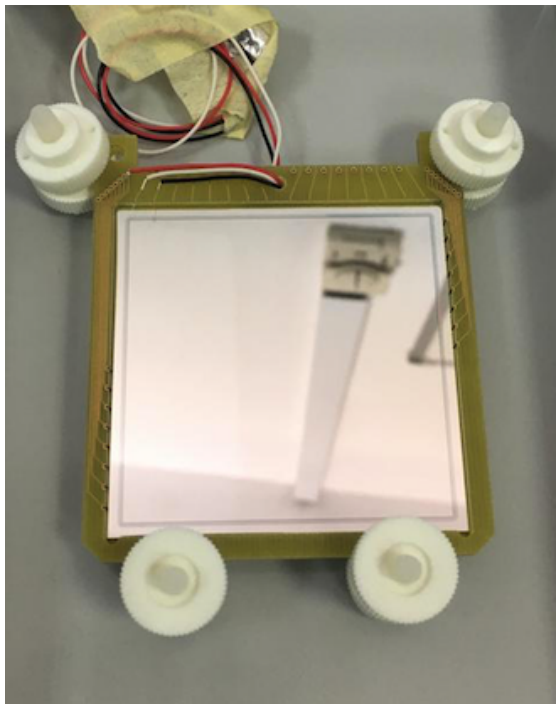

Figure 2.6: Picture of one of the PADs used in the experiment.

the experimental setup. The first, a top view of the PCB. The second, the pre-amplifiers connected. The third, the amplifiers labelled with the name of the detector connected. The PAD signals are collected directly also from the PCB.

Once the signal is processed by the pre-amplifiers, it is sent to the shaper via twisted pair cables. In the shaper, the signal splits into two chains: a logic and an energy chain.

The signal of the logic chain goes through the **T**iming **F**ilter **A**mplifier (TFA) that filters the signal to improve the definition of the time signal. After TFA, the signal is sent to a **L**eading **E**dge (LE) - detectors U2 and U5 - or to a **C**onstant **F**raction **D**iscriminator (CFD) - detectors U3, U4 and U6 - to select the signals of interest setting a threshold. From each detector, the logic signal is sent to a module called three-fold logic (CAEN module) where all the signals are ORed to obtain the experiment-TRIGGER. This TRIGGER is sent to the **G**ate and **D**elay module in order to produce a 4 μs gate for the ADC and the reference (START) of the **T**ime to **D**igital **C**onverter (TDC) that associates to each signal the time between the start and the stop signals.

In more detail, the logic between the detectors is as follows: from the TFA the signal is sent via a LE/CFD to the logic unit to build the trigger. In this module, two logic conditions are applied: the first one is that to accept an event, an AND condition is applied to the p- and n-signal of each DSSD, removing noise signals that are only produced on the electronic chain of one of the sides of the detector. The second condition is an OR between all the DSSDs, so if one DSSD triggers, the others are read. After the logic module the trigger signal goes to the digital chain to validate the event.

The signal of the energy chain, carrying the spectroscopic information (energy), is amplified in the shaper and from here goes directly to a 12-bits **A**nalog to **D**igital **C**onverter (ADC) that associates to each analogical signal a digital value. In the experiment, the integration window is of 4 μs. Once the signal is already digital, it is sent to the digital chain to store and process the information together with the time signal.

In the IS633 experiment, both the TFA and discriminators are included in the shapers used for the DSSDs and PADs (Mesytec STM16+ and MSCF-16).

In Fig. 2.8 one can see the scheme of the electronic chain used in the ex-

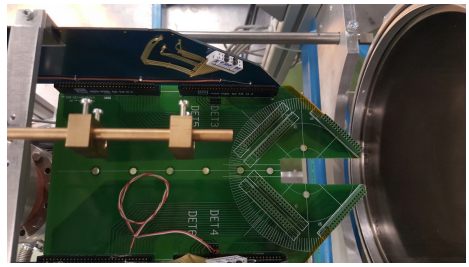

(a) Top view of the PCB used in the IS633 experiment. Each DSSD is connected directly on the connector of the bottom. The PADs are connected to the white pins on the lateral of the PCB. The detector are not seen in the picture.

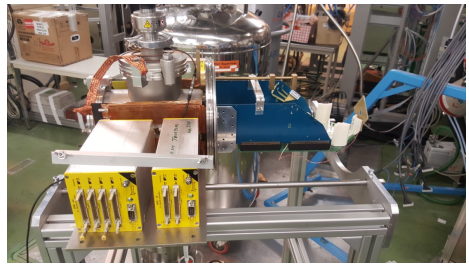

(b) Pre-amplifiers connected outside the chamber.

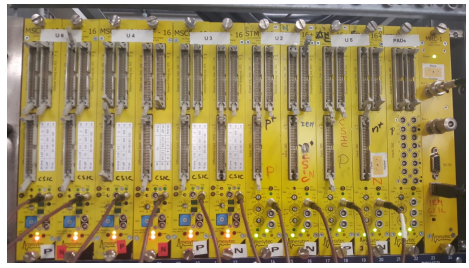

(c) Amplifiers used labelled with the detector name that is connected. For detectors U3, U4 and U6, the module is a MSCF-16. For detectors U2 and U5, STM16+.

Figure 2.7: Detailed pictures of the electronic (PCB, pre-amplifiers and amplifiers) used in the IS633 experiment

periment. All the time signals that came out from the amplifier have passed through a TFA and a CFD. Blue lines are the energy signal and the black lines the time signals.

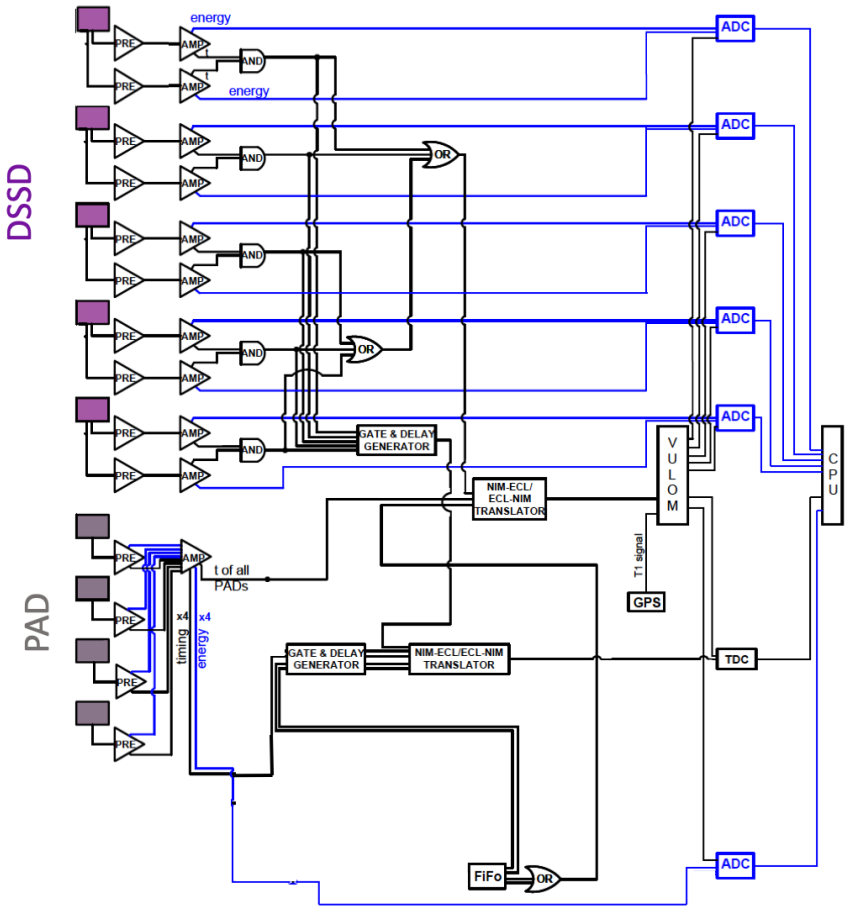

Figure 2.8: Electronic scheme of the IS633 experiment. All the time signals that came out from the amplifier have passed through a TFA. Blue lines are the energy signal and the black lines the time signals.

2.2.3 Data Structure

The data structure is defined and handled by the AUSAlib package [aus] developed by our collaborator fro University of Aarhus, the AUSAgroup, that performs, among other things, the unpacking of the data to make it treatable by an analysis program. This software package is based on ROOT [roo], a data analysis framework created and maintained by CERN which has the main advantage that provides a data structure, the TTree, that is extremely powerful for fast access of huge amounts of data much faster than accessing a normal file. Each TTree consists of a set of TBranches that contain the information of every parameter of each event (time, energy, channel,...). ROOT is developed in C++ and with the specific purpose of data processing and representation.

The data processing is done in two steps after the binary files are unpacked. The first data set consists in a non-calibrated information, where for each DSSD the signal processed by the p-side or the n-side is not matched. This first data set will be called *unpacked data* and has the following structure (where branches that are not useful for this experiment have been omitted):

- Energy branch for each DSSD: the energy is stored for each DSSD independently on ADC channels and the name of each branch has the structure of U*X*F_E or U*X*B_E depending on whether it is the p-side or the n-side signal, respectively. The X corresponds to the detector number: 2, 3, 4, 6 or 5.

- Time branch for each DSSD: similar than for the energy branches; U*X*F_T or U*X*B_T depending on whether it is the time signal of the p- or n-side of detector X. This is the TDC signal and is saved in units of 10 ns.

- Multiplicity of each DSSD: is a magnitude that indicates the number of hits in one detector per event. Also it is distinguished for the p-side (U*X*F) or for the n-side (U*X*B). There should not be difference in multiplicity between p and n sides, but it may happen due to electronic noise. These discrepancies will be solved in the next step of the data processing.

- Strip number branch that has collected the charge: U*X*FI or U*X*BI for the p- and n-side.

- Energy and time branches for the PADs: as only one signal is collected from the PADs, the information is saved in the branches PXE and PXT for the energy and time respectively. In this case, the number of the PAD can be 2, 3, 4 or 6.

- TPROTONS signal branch: this is a relevant global branch that stores information, in units of 10 ns, of the number of triggers in the experiment since the last proton pulse has arrived at the primary target. This signal will be used for the half-life determination (Sec. 5.3).

As said before, with this format the data are not yet calibrated and many effects are not corrected such as the energy matching between the p- and n-side, the noise and overflows removal and the inter-strip effect. These corrections are explained in Sec. 4.1 and therefore in the following only the details of the structure of the data after the so-called *Sorter* program will be explained.

The Sorter is a program of the AUSAlib package that performs the energy calibration per strip, does the p-n energy matching of the DSSD signals (removing the previous mentioned effects) and creates a new branch called *"mul"* which contains the general multiplicity of an event, which is a useful parameter during the analysis. In the sorted file, the data structure changes to have the energy branches *FE* and *BE* (p- and n-side respectively) and then the detector name as a condition: U2, U3, U4, U5 or U6. For the PADs, the energy is saved only in the *FE* branch. The strip information is in the branches *FI* and *BI* and the time signal in the *FT* and *BT*. With this structure, the data are more organized than in the unpacked stage. For the sorter process, information of the geometry of the setup and the calibration files are needed.

Experimental Measurement

3

3.1 ^{8}B BEAM PRODUCTION

As explained in the previous section (Sec. 2.1), the ISOL technique uses thick targets to maximise the production of the isotopes of interest. The three main reaction processes in the target for the production of the beams are spallation, fragmentation and fission. The isotopes move by effusion and diffusion from the very hot target material to the ion-source cavity, where they are ionized. Once the nuclei are extracted from the ion source using a HV potential up to 60 kV, the species are mass analyzed with a dipole magnet.

The extraction efficiencies from ISOL techniques can be up to 90% but for some elements this extraction is barely possible if they are refractory or chemically very reactive. The latter is the main problem for the production of boron. To extract one of its isotopes, the first step is the choice of the material of the target based on the boron production cross section and the experimental determination of its mobility, taking account both effusion and diffusion into processes. The relevant factors for a high-production rate are the production cross section σ for each isotope, the number of target nuclei and the number of proton impinging on it. The yield produced is calculated as

$$I_{secondary}(pps) = \sigma_{prod} \times N_{target} \times I_{protonbeam} \times \epsilon \tag{3.1}$$

where ϵ takes into account the different efficiencies involved in the production. At ISOLDE, the energy of these protons is 1.4 GeV. On the other hand, as

diffusion is a slow process compared with migration through open space, is mandatory a target characterized by a high open porosity and a small grain size. After the production, the isotopes diffuse out of the target and it is during this migration where the nuclei interact with the surrounding target and structural material. For the boron, the losses are so large that no radioactive beam is produced. The best material to produce a radioactive boron beam was found to be multi-walled carbon nanotubes [BSD+18].

Since boron has a high chemical reactivity and high boiling point, it is found possible to extract it as a molecule with a fluorination agent as boron and fluorine form relatively inert fluorides. The formation of the molecules must be fast, stable at operation temperature, inert towards reaction with the materials surrounding it and with sufficiently large cross sections. In [BSD+18] it is shown that the best compound is a boron trifluoride (BF_3) with the flourination made via sulfur hexafluoride (SF_6). Once the ionization is done, the most abundant species is BF_2^+, which arise from dissociative ionization of BF_3.

For practical purposes, ISOLDE release curves, $p(t)$, are typically fitted with three exponential functions given in Eq. 3.2 which is discussed in [LCD+97] and with the parameters defined in Tab. 3.1. The release time is an important parameter when the half-life of the nucleus is measured (Sec. 5.3) as the release curve can be considered in a simplistic view as the time that takes a certain chemical element to get out from the target-ion-source cavity.

$$p(t) = \frac{1}{A_L}(1 - e^{(-t/t_{rise})})(\alpha e^{(-t/t_{fall1})} + (1-\alpha)e^{(-t/t_{fall2})}) \tag{3.2}$$

Table 3.1: Release properties obtained from the curve fit of the ^{8}B isotope [BSD+18].

Ion	$\mathbf{t}_{rise}$	α	$\mathbf{t}_{fall1}$	$\mathbf{t}_{fall2}$
$^8BF_2^+$	52 ms	0.20	253 ms	3015 ms

3.2 MAIN GOAL OF THE EXPERIMENT

The main goal of this experiment is to resolve the 2^+ doublet state at 16.6 and 16.9 MeV populated via β^+ and electron capture (EC) respectively from the ^{8}B nucleus decay. This doublet is interesting due to the isospin mixing between the two states that lead to dominant configurations as ^{7}Li+p and ^{7}Be+n [vB96].

As said in Sec. 1.2.3, the lower state is 332 keV below the endpoint of the β-decay phase space while the 16.922 MeV state is 36 keV above (see Fig. 3.1). This means that the higher 2^+ state of the isospin doublet at 16.9 MeV, as well as the 1^+ state at 17.6 MeV, can only be populated via electron capture, whereas the lower 2^+ state of the doublet at 16.6 MeV will be populated via electron capture as well as β^+ emission.

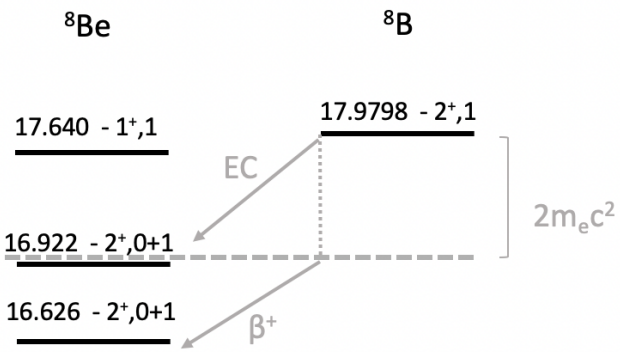

Figure 3.1: Zoom on the high energy region of the decay scheme of ^{8}B into ^{8}Be. Energies are given in MeV and referred to the ground state of ^{8}Be.

The feeding to the 16.922 MeV state was first seen, but with very low statistics, in a previous experiment performed at IGISOL by our collaboration, where 5 counts at the end of the excitation energy spectrum of ^{8}Be were assigned to the decay at 16.922(3) MeV to be compared with the 180 counts into the 16.626(3) MeV state [Kea11]. This experiment was performed to obtain higher statistics for the feeding of both states and learn more about the isospin mixing of the 2^+ doublet.

3.3 TIME-LINE OF THE EXPERIMENT

The experiment was carried out in May 2017 at the ISOLDE Decay Station (IDS). It started the night of the 23^{rd} with the beam tuning using ^{85}Rb with an extraction voltage of 60 kV. In order to have a stable running and a homogeneous implantation depth, the extraction voltage was decreased to 30 kV. The next day, the 24^{th}, the beam-line settings were readjusted using $^{32}S^{19}F$ and at 20:00h, the first ^{8}B ions reached the chamber with a counting rate of 25.000 counts/s and a dead time close to 40%.

The 26^{th}, the electronic thresholds were increased to reduce the dead time up to 2 MeV. After 4 hours, they were increased again up to 2.5 MeV, reducing the dead time below 10%. With these conditions, the run was smooth until the 28^{th} with the exception that a background measurement of one hour was done while the fluorination of the target was in progress. After the fluorination (explained in Sec. 3.1), a factor of two in the yield was lost for around 12 hours until the yield was recovered to 25.000 counts/s.

The 28^{th}, three hours were used to measure the half-life of ^{8}B and improve the uncertainty with respect to the last published measurement. After this period, the thresholds were decreased to the original values.

The 29^{th} at 8:45, the experiment finished and the calibration with α-sources started.

In total, 110 hours and 40 minutes of ^{8}B beam in the chamber, 32 hours and 40 minutes of α-calibrations and 4 hours and 10 minutes of background were recorded.

3.4 EXPERIMENTAL SETUP

The setup used was a "diamond" configuration of four Si-telescopes. The telescopes were composed by a thin ΔE-Double-sided Silicon Strip Detector (DSSD) with 16 strips at each side, backed by a thicker Si-detector. The detectors were fixed into a 3D-printed plastic structure to avoid any movement during the experiment and to facilitate the reproducibility of the geometrical conditions of the experiment during the use of external alpha sources for calibration. The 3D-plastic support was fixed onto a printed circuit board where the detectors were directly connected. An additional DSSD was placed at the bottom. Its thickness was 1000 μm and was used mainly as a β detector. Fig. 3.2 shows a picture of the setup with the detectors surrounding the carbon-catcher foil (C-foil of 31 μg/cm^2) where the ^{8}B beam was implanted perpendicular to the foil.

Two different front detector thicknesses were used in the telescopes; the thicker ΔE-DSSD of 60 μm assured the full detection of the highest energy α emitted in the breakup of the ^{8}Be. The thinner ΔE-DSSD of 40 μm were optimized for the second goal of the experiment: the detection of the delayed proton emission from the 17.6 MeV populated via EC and evidence of the p-halo structure of the ^{8}B nucleus, where better β-response and low background is mandatory. For the E-detectors of the telescope, the thicknesses were 1000 μm and 1500 μm, respectively.

In Fig. 3.3 one can see a sketch of the detectors (top view) with the distances and labels as in the experiment. The distances are in cm and the red arrow represents the incoming beam.

The characteristics of the detectors used are detailed on Tab. 3.2.

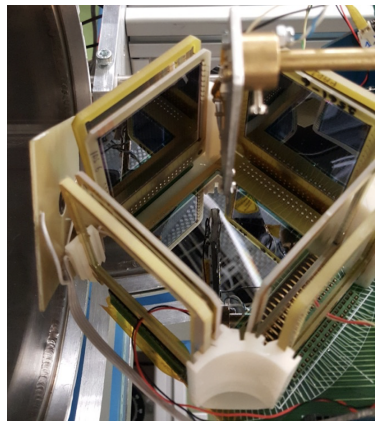

Figure 3.2: Picture of the setup placed inside the chamber used.

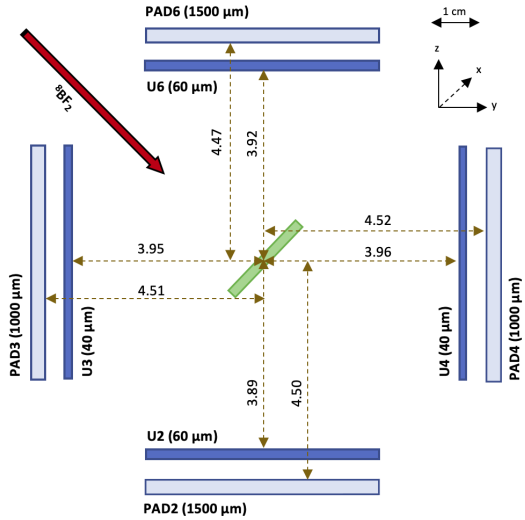

Figure 3.3: Distances defined on the 3D-plastic support designed for the IS633 experiment. The red arrow represents the incoming beam. All the measures are in cm.

Table 3.2: Characteristics of the detectors used in the experiment IS633A.

Detector	Thickness (μm)	Serial Number	Voltage applied(V)	Leackage Current (μA)
U2	60	DSSD 9G WI-60, 3187-5	-30	0.034
U3	40	DSSD 9G WI-40, 3203-12	-10	0.043
U4	42	DSSD 9G WI-40, 2561-6	-10	0.54
U6	60	DSSD 9G WI-60, 3187-4	-30	0.089
U5	1031	DSSD 9G WI-1000, 2635-21	-140	0.180
P2	1500	MSX25-1500 (MD006), 2280-27	-350	5.10
P3	1036	MSX25-1000, 3112-16	-160	0.143
P4	1038	MSX25-1000, 3112-14	-160	0.155
P6	1483	MSX25-1500 (MD005), 2280-15	-350	4

The dynamic range was set as follows:

- The amplification gain was adjusted to match the maximum energy deposited by the α particles in the detector (calculated using SRIM [ZZB10]) to the range of the 12 bit 8V-ADC used (CAEN V785G peak sensing ADC).
- The electronic thresholds were adjusted to cut the main contribution of the noise present on each strip.

Considering the noise observed in the different detectors, we choose a conservative threshold above the noise at 250 keV for ΔE detectors and 300 keV for E detectors as shown in Table 3.3 where it is also presented the dynamic range of each detector.

Table 3.3: Conservative low energy threshold above the noise and maximum α energy deposited in each detector.

Detector	**Threshold (keV)**	**E_{max} (MeV)**
U2 (60 μm)	250	9
U3 (40 μm)	250	7
U4 (40 μm)	250	7
U6 (60 μm)	250	9
U5 (1000 μm)	250	10
P2 (1500 μm)	300	7.5
P3 (1000 μm)	300	6.5
P4 (1000 μm)	300	7
P6 (1500 μm)	300	7

Data processing and Simulations

4

4.1 PRE-SORTING OF THE DATA

In an experiment, not all the events are relevant or have a physical meaning. To remove those unwanted events, some assumptions should be taken in order to differentiate what will be considered as good events and, in consequence, will be analysed and what will be rejected.

This section will explain the three main undesired effects that are direct consequence of the detectors used and the experimental issues associated to them.

4.1.1 Inter-strip and charge sharing events

The first effect that has to be checked is the inter-strip effect that the DSSDs present due to the charge collection via strips. Some α particles hit the region between two contiguous strips and, therefore, the energy of the α is shared between both contacts.

This effect produces an energy loss due to the charge sharing between the strips so the energy cannot be recovered 100%. As it is detailed in [GFT+14], the energy loss due to the inter-strip gap can be much larger than the nominal thickness of the inter-strip gap and depends on the energy of the detected particles and on the bias voltage applied.

Considering the amount of statistics collected during the experiment and that the ionisation of the particle cannot be fully recovered, the events with two hits in adjacent strips were removed from the data-set.

4.1.2 Energy-Matching

For some events it happens that the charge produced in the Silicon bulk is not fully collected by the p- or n-contact. To avoid this effect we must perform an energy matching between the p-side and the n-side of the detectors. This also removes random electronic noise from the channel.

The difference between the energy deposited on the p-strip and on the n-strip for each DSSD used in the experiment is shown in Fig. 4.1. In order to remove these undesired events, an energy condition is applied once the detector is energy calibrated: the maximum energy-difference between the p-strip and the n-strip allowed was set to ΔE=200 keV.

Applying this condition, the reduction in statistics for each detector is relatively low and amounts to 2.87(7)% and 4.90(7)% of the events for the 60 μm DSSDs (U2 and U6 respectively) and 2.66(8)% and 6.84(8)% for the 40 μm detectors (U3 and U4 respectively). The excess found in U6 detector (almost 5% of the reduction) is due to one n-strip not functioning correctly, increasing the amount of events where there is only signal on the p-strip. For the U4, there is an asymmetry in the noise contribution from the p-strips shown in the green curve presented in Fig. 4.1.

4.1.3 Overflows, pedestals and noise

The last condition is to remove the ADC overflows by using an artificial cut on the raw data (in channels) that correspond to energies above 11 MeV and 6.5 MeV for the DSSDs and the PADs respectively, which are far above the dynamic range of the detectors (see Tab. 3.3).

The noise levels for each strip of each detector are shown in Fig. 4.2, where the Y-axis is the ADC channel where the noise ends versus the strip number on the X-axis. To obtain these curves, the calibration data without the matching

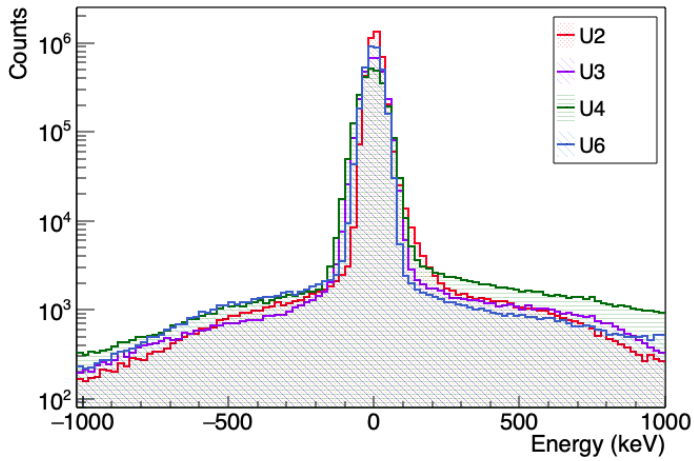

Figure 4.1: Difference between the energy deposited in the p-strip and in the n-strip for each DSSD used in the experiment IS633A. Note the asymmetry for the U4 detector (explained in text).

process was used. The noise levels are higher on the external strips (number 1 and/or 16) for all the detectors used except U2. Due to this effect, in many studies using DSSD, the external strips are removed. In this work, these strips are kept as with the matching process the amount of noise is practically removed and the coincidence conditions (see Sec. 5.1) applied to the data are restrictive enough to remove the noise-contribution of the external strips.

Once the p-n energy-matching process is applied (previous subsection), the noise contribution to each strip of each detector is practically removed. Fig. 4.3 shows the curves of the percentage of noise per strip for each detector after the energy-matching has been performed. As can be seen, the noise in the spectrum is practically removed from detector U2, U3 and U4. For U6, the amount of noise is higher but mainly on the external strips.

In Fig. 4.4 the percentage of statistics lost during the energy-matching process attributed to noise is shown. For detector U4 the loss has a maximum on the p-strips, confirming the asymmetry shown in Fig. 4.1. The 35% of noise in U4 is mainly on the external p-strips 1 and 16 but also the other strips are

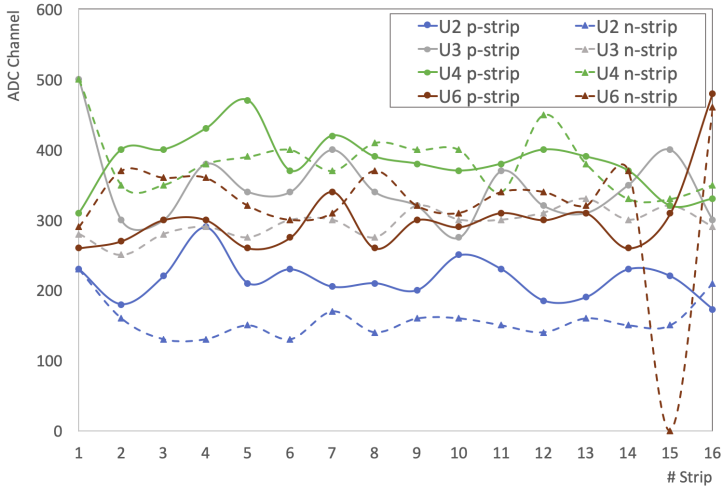

Figure 4.2: ADC channel noise threshold for each strip. The solid lines are for the p-strips and the dashed lines are for the n-strips. Only the detectors that conform the "diamond" are presented. N-Strip number 15 of detector U6 is not working correctly and no signal is recorded.

noisier than the n-strips. For the three other detectors, the amount of counts removed are below the 8% except for the p-strip number 16 of U3, where a 18% of counts are eliminated when the noise is removed. At the end, detector U4 is not used in the analysis except for obtaining one of the three non-correlated measurements of the half-life (Sec. 5.3).

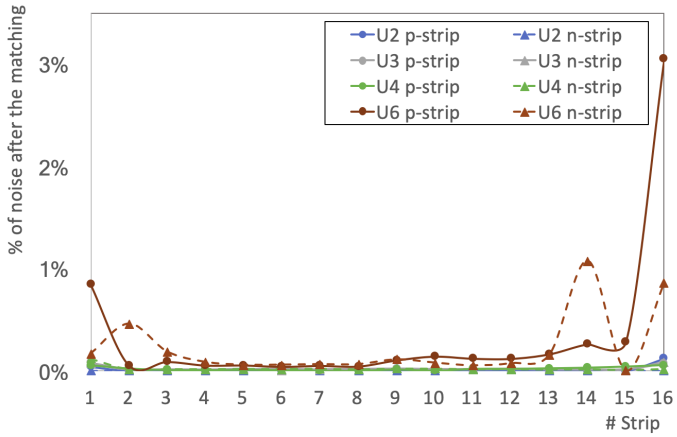

Figure 4.3: Remaining proportion of noise per strip for the different detectors once the energy-matching process is applied. The solid lines are for the p-strips and the dashed lines are for the n-strips. Notice that the U6 detector is more noisy.

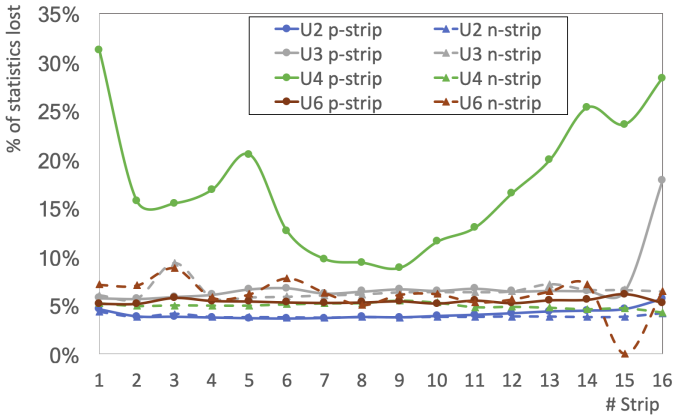

Figure 4.4: Percentage of counts removed per strip for the different detectors due to the noise removal. The solid lines are for the p-strips and the dashed lines are for the n-strips.

4.2 ENERGY CALIBRATION

4.2.1 Calibration sources

For the α calibration of the Si-detectors, the most common source used is the 4-α source, which is composed by four radio-isotopes that decay via α-emission with energies between 3 MeV and 6 MeV. The different isotopes included in the source as well as the different α intensities are listed in Table 4.1. The values are taken from Nuclear Data Services [nds].

Table 4.1: α energies and relative intensities of the four α-emitters in the source used for the calibration.

Isotope	Energy(keV)	Intensity (%)
^{148}Gd	3182.8	100
^{239}Pu	5156.59(14)	73.3(8)
	5144.3(8)	15.1(8)
	5105.5(8)	11.5(8)
^{241}Am	5485.6(12)	85.2(8)
	5442.90(13)	12.8(2)
	5388(1)	1.4(2)
^{244}Cm	5804.82(5)	76.4(2)
	5762.70(3)	23.6(2)
	5664(3)	0.022(1)

Fig. 4.5 shows the spectrum of the calibration source used (already calibrated). Due to the resolution of the detectors, only the most intense α is seen in the spectrum. The peaks at energies lower than the main emission are studied in detail in Sec. 4.3.4.

The source used was manufactured by *I.D.B. Holland B.V.* It is property of CERN and has the serial number 4235-36-37RP. The source is an open α-source on a stainless steel backing containing the four isotopes with the activity (measured the 1^{st} of November of 2007) detailed in Table 4.2, where the half life of each nucleus is specified. The total uncertainty listed is at the 99% confidence level. The disc where it is deposited has a thickness of 1 mm and an overall diameter of 24 mm with an active source of 19 mm (determined more precisely

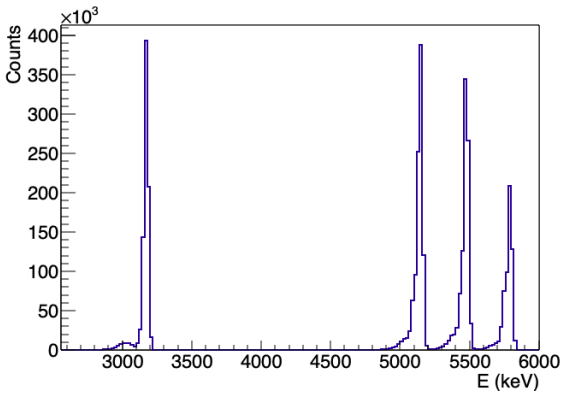

Figure 4.5: Spectrum of the 4-α source used to calibrate the experiment (U6 - 60μm).

Table 4.2: Data-sheet specification for the 4-α source used 4235-36-37RP certified the 1^{st} of November of 2007

Isotope	**Activity (1/11/07)**	**Half life (years)**	**Activity (23/4/17)**
^{148}Gd	1.197 kBq	75 ± 3	1.095 kBq
^{239}Pu	877.5 Bq	(2.411 ± 0.003)×10^4	877.3 Bq
^{241}Am	1.032 kBq	432.7 ± 0.5	1.016 kBq
^{244}Cm	1.158 kBq	18.11 ± 0.02	802 Bq

in Sec. 4.3.2).

4.2.2 Energy calibration per pixel

As explained in Sec. 2.2.1, the p- and n-strip perpendicular configuration allows to segment the detector into 16×16 = 256 pixels. This pixelization is used to take into account the impact angle of the particles detected and correct for the energy loss in each dead layer. As will be explained in the following, making a pixel calibration is more accurate than making it by strip.

To obtain the final energy calibration per pixel, a preliminary calibration

per strip has been done to convert the ADC (channels) into energy. It is done by fitting with a Gaussian function the spectrum obtained per strip of the 4-α source. This procedure is done using the calibrator tool from the Ausalib libraries [aus] developed by the AUSA group. With this first calibration the matching explained in Sec. 4.1.2 is applied, removing the undesired events i.e. noise, detection in the inter-strip region or incomplete charge collection.

The next step is a fine tuning to taylor the strip calibration to each pixel using the accurate simulation of the setup in GEANT4 defined in Sec. 4.3.3. A simulation with the 4-α source placed in the measurement position is done to obtain the energy deposited per pixel. In this step, high accuracy of the centroid determination is necessary. With this aim, two Gaussian functions folded together are used in order to take into account the tails of the peaks. The result of the fit with a double Gaussian for one pixel is shown in Fig. 4.6. Fitting the experimental calibration spectrum per pixel, the experimental energy detected is compared with the one obtained from the simulation for the same pixel. Then, a linear regression is applied to convert the spectrum from energy per strip to energy deposited per pixel. This process has been automatized for the 1280 pixels of the whole setup, and a visual check has been carried out to verify the quality of the fits like in Fig. 4.6. At this point, the detector is calibrated for the energy detected in each pixel and the pixels cannot be added as they are not yet corrected for the dead layer and, due to the emission angle, different pixels have different effective dead layers.

At this point, there are two independent ways to obtain a final spectrum. On one hand, the data can be unfolded for the response function to correct for the dead layers. On the other hand the data can be corrected for the energy loss in the dead layers by hand. The former approach requires to include all the effects in the response matrix defined in Sec. 4.3.4 and will not be discussed in this section. The latter approach consists in applying a linear regression to convert the energy deposited per pixel to the energy that would have been detected in absence of dead layers. To correct for the dead layers, the simulation must be done from the emission point.

With this last method, the calibration becomes more accurate than calibrating by strip. Fig 4.7 shows the comparison of the centroid of the ^{239}Pu peak (5.16 MeV) in 5 pixels distributed along the DSSD with a strip calibration (green) and with the pixel calibration (blue). The same trend is found for the other peaks and detectors. Clearly, if the data are analysed adding all the strips

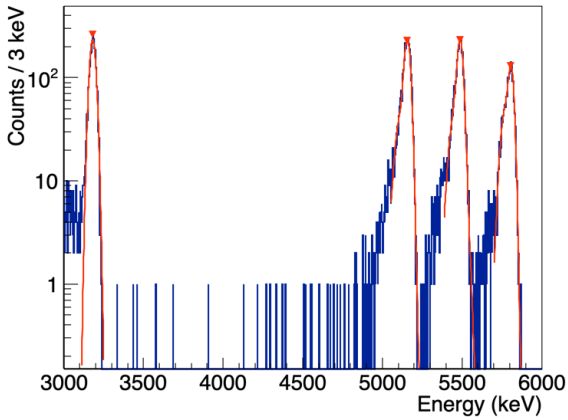

Figure 4.6: Fit of a pixel of detector U6 with two Gaussian functions folded to get high accuracy on the centroid determination as the tails of each peak are taken into account with the second gaussian.

together without correcting by the difference of solid angle covered along the strip and the emission angle, the peak to analyse will be broader, and therefore the resolution worse, than if the calibration is done per pixel and corrected by the energy loss in the dead layers. In other words, when using the strip calibration a systematic error is added as in the central pixels the effective dead layer is overestimated and therefore the energy of the peak is underestimated. The five pixels shown are from detector U6 and are identified in the inset of Fig. 4.7 corresponding to the next strip combinations:

- Pixel 1: P-strip = 1; N-strip = 1.
- Pixel 2: P-strip = 1; N-strip = 16.
- Pixel 3: P-strip = 8; N-strip = 8.
- Pixel 4: P-strip = 16; N-strip = 1.
- Pixel 5: P-strip = 16; N-strip = 16.

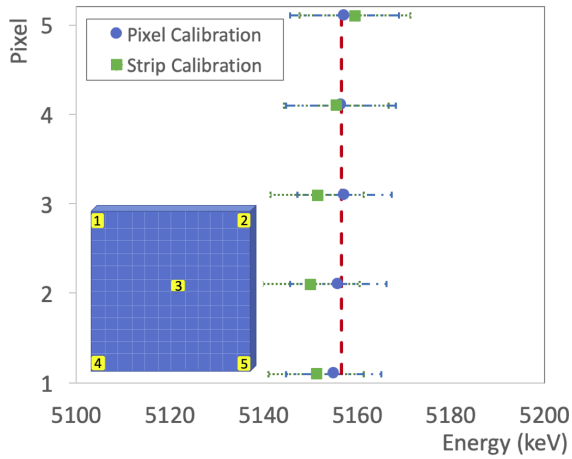

Figure 4.7: Comparison of the accuracy on the centroids of the ^{239}Pu peak between the strip calibration and the pixel calibration. The red line represents the exact emission energy. The inset shows a scheme of the distribution of the 5 pixels studied along a DSSD.

From Fig. 4.7 one concludes that the calibration per pixel is far more accurate than the one for strip. Moreover, the Calibrator tool overestimates the dead layer in the middle of the detector (Pixel 3, position (8,8)) worsening the calibration of the central pixels to obtain a better calibration on the external strips. With the pixel calibration this effect is removes. The PAD calibration is detailed in Table. 4.3. To obtain this calibration, the 4-α source has been used and fitted for each PAD. A simple Gaussian function has been used to fit the source.

Table 4.3: Calibration of the PAD-detectors.

PAD	**Slope (keV/ch)**	**Offset (keV)**
P2	1.8519	55.838
P3	1.6253	112.03
P4	1.7049	105.53
P6	1.7436	96.139

4.2.3 Resolution obtained by pixel calibration

The resolution of a DSSD is influenced by four aspects:

- The intrinsic resolution is due to the difference in the electron-hole recombination caused by defects in the Silicon wafer.
- The depletion voltage of the detector. If the voltage applied is not sufficient, part of the Si-active-volume of the DSSD becomes dead layer and increases the energy loss of the particles in the non-active areas. The addition of this non-active zone is not known. For this reason, in the experiment all the detectors were biased to double depletion to minimize the dead layer.
- The electronic noise present, which was minimized during the setup of the experiment.
- The dead layers that come from the doping depths, the aluminium contacts and the silicon oxide insulator between the strips. This effect is corrected with the pixel calibration explained in the previous section.

The main factor that affects the resolution of the detectors is the one that cannot be improved: the intrinsic resolution. The intrinsic resolution is not a global effect of the detector but of each strip. In order to obtain the best resolution, a comparison between the resolution of the p-strips and the n-strips is done once all the pixels are corrected by the dead layers and added. Table 4.4 shows the resolution of the ^{148}Gd peak of each detector for the p-strips and n-strips and also once the average of the energy collected in the p-strip and in the n-strip per event is done. Using this average energy ($\bar{E}$), an improvement on the energy resolution in the detectors where both strips (p and n) have a similar resolution is obtained, except for detector U4 where the resolution of the p-strips is almost a factor of two worse than the resolution of the n-strips. For this reason, in detector U4 only the energy deposited in the n-strips will be retained.

Table 4.4: Energy resolution of each detector for the ^{148}Gd peak. The first column is the resolution found when analysing only the p-strips, the second column when analysing the n-strips and the third column when adding both signals and doing the average.

Detector	**Resolution p-strips (keV)**	**Resolution n-strips (keV)**	**Resolution $\bar{E}$ (keV)**
U2	41.19(3)	41.36(4)	32.94(3)
U3	58.36(5)	59.56(6)	45.46(4)
U4	86.92(7)	45.14(4)	53.88(5)
U6	42.80(4)	48.51(4)	34.56(3)

4.3 MONTE CARLO SIMULATION OF THE SET-UP WITH GEANT4

An accurate Monte Carlo simulation of the geometrical and the physical processes that occur in the set-up is a powerful tool that allows to reproduce the observed data during the experiment and gives information about the detectors and their response to the passage of radiation, being a check of the goodness of the experimental set-up and the data obtained. In this work, the GEANT4 [AAA+03] package has been used to simulate the set-up. Moreover, as in GEANT4 the physical processes are already implemented with a great degree of detail, the information about the kinematics of the experiment can be reproduced.

In this section the procedure of simulating the geometry and why it is necessary to reproduce the response function of the detectors will be explained, but first, an introduction to the Monte Carlo calculations and the GEANT4 package is presented.

4.3.1 The GEANT4 package

Monte Carlo methods are a broad class of computational algorithms that rely on repeated random sampling to obtain numerical results. In physics, those algorithms are useful for simulating systems with many coupled degrees of freedom, such as fluids, disordered materials or, in the case that concerns us, generate plots from a probability distribution, as the decay scheme of nuclei.

GEANT4 is a toolkit for the simulation of the passage of radiation and particles through matter, with applications in high-energy, nuclear and accelerator physics [AAA+03]. It has been created exploiting software engineering and object-oriented technology, implemented in the C++ programming language. The toolkit provides a diverse, wide-ranging and yet cohesive set of software components. The set of components allows to divide the code in different parts: the generation of primary events, the physics to include in the simulation and the geometry of the setup among others.

For the interest of this work, the components of the code which we have been working with are detailed in the following.

First is, of course, the event generator that allows to define a physics event with the primary particle. The primary particle can be either an ion or a light particle as α or β. Also γ rays can be defined. The definition of the primary particle includes the energy of emittance, the position and the momentum direction. The decay scheme of each isotope is defined in the libraries of GEANT4, however, the decay of the ^{8}B nucleus is not defined as the emphGEANT4 radioactive files do not include broad resonances. This is why we have built specific radioactive decay files for this work.

Each event simulated is processed independently. To simplify the analysis and comparison of the simulations, the same data structure than for the experimental data (see Sec. 2.2.3) is defined for the output of the simulations thanks to that GEANT4 can be linked to the ROOT libraries. For general purposes, in each event, the data are chosen so that only energies produced in interaction with the detectors of the setup are stored. However, to define the kinematic conditions no setup was included in the simulations and therefore the storage of the data was defined differently.

The physics included in our simulations is the standard for nuclear physics: the electromagnetic interaction and the radioactive decay libraries.

Finally, the most modified module is the geometry one, which includes the description of the setup and conforms the main work of this section, with the definition of the fine structure of the DSSD. In this section it has been modified the step length as a function of the thickness of the layer which the particle interacts with. For example, the step of interaction for the p-doping has been fixed to 0.1 μm.

4.3.2 Positions of emission

In order to correctly define the geometry of the DSSD, it is essential to know the emission points of the α's detected. Depending on the emission point, the trajectories of the particles differ and so it does the effective thickness of dead layers.

The position of the calibration source is determined comparing the experimental hit patterns of the 4-α source with the simulated ones until the most

similar profiles are obtained.

The beam-spot of ^{8}B is determined reconstructing the kinematics of the decay and using the reconstruction of the coincidence.

α-source

The calibration of the detectors was done per pairs because the source only emits in 2π, therefore two different positions of the source have to be determined. Fig. 4.8 shows a picture of the experiment when detector U3 and U6 were calibrated, with the source facing not perpendicularly the detectors. The first position to determine is for detectors U3 and U6. The second, the position for the U2 and U4 calibration. Both positions are determined with the same method, that consists in discretizing the central region of the chamber in cubes of $2\times2\times2$ mm^3 in order to achieve a good balance between the spatial resolution and the computational time.

The main issue of this process is that the source's profile is not well described in the corresponding data sheet (see Sec. 4.2.1). The simulation has the source simplified to a circle to reduce the number of variables to optimize as the profile of the source is unknown. The radius of the simulated source has been fixed to 5.25 mm from the experimental hit patterns (left column of Fig. 4.9), calculating the FWHM. Another assumption is to consider that there is no tilt of the source, so the only possible movement is along the X-,Y- and Z-axis.

By looking at the pictures of the source position, it was well centered. In order to get the exact position, a discretitzation of the central region in a $24\times24\times24$ mm^3 cube has been scanned with a 2 mm pitch in each direction. In total, 2197 simulation have been done to determine the two positions of the source. The analysis has focused on the error calculation between the experimental and the simulated distribution of counts. For the first position (detectors U3 and U6), the position determined is (-6,0,6) mm and for the second position (detectors U2 and U4), (4,0,6) mm. The difference in the X-position between the two measurements is reasonable as one have the thickness of the α-source disk an a certain imprecision in the positioning. Fig 4.9 shows the experimental and the simulated hit patterns of each DSSD. On the left, the experimental patterns. On the right, the simulated ones.

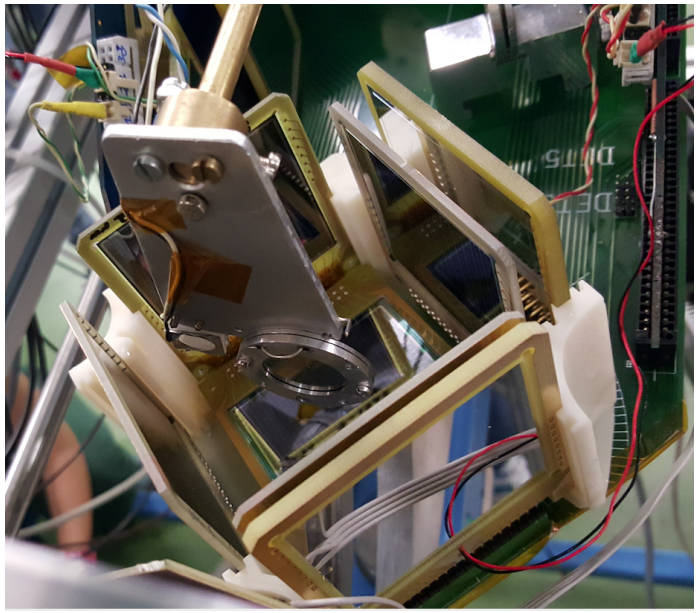

Figure 4.8: Picture of the calibration of detectors U3 and U6, with the α-source facing the two detectors.

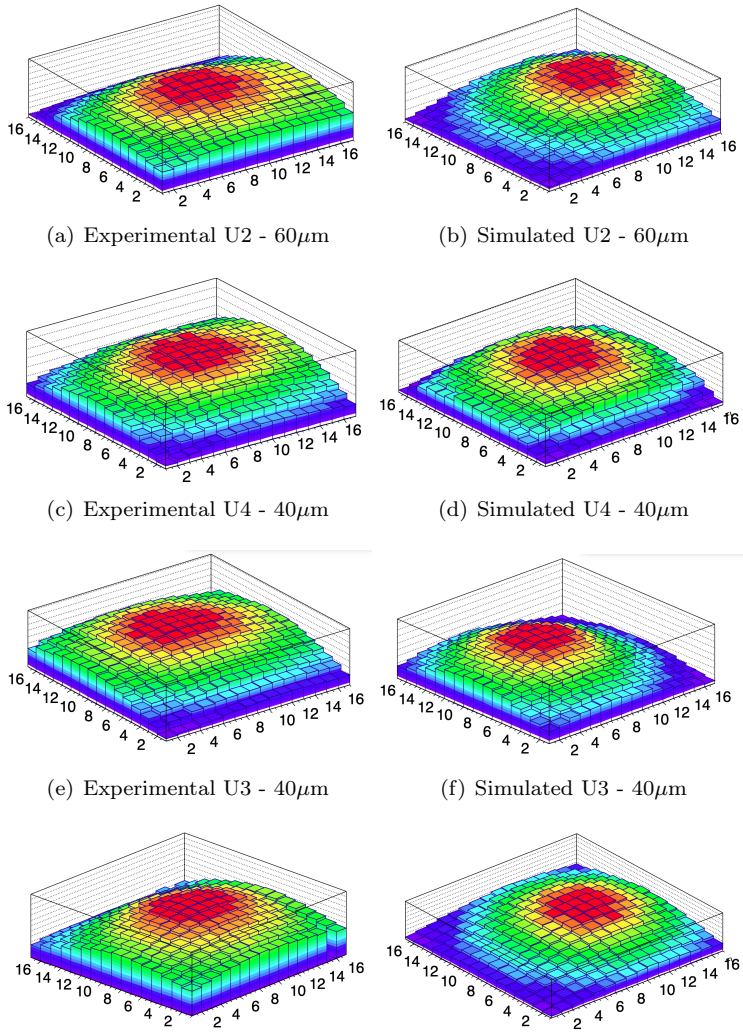

(a) Experimental U2 - 60μm (b) Simulated U2 - 60μm

(c) Experimental U4 - 40μm (d) Simulated U4 - 40μm

(e) Experimental U3 - 40μm (f) Simulated U3 - 40μm

(g) Experimental U6 - 60μm (h) Simulated U6 - 60μm

Figure 4.9: Comparison of the experimental (left) and simulated (right) hit maps for each DSSD using the α-source. The simulations show the source in the final positions: (4,0,6) mm for U2 and U4 and (-6,0,6) mm for U3 and U6. The small deviations between the experimental and the simulated hit maps are probably due to a tilt in the calibration source positioning (explained in the text). Vertical axis is the number of counts (arbitrary).

The comparison of both experimental and simulated patterns shows that the source had a tilt during the measurements as the elliptical form seen on the position of U2 and U4 is larger than for the U3 and U6 position. Neglecting this effect, the simulation places the source in the right position and with the right diameter, which is smaller than the one mentioned in the source certificate by a factor of 2.

^{8}B beam

The catcher used to stop the beam is placed in the center of the chamber (Sec. 3.4) and is a Carbon foil of thickness 31 μg/cm^2. The beam was a molecule of $^{8}BF_2$ extracted using a 30.0(1) kV pulsed high-voltage. With this voltage, the implantation depth is close to 26 nm in the 138 nm thick C-foil catcher.

By reconstructing the kinematics of the breakup of the ^{8}Be, the beam spot on the C-foil can be recovered. Fig. 4.10 shows the distribution of the implantation point of part of the data analysed. For this analysis, the catcher has been defined on the y=z plane and only has been considered the α-α coincidences detected in two opposite detectors with an energy difference ΔE $<$ 200 keV. The distribution is obtained without requiring any geometrical distribution along the pair of detectors. The detectors of 40 μm and 60 μm have been pairwise analysed.

The FWHM estimated from fitting the peak in Fig 4.10 is 4.934(19) mm on the x-axis and 4.746(22) mm on the y-axis. The position of the C-foil defined by this beamspot is (-1.602(11), -0.116(11), -0.116(11)) mm. This position can be checked by analyzing the detectors' hit pattern. The hit patterns of the DSSD are obtained by plotting the counts of the p-side versus the n-side and can be seen in Fig. 4.11 and it is clearly displaced as was calculated by fitting the beamspot. The n-strip number 14 of U6 presents more counts than expected as an effect of the contiguous dead strip. Fig 4.12 shows a 3D distribution of the hit maps with the C-foil centered.

4.3.3 GEANT4 simulation of a DSSD

To obtain an accurate characterization of each DSSD, the monochromatic α-source used in the calibration, ^{148}Gd, has been used. The experimental spec-

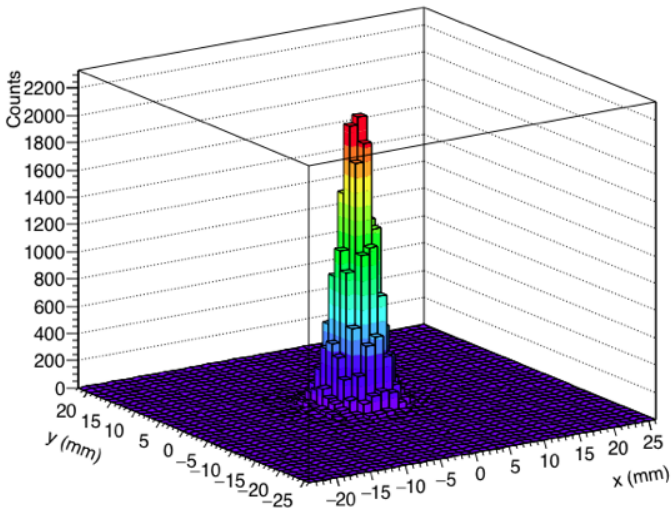

Figure 4.10: Beam-spot profile of ^{8}B in the C-foil positioned in the center of the detector setup, with a size of 4.9 mm and 4.7 mm in the x and y-directions respectively (dimensions given as FWHM). It has been calculated from the detection of two α in coincidence in energy and in opposite detectors. The C-foil is defined on the plane y=z.

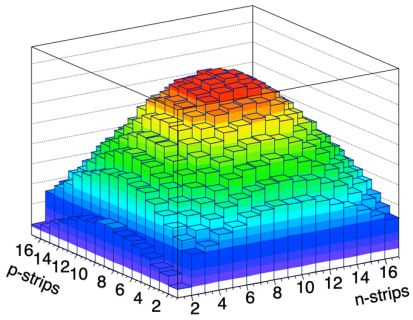

(a) Hit pattern of U2 - 60μm

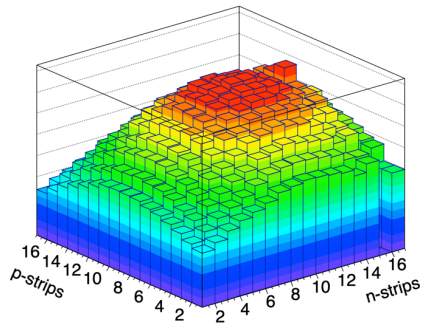

(b) Hit pattern of U6 - 60μm

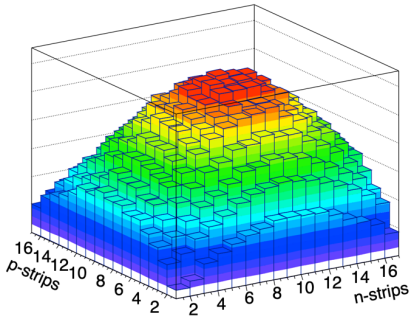

(c) Hit pattern of U3 - 40μm

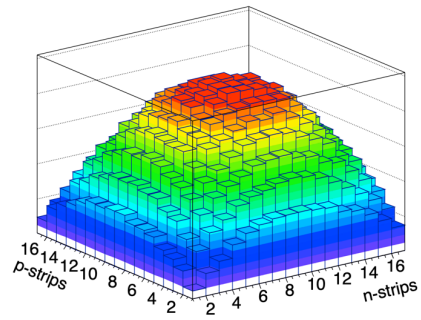

(d) Hit pattern of U4 - 40μm

Figure 4.11: Experimental hit patterns of the DSSD detectors for a ^{8}B-decay file.

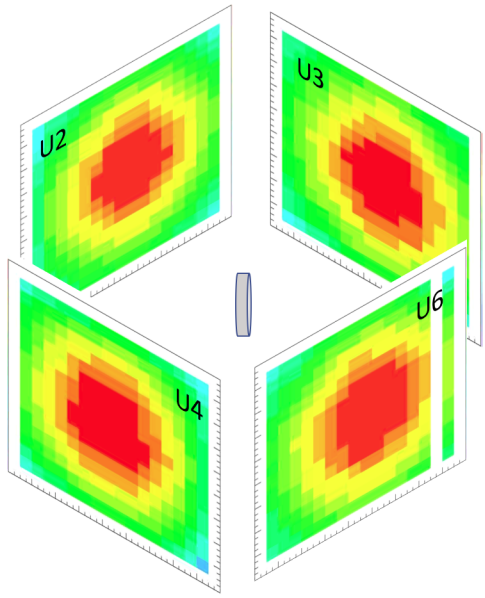

Figure 4.12: 3D representation of the hit maps of the detectors used in the IS633A experiment, with the C-foil at 90° to the incoming beam in the center of the setup. The horizontal axis of each hit map represents the n-strips and the vertical axis the p-strips. Detectors U4 and U6 are inverted as a mirror to show the distribution inside the chamber. The white area in U6 is the dead strip of the detector (n-strip number 15).

trum of this α has been compared in shape and in energy with the simulation of the ^{148}Gd α-emission in GEANT4. The different dead layers have been adjusted to reproduce the experimental peak.

The starting point of the simulated geometry is the one detailed in Fig. 4.13 that shows a sketch of the transversal section of a 60 μm DSSD with the different dead layers and specifications from the manufacturer (Micron Semiconductor Ltd). For the 40 μm DSSD it is the same configuration except for the active volume of Si where the ionisation is produced that is changed.

With this initial configuration, the intrinsic resolution of the simulated de-

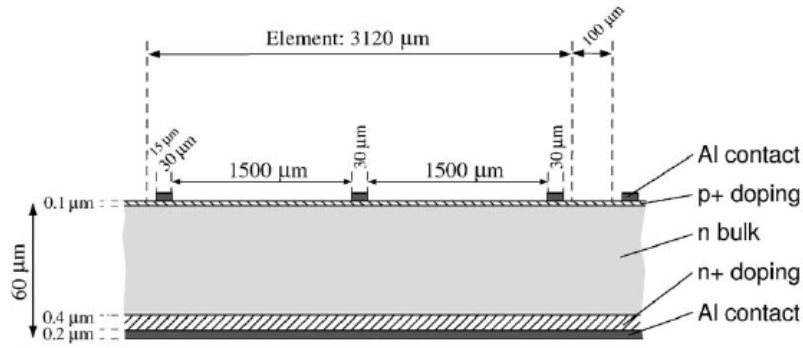

Figure 4.13: Sketch of the transversal section of a 60 μm DSSD with the specifications of the manufacturer for the first generation of this type of detectors where the thickness of the p^+-doping was larger than the ones used in this experiment. Picture taken from [TBF+04].

tector is adjusted by fitting the FWHM of both experimental and simulated peaks. The simulation includes the p^+-doping and the aluminium grid with the thickness, width and position as in the sketch. Fig. 4.14 shows the first comparison between the simulation of the detector U6 and the ^{148}Gd peak once the intrinsic resolution is applied to the simulation. Both spectra are normalized in the region shown and the source is simulated in the position defined in Sec. 4.3.2. Comparing both shapes it appears that an extra dead layer is needed to reproduce the experimental spectrum.

Adding an insulator of SiO_2, which is one of the most common insulators used in Si-detectors, between the p-strips and adjusting the width and the thickness, the shape of the monochromatic α-emission from ^{148}Gd is simulated and the result is in good agreement with the experimental peak (see Fig. 4.15). To include it, the p^+-doping between the p-strips has been replaced by the insulator. The differences on the tail of the peak is due to the contribution of the tails from the 3 other isotopes present in the source: ^{239}Pu, ^{241}Am and ^{244}Cm (see Sec. 4.2.1 for details of the source used to calibrate). Besides this contribution, the incomplete charge collection at the contacts will also produce a small difference between the simulated and measured tails as we will see later.

Once the shape is reproduced and without changes on the GEANT4 geome-

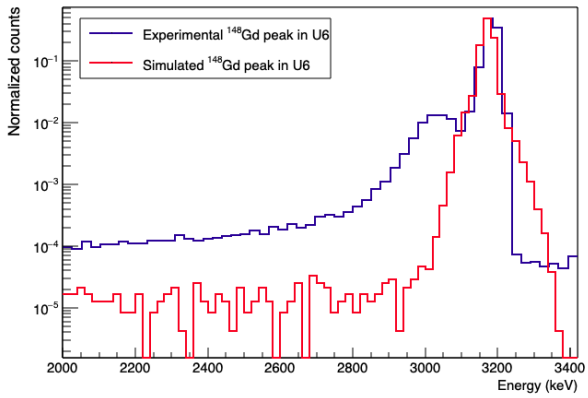

Figure 4.14: Comparison between the ^{148}Gd peak and the simulation of the nucleus with the initial parameters defined in [TBF+04] and the intrinsic resolution adjusted in the simulation. DSSD U6 (60 μm). Note the logarithmic scale.

try, the radiation from the three other α decaying nuclei present in the standard source are simulated to reproduce the experimental calibration spectrum. Also, by simulating the four nuclei, the tails at lower energies are enhanced due to the contribution from the higher energetic peaks. Fig. 4.16 shows in blue the experimental calibration spectrum for detector U6 and in red the simulated spectrum. The proportion of the nuclei in the simulation has been adjusted to coincide with the proportions on the source. Once the 4 isotopes are simulated, the main differences in the tails at lower energies are corrected. However, the simulation cannot reproduce a small fraction of the tail very close to each peak, which is the part related with the incomplete charge collection: some of the electron-hole pairs are recombined in the active volume or trapped, not reaching the electrodes. This effect has not been included in the simulation as this tails contributes only a 0.58(3)% to the ^{148}Gd peak and the tail with the contribution of the three other nuclei. Moreover, in Sec. 6.2 it will be shown that these discrepancies do not affect the deconvolution process.

The fine tuning of the simulated geometry has been done one by one for each DSSD used in the experiment. The manufacturer's values have been considered to have a 10% tolerance and the adjustment on the geometry has been always

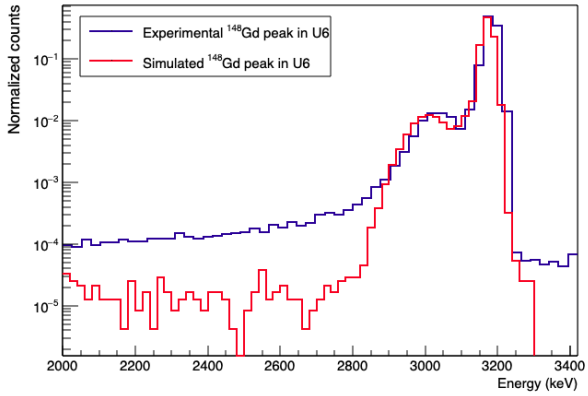

Figure 4.15: Comparison between the ^{148}Gd peak and the simulation of the nucleus once an insulator of SiO_2 is included between the p-strips. DSSD U6 (60 μm). Note the logarithmic intensity scale, being the long tails on both sides due to the contribution of the other isotopes present in the source.

within the limits determined by the manufacturer and the tolerance. The adjustment has been focused mainly on the thickness of the different layers that conform the DSSD. Table 4.5 has the final parameters of each dead layer for each DSSD. Fig. 4.17 shows the same transversal sketch as in [TBF$^+$04] including the SiO_2 insulator and without the dimensions as they depend on the detector.

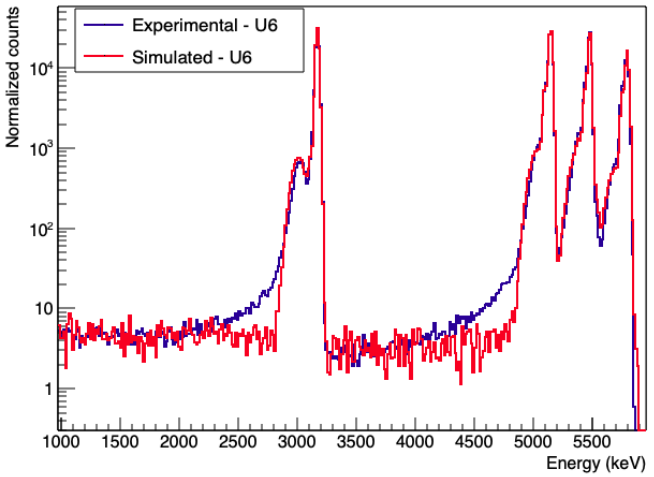

Figure 4.16: Comparison between the experimental calibration spectrum and the simulation of the four nuclei that contains the source with the geometry adjusted. DSSD U6 (60 μm). Note that the discrepancies in the tails of the peaks amount less than 1%.

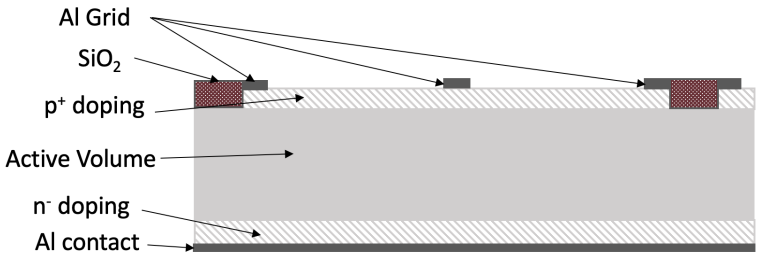

Figure 4.17: Sketch of the transversal section of a 60 μm DSSD including the insulator of SiO_2. Not to scale. See Table 4.5 for thickness and width values.

Table 4.5: Final geometry simulated of each DSSD used in the experiment.

DSSD Element		Reference value	U2	U6	U3	U4
N-bulk (μm)		60/40	59.3		39.3	
Al Grid	**Thickness (μm)**	–	0.2	0.2	0.2	0.3
	Width (μm)	30	30	30	30	33
p^+-doping	**Thickness (μm)**	0.05	0.05			
	Width (μm)	3120	3000	2950	2950	3100
SiO_2	**Thickness (μm)**	–	0.6			
	Width (μm)	100	207	254	254	113
n^--doping	**Thickness (μm)**	0.4	0.4			
	Width (μm)	3120	3120			
Al contact	**Thickness (μm)**	0.2	0.2			

4.3.4 Response function of a DSSD

The response function of a detector is defined as the pulse-height spectrum produced by a mono-energetic source. In this work, an accurate knowledge of the response function of the detectors is of paramount importance. The reason is that it will be included in the R-matrix analysis code (Sec. 5.5.1) where it is needed to fold the resulting excitation spectrum (β-feeding distribution) with a realistic detector response function.

In previous works [Kea11], the response function is obtained mathematically fitting a monochromatic source as suggested in [BAS06], where a Gaussian function is folded with two low-energy exponential tails to fit the α emitted by ^{148}Gd. The use of a mathematical expression to obtain the response function has the inconvenience that it has no physical meaning and can introduce systematic errors on the analysis. It can happen that it fits some experimental peaks in a certain energy region, but cannot be extrapolated to other energy values.

In this work, we have introduced the setup in a GEANT4 simulation and have adjusted the geometry until it reproduces the calibration source consisting of four α decaying nuclei in a wide energy region (see previous section and Fig. 4.16). The same simulation of the setup will be used to obtain the response function. By using this method, only the physical effects are considered and therefore it can be extended over the full experimental spectrum as the single-α detection is in the same energy range than the calibration source.

Since the response function depends on the energy of the particle detected, a set of simulations up to the maximum energy expected in the experiment have been done, discretizing the energy window in bins of 20 keV. To obtain the response matrix for the α-source, only the intrinsic resolution of each detector has been required in the analysis. For the ^{8}B case, the response matrix is calculated, not for mono-energetic α, but for the 2-α breakup of all the possible states populated in the β-decay of ^{8}B. Furthermore, it is analysed using α-α coincidence as the experimental data, with the kinematic and energy conditions defined in Sec. 5.1.

The response matrix includes the energy loss in the dead layers as a function of the pixel analysed and, for the ^{8}B-decay, the response function also includes the recoil broadening (β decay kinematics) and the energy loss in the C-foil. For each of the cases above (two for the α-source and one for the ^{8}B) a response matrix has been calculated using the GEANT4 simulation code.

The upper panel of Fig. 4.18 shows the response matrix of the U6 detector to mono-energetic α particles. The lower panel of the same figure shows the response of the U2-U6 detector pair to the β-decay of the ^{8}B applying the same coincidence condition as have been applied to the data (Sec. 5.1). Comparing the two figures one can see the effect of the coincidence restrictions, where the lower energetic tails of the response matrix (see insets) are completely suppressed. For the ^{8}B response matrix, a small fraction ($< 0.01\%$) of low energetic β-contribution remains.

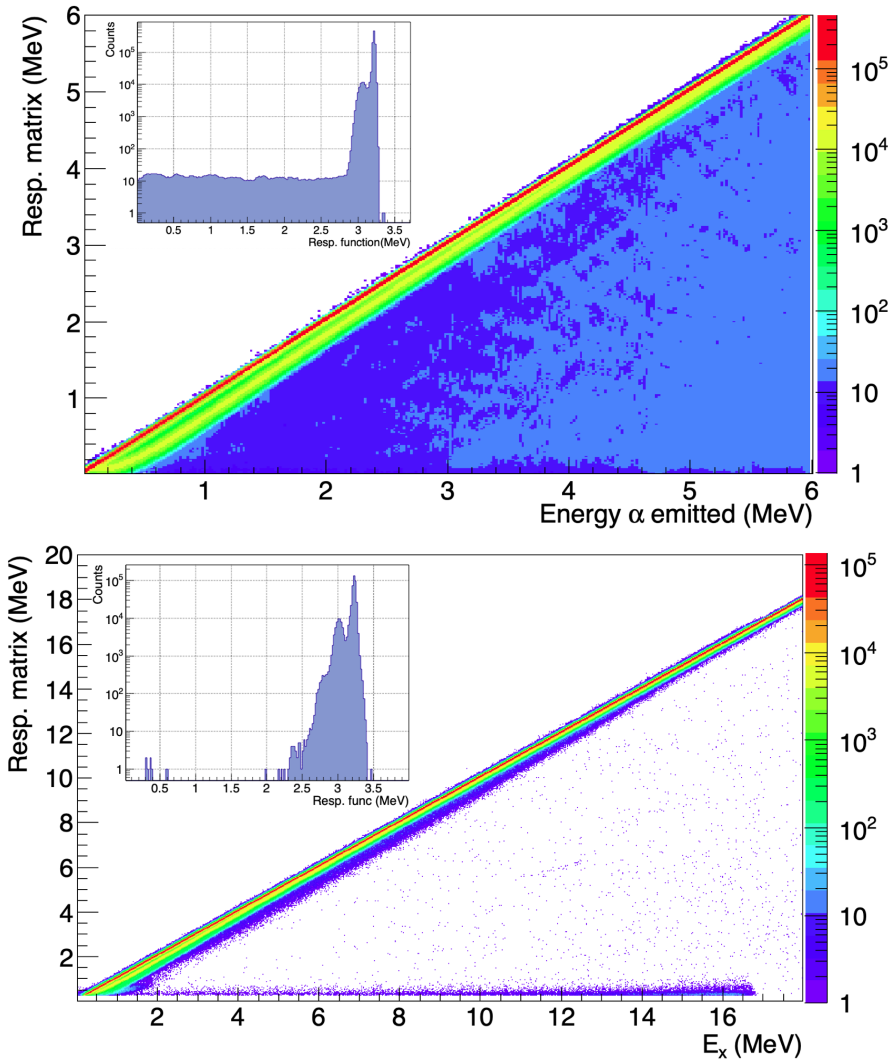

Figure 4.18: Response matrices obtained with GEANT4. In the upper panel, the response matrix of U6 (60 μm) to mono-energetic α-particles. The response matrix is analysed without conditions. The insert is the response function at the energy of ^{148}Gd peak. In the lower panel, the response matrix of the 60 μm detectors (U2 and U6) to the β-decay of ^{8}B as a function of the excitation energy of ^{8}Be. The response matrix is analysed with the same coincidence conditions than the experimental data (see Sec. 5.1 for details). The insert is the response function at 3.140(10) MeV, which is the main excitation energy populated in ^{8}Be.

4.3.5 Efficiency of the setup

With the previous work of simulation and characterization of the setup, the efficiency of the setup can be studied with different conditions.

The intrinsic detection efficiency of a DSSD can be considered to be 100%, so we will not discuss this aspect in this section. Then, the geometrical efficiency of the setup used in the IS633 experiment is the solid angle covered by the 5 DSSD i.e. the efficiency of detecting a single α particle. Fig. 4.19 shows the efficiency of the setup for the simulation of α particles at different energies (every 500 keV). The curve has been obtained simulating 1.000.000 α particles. The total efficiency to detect an α particle as a function of the energy is roughly constant and equals to 50.2(1)% of 4π (that corresponds to the solid angle covered).

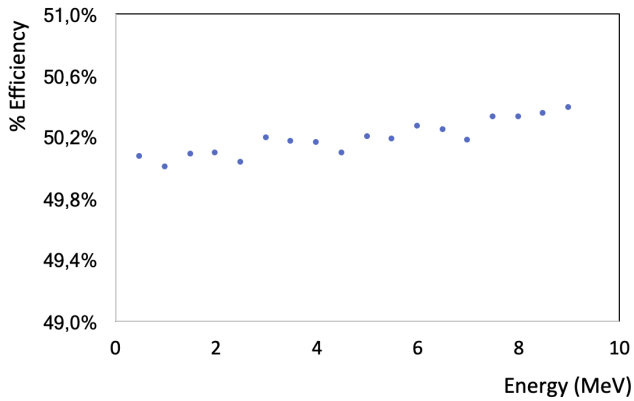

Figure 4.19: Total efficiency of the setup (5 DSSD) as a function of the energy of an α particle. Curve obtained simulating in GEANT4 1.000.000 α-particles discretizing the energy in 500 keV energy bins.

For the coincidence efficiency, the setup is reduced to the four DSSD that are involved in the coincidence analysis. Fig 4.20 shows the coincidence efficiency of the setup. The curve has been calculated simulating in GEANT4 1.000.000 β-decays of ^{8}B in the catcher position obtained in the previous section and with an energy obtained discretizing the Q-value in 20 keV energy bins. The simulations have been analysed removing the n-strip 15 of U6 and applying the same conditions as in the ^{8}B data (see Sec. 5.1), where only detectors U2 and U6 (60

μm) are considered for the coincidence. The efficiency of the α-α-coincidence for β-feeding at 3 MeV (the main decay) is 44.4(1)%. As for the single detection, above 500 keV the curve is practically flat. One would believe that the efficiency of the α-α coincidence would be much less than the single α efficiency. However, due to the kinematics of the breakup, the emission of the two α is roughly at 180° and once one α is detected, the efficiency of detecting the other is close to 100%.

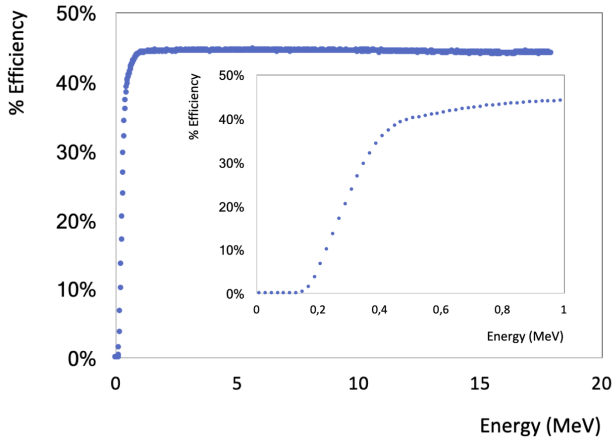

Figure 4.20: α-α coincidence efficiency of the setup (4 DSSD) as a function of the energy. Curve obtained simulating in GEANT4 1.000.000 events of ^{8}B β-decay discretizing the Q_{ec} window in 20 keV energy bins.

4.4 DATA-SETS

During the experiment, two sets of data with different electronic conditions and ^{8}B production were recorded. The sets can be described as:

- Electronic thresholds at 250 keV and a 40% of deadtime: This data set was used to assure that the yield of ^{8}B was sufficient and that the spectrum had the expected shape. During 52 hours and 18 minutes, 81 GB of data were taken. The proton current was 0.8(2) μA.
- Electronic thresholds at 2.5 MeV and 10% of deadtime: The raise of the thresholds was done to maximise the statistics at the higher energetic region and also decrease the deadtime present in the data. During 50 hours and 28 minutes, 27 GB of data were taken. The proton current was increased to 1.6(2) μA.

The deadtime during the experiment has been studied comparing the total amount of triggers received against the accepted triggers. The distribution along the time is shown in Fig. 4.21. The green zones correspond to the low electronic thresholds configuration. The red zone limits the configuration with the electronic thresholds increased at 2.5 MeV.

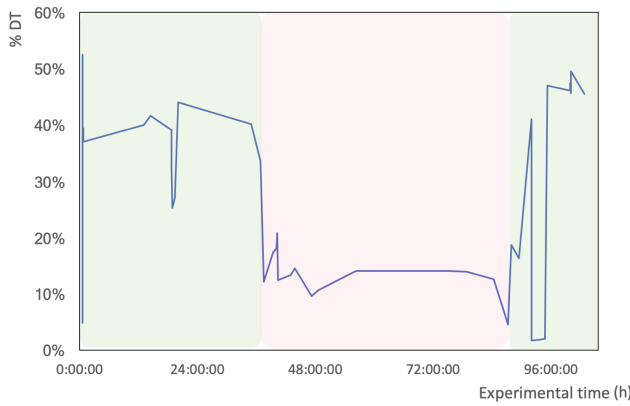

Figure 4.21: Deadtime distribution along the experimental time in hours. The green zones have the electronic thresholds set at 250 keV. The red zone has the electronic thresholds at 2.5 MeV.

Each data-set has been analysed independently with the conditions defined in Sec. 5.1. Fig. 4.22 shows the sum of all the statistics of the α-α coincidence on the 60 μm detectors. The spectrum of the data-set with the electronic thresholds set at 250 keV is represented in blue and in red the data-set with the electronic thresholds at 2.5 MeV. Due to the high thresholds on the second set, the spectrum is distorted at the low energy range and cannot be added directly. The counts present below 6 MeV in the data-set with high thresholds are registered due to threshold effects. The electronic module that defined the thresholds in each detector is a Leading Edge CFD, designed mainly for cutting the low energy channels. As for the data-taking the thresholds were increased over the common limits, it is not clear the efficiency of the thresholds. Moreover, the electronic thresholds are not sharp and can let pass signals below the threshold set.

As our aim is the high energy part of the spectrum, we need to use the data-set with the thresholds increased as the main contribution to this region comes from this data-set. In order to include this data-set, we need first to correct the distortion present due to the high thresholds. To do that, the range from 6 to 8 MeV of both spectra has been integrated and scaled. Once the factor is obtained, the low energy part of the data-set with the low thresholds is scaled to the high thresholds one. Figure 4.23 shows the α-α coincidence spectra for the data-set with low thresholds (blue), the data-set with the thresholds at 2.5 MeV already corrected (red) and the sum of all the statistics once the data-set is corrected (green).

The errors associated to the data are propagated consequently to the process explained.

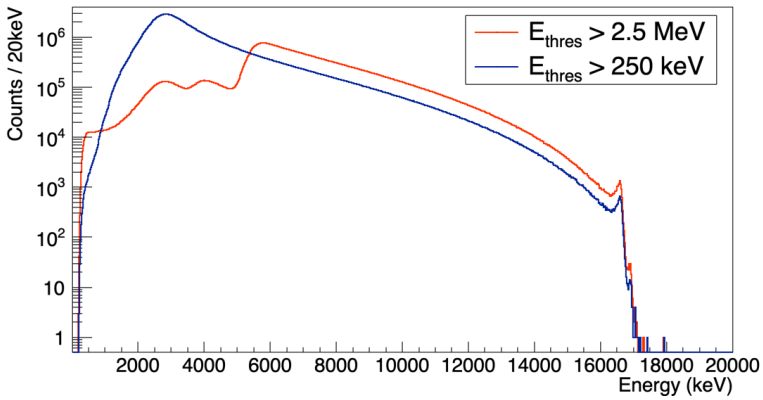

Figure 4.22: α-α coincidence (60 μm detectors). In blue, the data with the electronic thresholds at 250 keV. In red, the data with the electronic thresholds at 2.5 MeV.

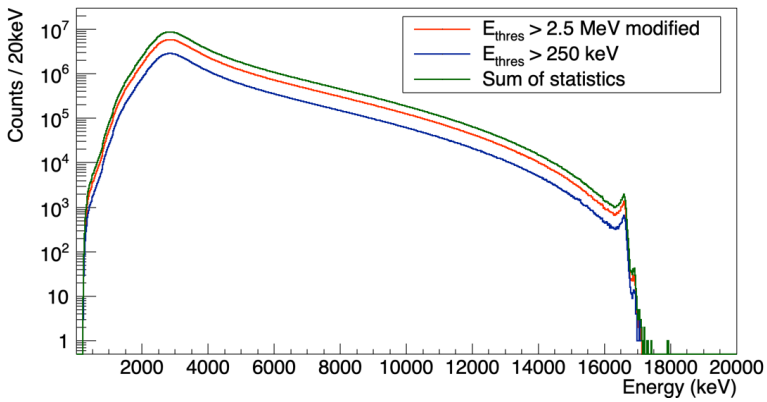

Figure 4.23: α-α coincidence (60 μm detectors). In blue, the data with the electronic thresholds at 250 keV. In red, the high thresholds data-set corrected. In green, the sum of all the statistics.

Analysis of α-particles

5

5.1 COINCIDENCE CONDITIONS

The aim of this work is to study the ^{8}Be excitation spectrum through the β/EC-decay from ^{8}B. In order to obtain the excitation spectrum, a reconstruction of the energy levels populated in ^{8}Be is done through the α-α coincidence detection that comes from the breakup of the ^{8}Be. In this context, we define the excitation spectrum of ^{8}Be as the spectrum which is corrected by the energy of the recoil and the separation energy of the two α. Two different conditions have been applied to the data (and to the simulation): kinematic conditions and energy conditions, to assure that the two α's detected in coincidence are coming from the same β-decay.

On one hand, the kinematic conditions have been studied using the GEANT4 G4RadiactiveDecay event generator not including the geometry of the setup. Like this, information about the emission angle and the energy of the recoil is obtained. This is presented in Sec. 5.1.1.

On the other hand, the energy conditions, which have been defined including the setup defined as in Sec. 4.3.3 in the simulation in order to define the energy cuts to be applied to the data (Sec. 5.1.2).

5.1.1 Kinematic conditions

The ^{8}B nucleus is implanted in the C-foil and the β-decay occurs at rest. In the β-decay, the daughter nucleus (^{8}Be) gets a recoil-energy (E_{recoil}) between 0 and 20 keV depending on the energy of the emitted β particle. Fig. 5.1 shows the energy distribution of the daughter nucleus as a function of the excitation energy of the ^{8}Be, simulating 10^6 ^{8}B β-decays per bin. The Z-axis (colour scale) represents the number of events for each recoil energy. As we can see in the figure, for β-population above 15 MeV, the recoil energy is negligible.

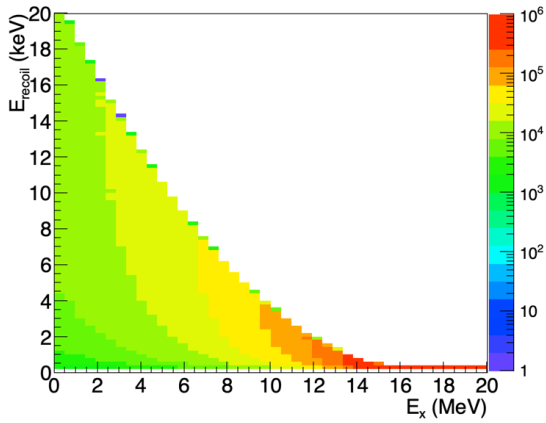

Figure 5.1: Recoil-energy distribution of the ^{8}Be nucleus as a function of the excitation energy following the β-decay of ^{8}B. 10^6 ^{8}B β-decays have been simulated per bin. Z-axis (colour scale) represents the number of events for each recoil energy.

The 2α emitted in the breakup of the ^{8}Be nucleus have, in the rest frame of the daughter nucleus, the same kinetic energy but they are emitted in opposite directions. In the laboratory frame, the trajectory of the α is affected by the β-decay recoil of the mother nucleus as the breakup of ^{8}Be into two α does not really happen at rest. The recoil implies a change of the trajectory that, in the laboratory frame, produces a variation on the 180° emission angle between the two α. Fig. 5.2 shows the emission angle between the two α in the laboratory frame as a function of the excitation energy of the populated level. More than 90% of the ^{8}Be break up occurs within an emission angle between the two α's

of 180(5)°.

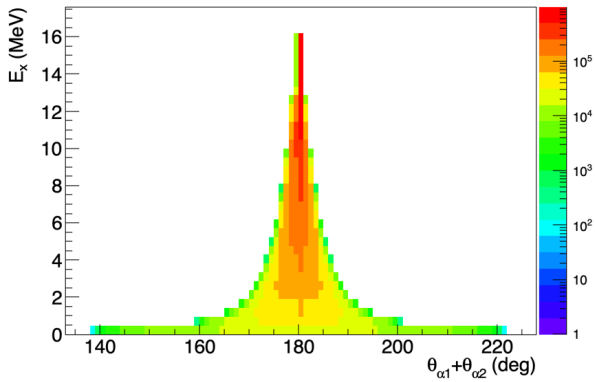

Figure 5.2: Simulation of the opening angle (θ) between the two α after the ^{8}Be breakup in the laboratory frame. The Y-axis is the excitation energy of the ^{8}Be nucleus. More than 90% of the ^{8}Be breakup occurs within an emission angle between the two α's of 180(5)°.

As kinematic condition, the analysis requires that the alphas are emitted from the beam-spot defined in Sec. 4.3.2. The beam-spot has been defined large enough to create a cone in the DSSD that includes the maximum deviation on the angle between the two α. Geometrically, this condition is applied tracing a straight line between the two α that cross the C-foil. If the interaction point with the C-foil is inside the beam-spot, the coincidence is accepted. Fig. 5.3 shows a sketch of how is defined the straight line. The left panel shows the situation when the two α are emitted within the tolerance on the emission angle defined. The right panel, when the geometric condition is not met. As the beam-spot is not punctual, a pixel of one detector is correlated with a 3×3 pixel region in the opposite detector. This condition is useful for events with more than one decay, as it allows to relate each α with its partner.

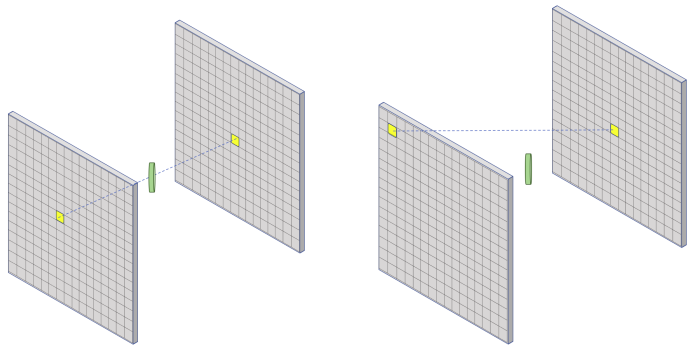

(a) Two α detected within the geometric condition

(b) Two α detected excluded due to the geometric condition

Figure 5.3: Scheme of the geometrical condition for an α-α coincidence. The left panel shows the case where two α are detected within the tolerance of the emission angle. The right panel shows two α detected that do not meet the geometric condition.

5.1.2 Energy conditions

The two α's following the breakup are emitted with equal energy within a stochastic distribution due to different aspects already discussed like the recoil energy.

As a preliminary condition to get the beam-spot of the ^{8}B implantation, a ΔE = 200 keV between the two detected α was chosen. Now, an improvement of the tolerance as a function of the energy difference between the two α's can be performed by means of a GEANT4 simulation, thus obtaining a realistic value for the $\Delta E(E_{\alpha_1},E_{\alpha_2})$. Figure 5.4 is the representation of the energy of each pair of α's detected in the 60 μm detectors (U2 and U6). The narrow distribution of the figure allows us to define the good events as the ones inside the black polyhedron of the diagonal, removing the contribution of α-α coincidence partially detected. This polyhedron will be used in the following analysis of the ^{8}B data.

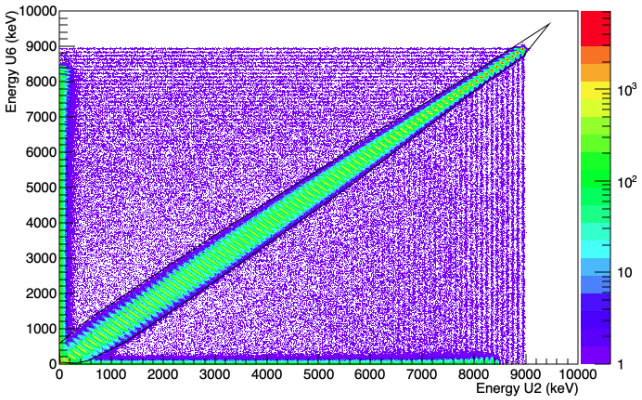

Figure 5.4: Energy deposited in U6 vs energy deposited in U2 for a GEANT4 simulation of the ^{8}B β-decay. The energy condition defined is the black polyhedron in the diagonal, where the β contribution and the events where only one of the α's are detected are excluded.

5.2 PILE-UP AND SUMMING ANALYSIS

For the ^{8}B β-decay, three different effects may occur that produce a distortion of the spectrum:

- Pile-up of an α and a β produced due to random coincidence between an α and a β from different decays.
- Pile-up of two α produced due to random coincidence between two α from different decays.
- Summing of an α and a β produced due to the coincidence of two or more particles from the same decay.

The case of the pile-up of an α and a β from two different decays is excluded from a pile-up study as the thickness of the DSSD (40 μm and 60 μm) is not enough for the β to deposit more than few keV, which is not significant since the binning of the histograms is 20 keV/ch. Fig. 5.5 shows the maximum energy deposited in a DSSD by a β as a function of the energy level populated in ^{8}Be for the 60 μm detectors. The distributions have been obtained simulating 100.000 ^{8}B decays into the setup. In the region from 2 to 4 MeV, where most of the decays occur (high data rate), less than 4.4% of the total amount of β deposit more than 20 keV in the detector which will imply a displacement of one bin (pile-up). For the 40 μm detectors, the energy deposited by the β is even less.

The summing of an α and a β from the same decay is corrected at a later stage, either by unfolding or in the R-Matrix analysis, since this effect is included in the response function of the detector. It is an effect that depens on the geometry as it is proportional to the solid angle of each pixel and also will appear in the GEANT4 simulation. This will be discussed in detail in Sec. 4.3.4.

The pile-up of two α is the one that will produce the largest deviation on the energy detected. This effect is due to the high data rate in the experiment. The ^{8}Be daughter nucleus breaks up into two α that are emitted roughly at 180° due to the kinematics of the breakup. Since the aim is to obtain the ^{8}Be excitation spectrum, the analysis of the pile-up produced by two consecutive decays has to be done with the constrains used to obtain the spectrum. This effect will be studied in detail through different but complementary methods in the next subsections. First, a statistical study of the amount of double (or even more) decays in the same ADC time window (or event) will provide an

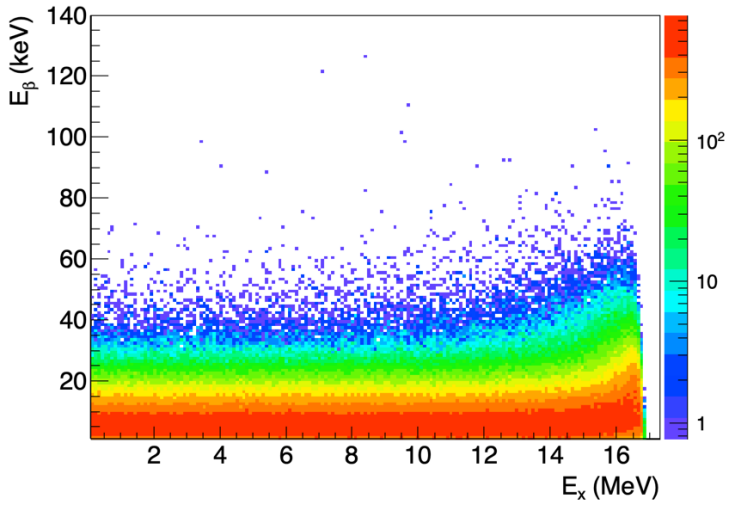

Figure 5.5: Distribution of the energy deposited by a β as a function of the excitation energy of ^{8}Be that gets populated in the decay for the 60 μm detectors used in the IS633 experiment.

estimation of the percentage of pile-up in the ^{8}Be excitation spectrum. Later, to understand how the pile-up is distributed in energy, a code that reproduces the treatment of the ADC signals will be used to recreate a pile-up spectrum. Finally, an exhaustive study of the events at higher energies above the Q-value (above 17 MeV) will be performed.

5.2.1 Evaluation of the amount of pile-up

For the statistical study, the ^{8}Be excitation spectrum will be considered for the 60 μm DSSDs since these detectors are thick enough to stop all α particles emitted in the decay.

One of the issues of having a high rate of decays during the experiment is that more than one decay can occur during the ADC time window, 4 μs, defined by the acquisition system. In the IS633 experiment, the average rate during the experiment was 25.000 counts/s and therefore it is necessary to know statistically how the events are distributed concerning the amount of particles detected in each detector per event. Furthermore, since the final aim is to obtain the excitation-spectrum of ^{8}Be, the amount of pile-up has to be checked once the coincidence constrains are implemented (defined in Sec. 5.1) because they exclude many events with two or more detections in one DSSD for geometrical or energetic conditions.

To obtain the statistics, the average of 50 files of each set of data defined in Sec. 4.4 is calculated. The proportion of α-α coincidences detected with more than one hit in one of the detectors, with respect the total coincidences, is detailed in Tab. 5.1, where the two sets of data analysed are treated individually. For the estimation of the pile-up counts in the α-α spectrum, the maximum ratio of double hits with respect to the total coincidences is used: $P_{double/total} = 3.95\%$.

Due to the very restrictive coincidence constrain in energy (see Sec. 5.1), only the events with double detection in both detectors of the coincidence are studied. The case of two α-detections in one detector and one in the opposite will not produce a coincidence as the energy detected in the double detection will be larger than the tolerance fixed on the energy constrain ΔE<200 keV.

In order to study the double detection in both detectors, a geometry factor,

Table 5.1: Proportion of coincidences with more than one hit per detector with respect to the total coincidences for each set of data.

Detector	$\mathbf{E}_{thres.} > \mathbf{250\ keV}$	$\mathbf{E}_{thres.} > \mathbf{2.5\ MeV}$
60μm coincidence	1.98(24) %	3.95(65)%
40μm coincidence	0.40(6) %	0.72(12)%

representing the probability to detect the 4α in the two same pixels has to be calculated. The counts of pile-up in the coincidence spectrum can be calculated as equation 5.1, where G is the geometry factor, $P_{double/total}$ the proportion between the double/total coincidence detections and N_{events} the total coincidences on the experimental α-α spectrum.

$$C_{pile-up} = G \times P_{double/total} \times N_{events} \tag{5.1}$$

To calculate the geometry factor (G), let us consider an event with two simultaneous decays. If only the α particles are considered, the first $\alpha_{1,1}$ is detected in the pixel of detector U2 with p-strip number 8 and n-strip number 7. Due to the kinematics of the ^{8}Be breakup, the $\alpha_{1,2}$ of the first decay is detected in the pixel of detector U6 with p-strip number 9 and n-strip number 8. In the second decay, the first α emitted, $\alpha_{2,1}$, is detected in the same pixel than $\alpha_{1,1}$. Then, due to the kinematics, and because the implantation is not exactly point-like (see Sec. 4.3.2), the second $\alpha_{2,2}$ will be detected in a region of 9 pixels around the pixel where $\alpha_{1,2}$ was detected in U6. It can be concluded that once the $\alpha_{2,1}$ is detected in the same pixel in U2 than $\alpha_{1,1}$, we estimate a $1/9$ probability that the $\alpha_{2,2}$ will be detected in the same pixel than $\alpha_{1,2}$.

Following the example explained and knowing that the solid angle covered by the central pixel of U2 (which covers the maximum solid angle per pixel) respect to the total solid angle covered by the detector is 4.98×10^{-3}, the geometry factor (G) of having double detection in both detectors in the same pixels is $4.98\times10^{-3}\cdot\frac{1}{9}=5.53\times10^{-4}$. The total amount of counts in the α-α coincidence spectrum (N_{events}) is 9.6×10^{8} and $P_{double/total}$ is 3.95%. Therefore we expect a total of 20983 pile-up counts distributed over all the spectrum, which is a 0.0022% of the total amount of counts.

5.2.2 Shape of the pile-up spectrum

Once the amount of pile-up in the spectrum is determined, it is necessary to know how it is distributed and therefore calculate the shape of the pile-up spectrum as a function of the energy.

Before getting into the details of the program, a summary about how the electronic signals are treated by the ADC will be explained. Once a particle is detected in a detector, the charge generated due to the ionisation produced by the particle is collected. After the amplification of the signal, it is sent to an ADC where the signal is processed and converted into a digital number that can be read and saved. The ADC's used in the IS633 experiment are a peak-sensing ADC, which is based on the conversion into a digital signal of the maximum height of the gaussian input pulse.

If two signals arrived within the same time interval but with enough space between them to not overlap, the resultant signal processed in the amplifier will be the integral during the amplifier shapping time of the first signal produced in the pre-amplifier. Therefore, the conversion of the signal in the ADC will not be affected by pile-up. However, if the two signals in the preamplifier are close enough, the integral obtained will be higher, producing a signal to the ADC that is not the sum of the particles that have been detected. Fig. 5.6 shows a scheme of how the pile-up is produced in the electronic chain. In the upper panel, the cases of two signals that do not produce pile-up. In the lower panel, the resultant signal of a pile-up event.

To calculate the pile-up spectrum, a program based on how the digital signals are obtained is used. The program starts with the experimental spectrum, from where the pile-up spectrum wants to be inferred, to convert it into a cumulative distribution function. Defining the ADC time window as 4 μs and the shapping time as 2 μs (which will be the σ of the gaussian signals), the program produces two random numbers to generate the signals within the time window defined. The height of both signals is determined with another two random numbers to sample the cumulative distribution created before. Using Root, both signals are added and the height of the resultant function is the energy of the pile-up count.

Repeating this process enough to have statistics, the shape of the pile-up spectrum is produced. In order to obtain the spectrum of the pile-up, a normalisation has to be applied to adjust it to the experimental spectrum. For

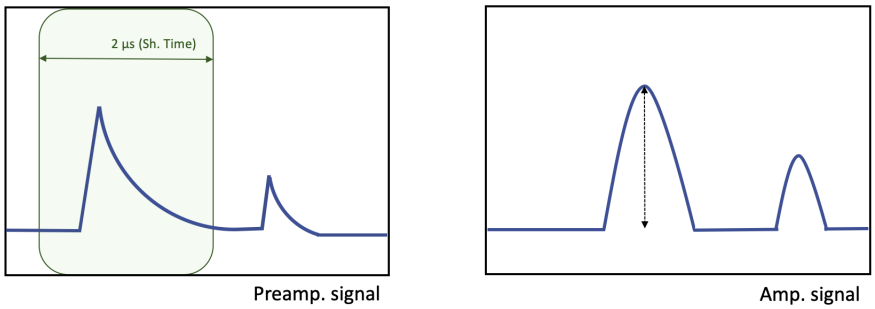

(a) Two signals far enough in time do not have overlap between them.

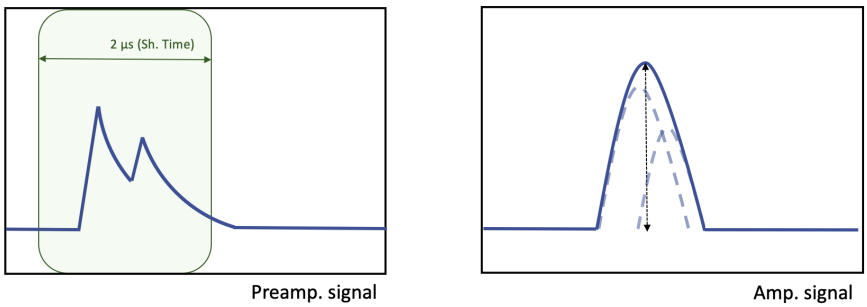

(b) Two signals within the time window close enough to produce pile-up. The signal processed by the amplifier will be higher than what corresponds to the ionisation produced by one particle.

Figure 5.6: Scheme of two independent signals distributed within the shaping time of the amplifier and the resultant signal that will be processed.

this normalisation, the amount of pile-up calculated statistically in the previous section is used. Fig. 5.7 shows the pile-up spectrum in red and the ^{8}Be excitation spectrum obtained experimentally in blue. As can be seen, the effect of the pile-up on the shape of the experimental spectrum is negligible (note the log scale).

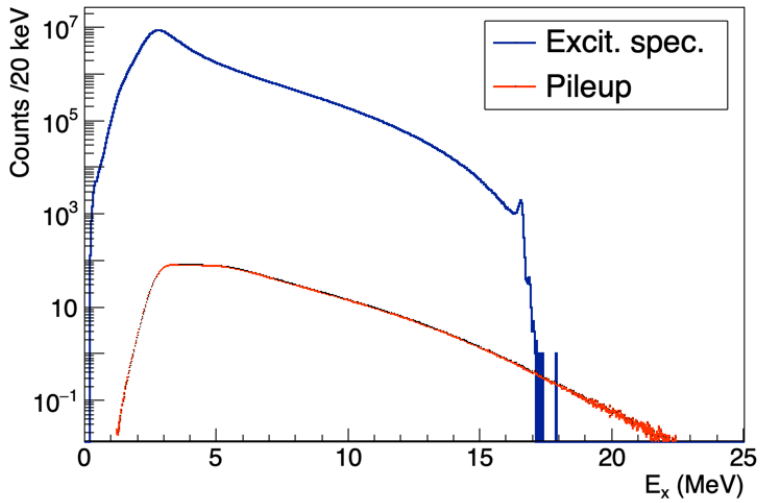

Figure 5.7: In red, the pile-up spectrum normalised to the amount of pile-up calculated statistically. In blue, the excitation spectrum of ^{8}Be obtained from the 60 μm detectors. Note the logarithmic scale.

Using the normalisation calculated previously, the integral of the pile-up spectrum above the Q-value and up to 18.5 MeV (the dynamic range of the 60 μm detectors as set during the experiment) is 7 counts, which is in perfect agreement with the extra counts suspicious to be pile-up in the ^{8}Be excitation spectrum.

5.2.3 Study of the events above the Q-value

With the two previous sections, it has been proven that the pile-up estimated for the spectrum is insignificant. Anyhow, and due to the low statistics above 16.9 MeV, it is mandatory to carefully study these events, mainly the ones that are suspicious to be pile-up as are above the Q_{EC}-value of the decay (Q_{EC}=17979.9(10) keV). Fig. 5.8 presents a zoom on the region of interest for this section.

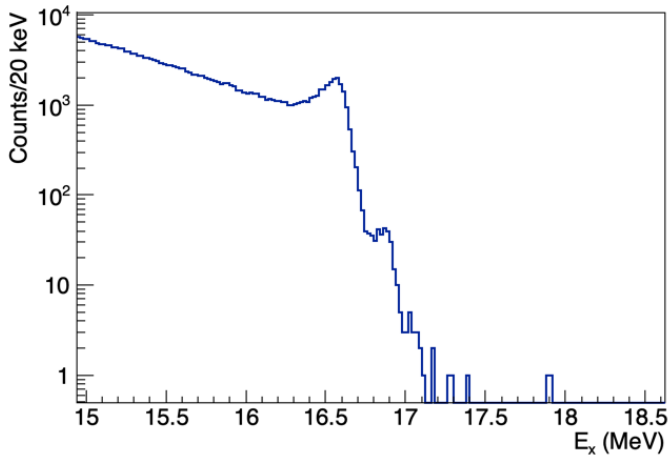

Figure 5.8: Zoom on the high-energy range of the excitation spectrum of ^{8}Be on the 60 μm detectors (U2 and U6). The events above 17.1 MeV are suspicious to be pile-up.

The study is focused on estimating the fraction of β in coincidence with the 2α that are part of the α-α coincidence in our analysis. In principle, the higher the energy of the level populated in ^{8}Be (and therefore, as higher the energy of the α detected), the lower fraction of β should be detected as the decay will be dominated by electron capture (EC). For the 16.6 MeV state populated in ^{8}Be, the fraction of β-decay to this level is 95%, however, for the 16.9 MeV, the β-decay process falls down to 3%. Fig. 5.9 shows how the population via β-decay and EC vary as a function of the excitation energy in ^{8}Be, calculated with LOGFT.for code [nds]. For decays above 16.940 MeV, only EC is present

and no β-particle should be detected. If a β is detected, this is a clear indication that the events above 16.94 MeV are pile-up.

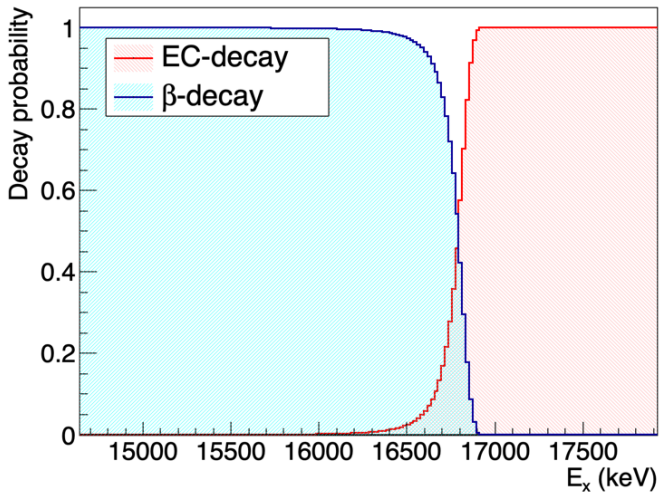

Figure 5.9: Calculated phase space fraction of β-decay (blue) and electron capture (red) as a function of the excitation spectrum in ^{8}Be.

The triple coincidences (α-α-β) are differentiated in five regions (see Fig. 5.9) considering the Q_β, the Q_{EC} and the resolution of the detector:

- Coincidences below the 16.6 MeV state, defined as the region comprised between 14.4 and 16.37 MeV. (a)
- Coincidences from the 16.6 MeV state, defined as the region comprised between 16.37 and 16.8 MeV. (b)
- Coincidences from the 16.9 MeV state, defined as the region comprised between 16.8 and 17.04 MeV. (c)
- Coincidences above the Q_β-value (Q_{EC}-1022 keV = 16957.9 keV), defined as the region comprised between 17.04 and 18.5 MeV. This region can be further divided into two:

- From 17.04 to 17.2 MeV, as it has a peak structure. (d)
- From 17.2 MeV to 18.5 MeV. (e)

In Fig. 5.10 one can see the fraction of triple coincidence α-α-β to α-α coincidence in the regions defined above due to the low statistics on the 60 μm detectors overlayed to the β-decay fraction calculated in Fig. 5.9. If the α-α-β events are physical (the three particles belong to the same decay), the red spots ($\alpha\alpha\beta/\alpha\alpha$ fraction) should follow the trend of the β-fraction and, in this case, these events have to be considered in the analysis. If they are out of the trend of the β-fraction they should be regarded as pile-up and rejected. In green, the ^{8}Be excitation spectrum in arbitrary units just to guide the eye and distinguish the different regions on the spectrum. The β-coincidence is required in any of the PADs and in anti-coincidence with the 40 μm detectors to ensure that the coincidence is purely β-coincidence and not an energetic α passing through the thinner detectors.

Region **a** has been used to normalise the β-decay fraction (from Fig. 5.9) to the solid angle covered by the detectors and the loss in the statistics due to the constrains.

Region **b** presents a lower β-contribution than expected due to the definition of the region, as it includes higher energetic decays that will contribute with less β-particles to the 16.6 MeV peak. However, it follows the trend in the energy region defined. Region **c** also follows the trend of the blue curve. Both regions can be identified as physical β-decay events.

Region **d** and **e** will be studied event per event as the error bars are so large that it is not possible to obtain a clear conclusion from the figure.

On one hand, for the region **d** comprised between 17.04 and 17.2 MeV, 16 α-α coincidences and 3 β-α-α coincidences are detected. The β are detected in the PADs. The three triple coincidences are considered pile-up and removed, as a decay on that energy should not be in coincidence with a β. The remaining events will be considered physical and included in the following analysis.

On the other hand, for the region **e**, which is above 17.2 MeV, 6 α-α coincidences and 1 β-α-α coincidence are detected. Due to the random distribution along the region and the good agreement with the amount of pile-up counts on the region calculated in the previous section, the 7 events are considered pile-up

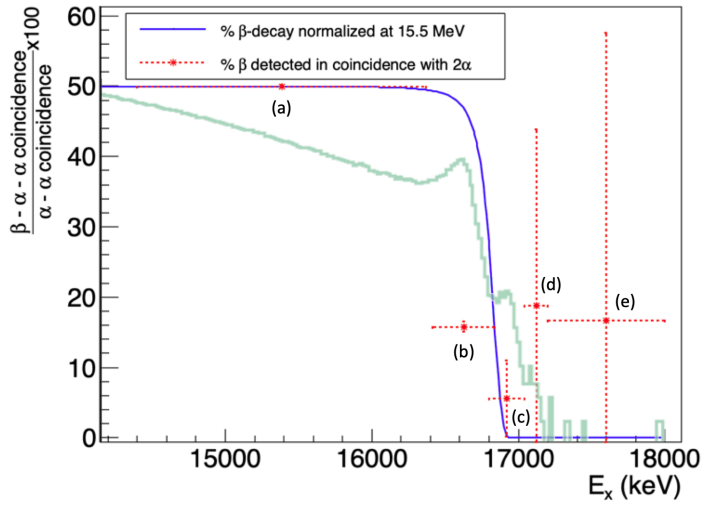

Figure 5.10: Fraction of triple coincidence α-α-β to α-α coincidence in the regions defined in the text on the 60 μm detectors overlayed with the β-decay fraction. In blue, the percentage of β-decay normalised to the fraction of β in coincidence with 2α below the 16.6 MeV region. In red, the percentage fraction of α-α-β coincidences to the total number of α-α coincidences for the 5 regions defined in text. The letters are used to explain the figure in the text per regions. The green spectrum is with arbitrary units and only to guide the eye and distinguish the regions on the ^{8}Be excitation spectrum.

and will be removed from future spectra.

5.3 HALF-LIFE OF ^{8}B

A measurement of the half-life provides one of the observables needed for the determination of the nuclear structure, including the B_{GT} of the transition to the states populated in the β^+/EC-decay. The previous value found in the literature, prior to this work, for the half-life of ^{8}B was 770(3) ms [ASL74]. However, these measurements date back to the 70's and one would expect that with present statistics and new techniques an improvement in the precision can be obtained.

The half-life of the nuclei can be extracted experimentally by fitting the exponential curve of the amount of decays observed in our setup as a function of time. Once the source is implanted, and if there is no other implantation afterwards, the counting rate of the detectors will decrease exponentially following the decay-law prediction (Eq. 5.2)

$$A = A_0 e^{-\lambda t} \tag{5.2}$$

where A is the activity of the nucleus at the measurement time (t), A_0 is the initial activity and λ is the parameter correlated with the half-life ($T_{1/2}$) as is shown in equation 5.3.

$$T_{1/2} = \frac{ln2}{\lambda} \tag{5.3}$$

The decay of ^{8}B is correlated in time with the proton pulses arriving at the ISOLDE target unit. For the half-life measurement, the PS-Booster was running with a supercycle of 36 proton pulses over 43.2 s, having an interval between pulses of 1.2 s. Seven equidistant pulses in the supercycle were selected so that the time between each pulse ($5\times1.2s = 6s$) is longer than 6.5 times the half-life. With the proton request condition, the reduced proton current on target (1.6 μA) and the electronic thresholds set to 2.5 MeV, the dead time of our system calculated with the accepted triggers from the DAQ was 4.48(8)% at the implantation time.

In Fig. 5.11 the clock signal for the two different request of protons is shown. On the left, the clock signal which was used during most part of the experiment, where the beam gate is fully open all the time and the pulses arrive at the primary target every 1.2 seconds. On the right, the clock signal for the half-life measurement, where a beam-gate of 100 ms was set and can be seen

the decay of the nucleus to extract the λ parameter by fitting the next 5 seconds.

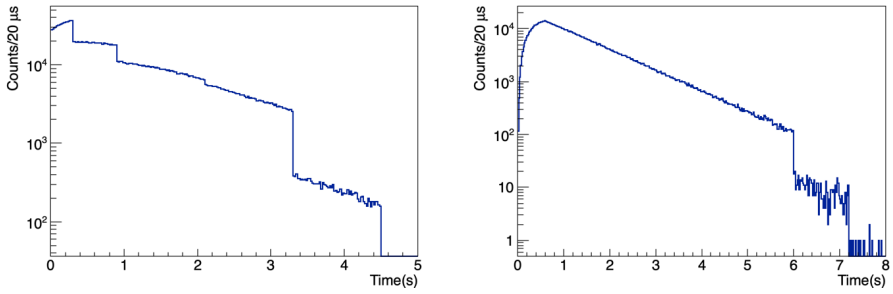

(a) (b)

Figure 5.11: Clock signal for the two different conditions of measurement. On the left (a), the standard conditions with the protons impacting on the primary target every 1.2 seconds many times, every 2.4 s less often and so on. On the right (b), the cycle of the protons modified with a beam-gate of 1 s to measure the half-life of the collected ^{8}B nuclei during the remaining 5 s.

The configuration of the setup in combination with the characteristics of the ^{8}B decay allowed for three independent measurements and analysis of the half-life to be performed.

From the two pairs of DSSDs facing each other, two independent α-α-coincidence spectra can be analyzed. The coincidence constrains are the same as the ones explained in Sec. 5.1 and, as an extra condition, in order to avoid possible effects of the high thresholds or punch through of the most energetic α-particles detected by the 40 μm detector-pair, the range of the coincidence was fixed to the energy interval 7 to 14 MeV.

Moreover, from the 1000 μm detector placed below the catcher foil, both α and β particles are detected and, by gating above the β-contribution, an independent single-α spectrum is obtained. The energy range considered in this case is above 4 MeV.

In order to obtain an accurate result and improve the uncertainty, the data

is corrected for dead time. Since the dead time will decrease with the activity of the nucleus, the correction has been done bin per bin. The correction applied follows Eq. 5.4, where λ is the published decay constant derived from the ^{8}B half-life and τ is the time after the implantation. The maximum dead time of the system, DT_0, is 4.48% and occurs at the arrival of each implantation. Eq. 5.5 is the correction applied to the amount of $\alpha - \alpha$ coincidences considered for the half-life measurement in each bin.

$$DT = DT_0 e^{-\lambda\tau} \tag{5.4}$$

$$N_{corrected} = N_{meas}(1 + DT) \tag{5.5}$$

As mentioned in Sec. 3.1, the release time of the ^{8}B nucleus from the primary target of ISOLDE has to be taken into account for the determination of the half-life. To avoid the effects of this release-time, the beam-gate was opened to start the collection 5 ms after the protons impacted on the ISOLDE target (the time for the HV to recover), left opened for 1 s, and then closed, in order to follow the decay of the collected ^{8}B source. In addition, a suppression of the first hundred of milliseconds is done in order to have less dead time in the acquisition system: at the implantation time, DT_0 is 4.48%. We thus delayed the start of the analysis 600 ms after the source collection, when the dead-time is only 1%. This dead-time drops to 0.1% in the following 3 s.

In Fig. 5.12 one can see the time spectrum corrected by dead-time of the α-α coincidence seen in the 60 μm DSSD (in blue) and the fit to an exponential decay function to extract the half-life (in red). The relative residuals of the fitted region are presented. The extra counts above 6 s correspond to some cycles where instead of seven, eight pulses have been delivered. These events are not considered in the analysis.

For the three measurements, the results obtained with the fit are:

- α-α coincidence in the 60 μm DSSD-pair: $T_{1/2}$=771.9(17) ms (χ^2/dof=1.10)
- α-α coincidence in the 40 μm DSSD-pair: $T_{1/2}$=773.9(18) ms (χ^2/dof=1.19)
- α-singles in the 1000 μm DSSD: $T_{1/2}$=770.9(17) ms (χ^2/dof=1.15)

The weighted average of the three values is 772.2(10) ms. If we combine our value with the prior value from [ASL74], the result is 771.95(95) ms, reducing

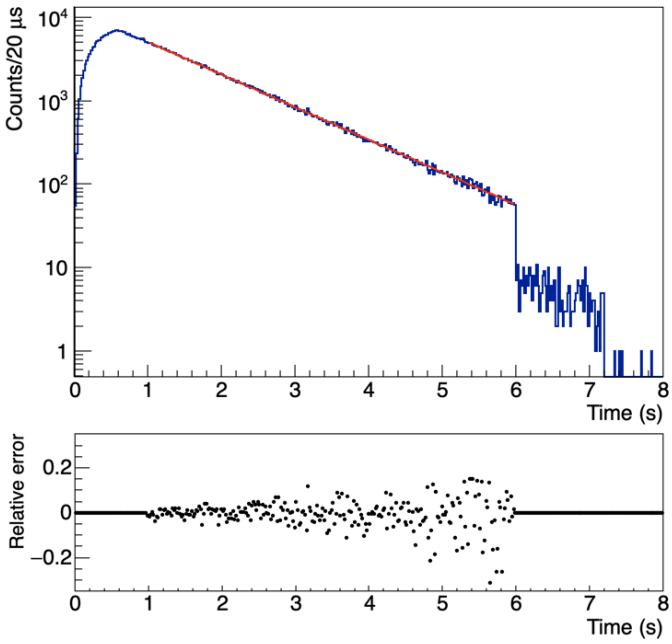

Figure 5.12: Upper panel: Time spectrum of the α-α coincidence in the 60 μm detector-pair using the upper energy sum range from 7 MeV to 14 MeV (blue histogram) and an exponential decay fit to the data (red line). Lower panel: relative residuals to the experimental data in the fitted region. The binning of both histograms is 20 μs.

the uncertainty of the half-life by a factor 3.1.

In order to ensure that no systematic errors are added when choosing the energy range of the α-coincidence, 7-14 MeV, we have checked that reducing this range to 8-13 MeV, the results obtained for the half-life are the same within the errors (larger in this latter case). Moreover, we have checked that the dead-time correction is not sensitive to the small change in λ due to the new value of the half-life obtained here.

5.4 R-MATRIX FRAMEWORK

The main goal of this thesis is to obtain the β-decay transition probabilities for the decay of ^{8}B into ^{8}Be, in particular, the B_{GT} and B_{F} to the isospin doublet at 16.6 and 16.9 MeV excitation energy never measured before. Due to the broad resonance at 3 MeV, the study cannot be done in the Breit-Wigner approximation. An R-matrix analysis will provide the configuration of the phase space for those states that have constructive and destructive interference between them, describing the nuclear resonances in therms of physical and meaningful parameters.

In this section, a brief description of the R-matrix theory will be presented. For more details and the mathematical description of the theory, see reference [LT58], and for a description focused on a β-decay process followed by two body-break-up, see the work of Barker [Bar69].

5.4.1 Introduction to R-Matrix

The R-matrix theory was formulated to resolve the nuclear resonances in reaction experiments, following the calculation of the cross section of the involved resonances. Later, in 1969, Barker adapted the theory to β-decay followed by two-body break up of the daughter nucleus.

It is based on considering the nuclear interaction in two regions. On one hand, the internal region where only the nuclear potential is present. On the other hand, the external region, which is purely governed by the Coulomb interaction. The border between the two regions is defined by the channel radius, which can be calculated as Eq. 5.6

$$a_c = r_0(A_1^{\frac{1}{3}} + A_2^{\frac{1}{3}}), \tag{5.6}$$

where A_1 and A_2 are the mass number of the interacting nuclei. Due to the short range of the nuclear forces, the channel radius is of few fm.

The wave function of the external region of the nucleus, Ψ, for a certain number of channels, c, can be factorized as the sum of the wave function of each

channel, ψ_c, multiplied by the solution of the Schrödinger's equation, $u_c(r)$:

$$\Psi = \sum_c \psi_c u_c(r) \tag{5.7}$$

The external region of the nucleus is characterized by pure Coulomb interaction. The wave function of each channel includes the dependence with spin and angular momentum while the solution of the Schrödinger equation contains the dependence with the regular and irregular Coulomb functions.

For the internal region of the nucleus, the wave function can be expanded in terms of the internal eigenfunctions, which directly depend on the orthogonal eigenfunctions of the Schrödinger equation:

$$\Psi = \sum_\lambda C_\lambda X_\lambda \tag{5.8}$$

In the nuclear reaction framework, a collision matrix can be defined where each eigenvalue, λ, contributes with its energy, E_λ, and its reduced widths, $\gamma_{\lambda c}$. The energy dependence is in the shift and penetration functions, namely the real and imaginary part of the logarithmic derivative of the outgoing wave, that only depend on the properties of the Coulomb wave functions. To apply this theory to our case, the β-decay framework, the cross section is replaced by a decay probability, directly connected to the β-strength parameter, $g_{\lambda,X}$, which can be Fermi ($g_{\lambda,F}$) or Gamow-Teller ($g_{\lambda,GT}$). With these changes, the collision matrix element for a β-decay is described by:

$$M_{\lambda,X} = \frac{g_{\lambda,X}}{\sqrt{1 + \sum_c \gamma^2_{\lambda,c} \frac{\partial S_c}{\partial E}|_{E=E_\lambda}}} \tag{5.9}$$

where S_c is the shift function.

If there is only one resonance in the nucleus, the natural choice of the R-matrix parameter E_λ is the energy of the resonance. In the case where more than one resonance are present, the energy of the R-matrix, E_λ, only can take the energy value of one of the resonances. The reduced widths will depend on the boundary conditions due to the fact that the matrix is not diagonal. To solve this issue, one can find a set of R-matrix parameters for one of the resonances, resolve it and get the observables, and, then, modify the initial parameters to resolve the next resonance. This process is iterative and produces an invariant

collision matrix, so the branching ratio (or the cross section in the nuclear reactions framework) is kept constant.

To demonstrate the relation of the R-matrix parameters with the physical and measurable observables, the study is reduced to the single level approximation, proving that the results of this reduction coincide with the Breit-Wigner formula for a narrow resonance (demonstrated in [Hyl10]). This approximation will be valid for wider levels as long as the shift function is linear above the resonance. In this case, the widths, Γ^0_λ, are independent of the energy.

For levels close to the threshold of particle emission, the single level spectrum differs significantly from the Breit-Wigner form. This is due to the fast increase of the penetration function with energy, enhancing the high energy tails above the level leading to a second local maximum at higher energies, known as a ghost level.

The R-matrix theory includes an interference effect which cannot be taken into account within the Breit-Wigner approximation. The overlap of levels with same spin and parity can interfere constructively or destructively and this effect makes impossible to solve the nuclear structure as a sum of single levels. For narrow levels, the branching ratio and the *ft*-value are directly related and well defined. For broad levels, the *ft*-value will have an energy dependence correlated with the elements of the collision matrix or with the branching ratios. The *ft*-value will not be used when treating broad or resonant levels as the calculations through the collision matrix or the branching ratios do not converge. On one hand, if it is correlated with the matrix elements, then the *ft*-value is independent from the effects of the tails of the levels. On the other hand, if the *ft*-value is correlated with the branching ratios, the integral of a level depends on the other levels, producing a contradiction because it will imply that the matrix element is an overlap of the initial and final states.

To resolve an experimental spectrum with the R-matrix model, only the main levels that can be adjusted in the spectrum are included in the basis, reducing the problem to fit a few levels. This truncation forces to include a wide background level to the model, to compensate for the bias on the levels not included in the basis. Depending on the channel radius chosen, the parameters of the background level will be modified but these parameters have no influence on the remaining (physical) levels. For details about the dependence of the R-matrix model on the background level, see [RFHJ15].

5.4.2 The case of ^{8}B β-decay

In the β-decay of ^{8}B, there are only 4 excited (also the 0^+ ground state) states in the daughter nucleus, ^{8}Be, lying within the Q_{EC} window that can be fed by allowed transitions. The β-decay to the 2^+ 3 MeV state is purely Gamow-Teller and therefore in the analysis no Fermi part will be present in the treatment of this state. For the 2^+ doublet at 16.6 and 16.9 MeV, the treatment will be explained in detail in the following. Even though there is a 4^+ level in ^{8}Be lying at 11.4 MeV, this transition would be second forbidden and will not be included in the R-matrix analysis. Since the three levels populated are 2^+ states, the analysis of the spectrum is simplified to a single channel.

The two states that form the doublet at 16.6 and 16.9 MeV are treated following Barker's approach [Bar69]. Assuming the isospin mixing between the two states [Bar75], each level can be described as a linear combination of the T = 0 and T = 1 (analogue of the ^{8}Li and ^{8}B ground states) components:

$$|a\rangle = \alpha|T=0\rangle + \beta|T=1\rangle \tag{5.10}$$

$$|b\rangle = \beta|T=0\rangle - \alpha|T=1\rangle \tag{5.11}$$

where $|a>$ and $|b>$ are two isospin-mixed states that must comply $\alpha^2+\beta^2=1$. With this reasoning, the collision matrix elements for the two states for both Fermi and Gamow-Teller elements are described as:

$$M_{a,X} = \langle a|O_x|^8B\rangle \rightarrow \begin{cases} M_{a,F} = \sqrt{2}\beta \\ M_{a,GT} = \alpha M_{0,GT} + \beta M_{1,GT} \end{cases} \tag{5.12}$$

$$M_{b,X} = \langle b|O_x|^8B\rangle \rightarrow \begin{cases} M_{b,F} = -\sqrt{2}\alpha \\ M_{b,GT} = \beta M_{0,GT} - \alpha M_{1,GT} \end{cases} \tag{5.13}$$

where $M_{0,GT}$ and $M_{1,GT}$ are the Gamow-Teller matrix elements for isospin T=0 and T=1, respectively.

The channel radius parameter (r_0) chosen for this study has been fixed to 1.35 fm from previous works [Hyl10].

5.5 R-MATRIX ANALYSIS

5.5.1 ORM program

The ORM program has been developed by M. Munch, O.S. Kirsebom and J. Refsgaard from the AUSA-group with whom we work in a collaboration [MKR]. The code contains the mathematical description of the R-matrix to perform a fit to β-decay experimental data. A. Gad has contributed to the code to improve and adapt it to the ^{8}B case, related with the specific treatment of the β-decay. For more details about the contribution done by A. Gad see [Gad18].

The fitting process is done using the Minuit program developed at CERN and implemented in *ROOT*. This program is based on the minimization of a log-likelihood function. Each level included in the truncated R-matrix basis creates one fit parameter for each channel coupled to the energy of the level. The parameters obtained from the fit are, for each state, the B_F, the B_{GT}, the energy and the $\Gamma_{\alpha\alpha}$ parameter, which is the width of the level.

The ORM code includes a folding with the response function of the detector setup to fit the data. Such a response function must be calculated carefully because it is an essential part of the fit (see Sec. 4.3.4). In this work we have followed two different approaches to treat the response of the detector when fitting within R-Matrix: first, to include the response function in the fitting procedure (Sec. 5.5), and second, to do an unfolding process of the data and then do the fit with a response matrix equal to 1 (Sec. 6.3.2).

5.5.2 High-energy region

As it was stated before, the main goal is to obtain the β-decay transition probabilities in the decay of ^{8}B into ^{8}Be, in particular, the B_{GT} and B_F to the isospin doublet at 16.6 and 16.9 MeV excitation energy. As these two states are far enough from the main decay in energy, one of the options is to focus only on the high-energy part of the spectrum and fit these two states. This option has many advantages as one of the main issues of fitting the full spectrum is that the program is based on the χ^2 minimization and the main decay at 3 MeV state dominates the fit due to its huge statistics.

The region to fit is then reduced to the interval from 16 MeV to 18 MeV. In this approach, the states to be included in the fit are the 2^+ states at 3 MeV, 16.6 MeV and 16.9 MeV. The parameters fixed during the fit are the channel radius parameter, which has been set to 1.35 fm, and the B_F=0 of the 3 MeV state, as the transition to this state is purely Gamow-Teller.

The result obtained with these conditions is shown in Fig. 5.13. The upper panel of the figure shows the high-energy region of the ^{8}Be spectrum overlaid with the resulting contribution of each state and the global fit (see legend for details). The lower panel represents the residuals, calculated according to Eq. 5.14.

$$R = \frac{Experimental - Fit}{Experimental} \tag{5.14}$$

For this fit, the $\frac{\chi^2}{d.o.f} = 0.189$ indicating that the errors are overestimated for this region but, with the lower value of the χ^2 and a visual check of the fit we can conclude that this model fits perfectly the high-energy region of the experimental data. Notice that the individual contribution of each state can not be added to obtain the final fit due to the destructive interference between them.

5.5.3 Full spectrum fit

Even though our aim is to understand the nature of the 2^+ doublet, clearly the properties of the doublet will affect and be affected by the main decay and therefore the full spectrum has to be fitted. If the fit is done over the full range spectrum, the spectrum is not well reproduced. The upper panel of Fig. 5.14 shows the plot of the results of the analysis in the high-energy region (previous section) when the full spectrum is opened. With the parameters obtained in the fit of the high-energy region, the contribution of the 3 MeV level is one order of magnitude larger than the experimental data.

If the three levels parameters are set free to obtain the best fit, the R-matrix analysis cannot resolve the full spectrum as shown in the lower panel of Fig. 5.14. Although the fit visually is much better than with the parameters of the high-energy fit, the discrepancies between the experimental data and the fit are still too large (Fig. 5.14 lower panel), as indicated by a $\chi^2/d.o.f. = 4348$. These discrepancies occur mainly below 4 MeV and in the region between 10 and 14 MeV. This is seen at first sight by looking at the spectrum, being the fit (red

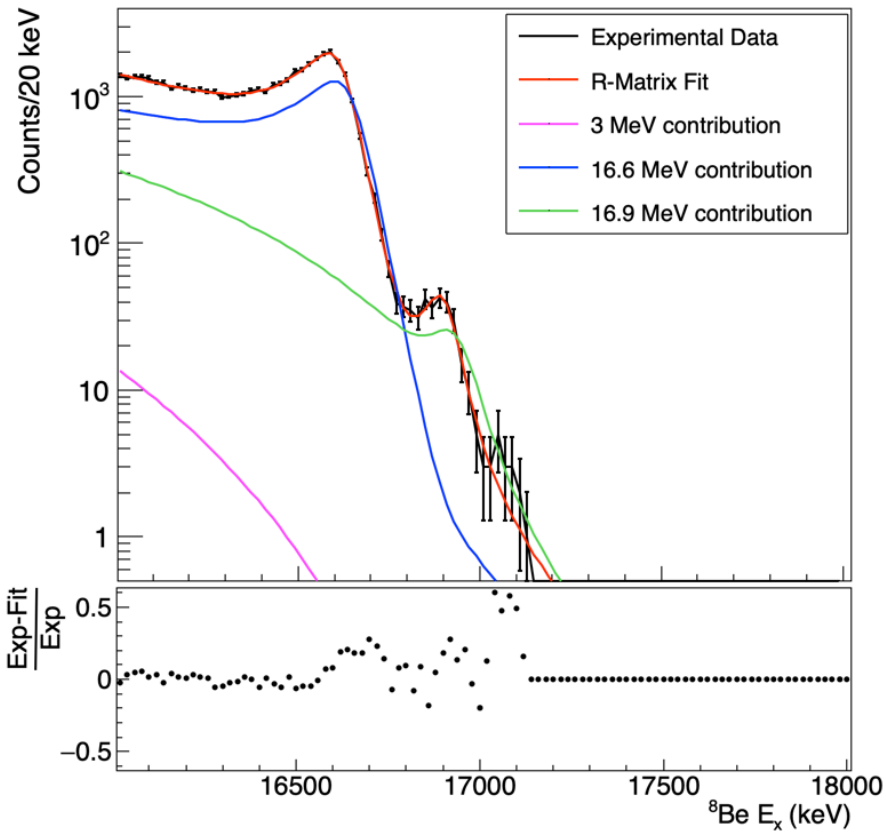

Figure 5.13: R-matrix fit of the ^{8}B decay spectrum in the interesting region for the doublet: from 16 MeV to 18 MeV. The upper panel shows the experimental data (black) and the result of the R-matrix fit (red). The lower panel shows the residuals. The x-axis represents the excitation energy of ^{8}Be. (As a reminder, the excitation spectrum has subtracted the separation energy of the α and corrected the recoil energy).

line) above the experimental data (black line) for energies less than 4 MeV and below in the region between 10 and 14 MeV.

In order to obtain a better fit of the full spectrum, a background level has to be added. The background level is to take into account that the basis used to solve the R-matrix analysis is truncated, not including levels above our experimental data, as explained in Sec. 5.4.1. The background level has no direct physical meaning but can produce constructive or destructive interference with the other levels. In the studied case, the background level is situated far beyond the fit range of the spectrum but only contributes constructively to the fit below 15.5 MeV.

Moreover, when fitting the full spectrum, a problem due to the several orders of magnitude difference in statistics between the feeding to the 3 MeV level and the doublet at 16 MeV appears. The fitting process is based on the χ^2 minimization and, due to the fact that the main contribution to the χ^2 comes from the main decay (high statistics, small errors), the fitting code focuses on the main decay and disregards the high-energy region (low statistics, large errors). To solve this, we have biased the fit modifying artificially these errors: multiplying the statistical errors bin by bin below 7 MeV by 100, between 7 MeV and 15.5 MeV by 10 and dividing by 10 above 15.5 MeV. The errors associated to the data are thus modified to fix the 2^+ doublet parameters and to enhance the importance of the high-energy region of the spectrum in the fitting process.

The fit-process is started by first varying the parameters related with the 2^+ doublet at 16 MeV with the errors modified, so that the influence of the background level and the 3 MeV should not have a strong importance on this region. Once the fit reproduces well the data in the high-energy region, we fix the parameters of the doublet and try to fit the other two levels, but now with the statistical errors.

The parameters of the 3 MeV level and the background level are set free with the exception of the B_F of both states as these are considered purely Gamow-Teller. As a starting point, the energy for the background level is placed at 20 MeV. Figure 5.15 shows the best fit obtained fitting the 4 levels. As can be seen, visually the fit is in good agreement with the experimental data and by looking into the residuals, the main discrepancies between the fit and the experimental data are from the low energy region of the spectrum, below 2 MeV. If all the

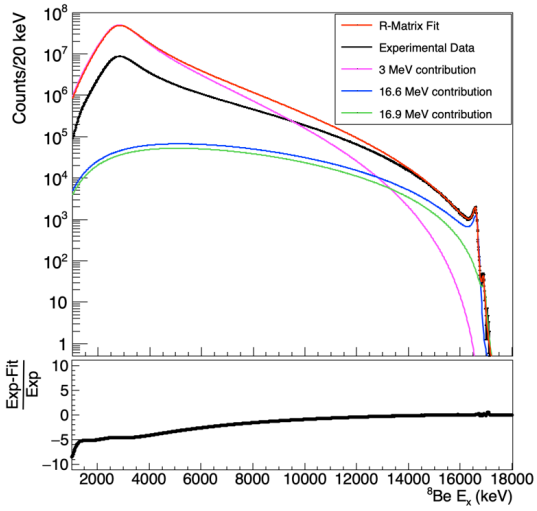

(a) 3 levels fixed as in the high-energy region fit

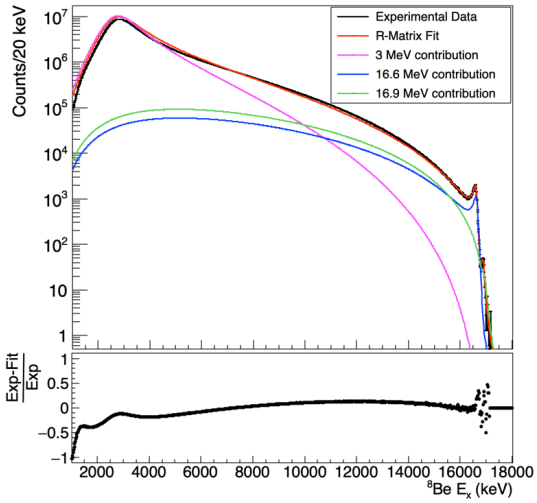

(b) 3 levels fitted to the full spectrum

Figure 5.14: In the upper panel, the plot of the R-matrix result of the high-energy region in the full spectrum region. In the lower panel, the best fit obtained with three levels fitting the full spectrum.

spectrum (from 1 MeV to 18 MeV) is used to determine the $\frac{\chi^2}{d.o.f}$, the result is $\frac{\chi^2}{d.o.f} = 34.01$. If the fitting range is reduced above the main decay, from 3 MeV to 18 MeV, $\frac{\chi^2}{d.o.f} = 9.2$. For the doublet region from 15 to 18 MeV, $\frac{\chi^2}{d.o.f} = 0.77$.

With this method, the doublet is well fitted. However, it can be seen from the individual contributions of each level that the 3 MeV and the background levels do not contribute to the fit of the two states of the doublet since, for example, the 3 MeV contribution has, at 16 MeV, an effect on the global fit of two orders of magnitude below the doublet contribution. For this reason, the final fit of the doublet is obtained by fixing the 3 MeV and the background levels to the results of the general fit and reducing the fit region from 15 to 18 MeV, setting free the four parameters of the two states of the doublet. By doing this iterative process, the χ^2/dof at the end of the spectrum and therefore in the region where we are interested is reduced by a factor of ∼2, being $\frac{\chi^2}{d.o.f} = 0.39$ for the region from 15 MeV to 18 MeV. Fig. 5.16 shows the fit of the 2^+ doublet after the new fit (lower panel).

One could wonder if the new fit to the doublet will affect the rest of the spectrum. The contribution of the doublet in the energy region of 1 to 6 MeV is 3 orders of magnitude below the contribution of the 3 MeV state, thus it will not affect the fit in this region. The tricky region is between 6 and 12 MeV. In this region, the contributions of each level is in the same order of magnitude. When fixing the doublet and letting the 3 MeV state free, the results in this region (6 to 12 MeV) are worse than when fitting the full spectrum, being $\frac{\chi^2}{d.o.f} = 62.22$ for the region from 1 to 18 MeV. However, it is known that the R-Matrix analysis can not reproduce this region, being one of the reasons of including a background level (see discussion in [RFHJ15]). On the upper panel of Fig. 5.16 one can see the full spectrum.

Visually there is no difference between the two fits. However, it is in the χ^2 where the differences are noticeable. Summarizing, on one hand, the fit that focuses on the full spectrum (1 to 18 MeV), from now on referred to as **holistic**, has a better $\chi^2/d.o.f$ for the full spectrum than the fit focused on fitting the doublet (15 to 18 MeV). On the other hand, the fit to the 2^+ doublet-region is improved when the interval of fitting is reduced. The results of these two fits will be discussed and used to calculate the isospin mixing of the states of the 2^+ doublet. The final parameters of these fits with their uncertainties will be

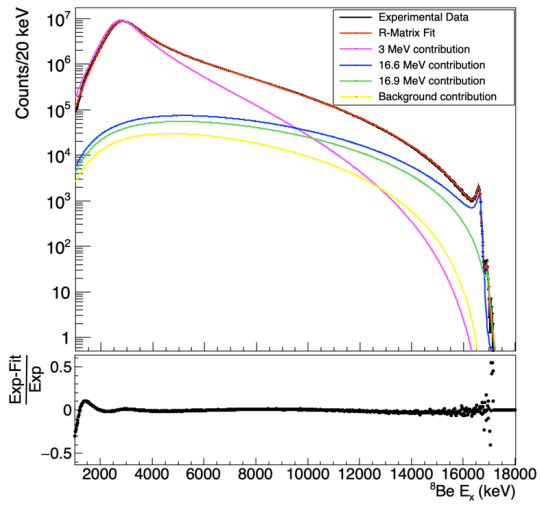

(a) Full spectrum

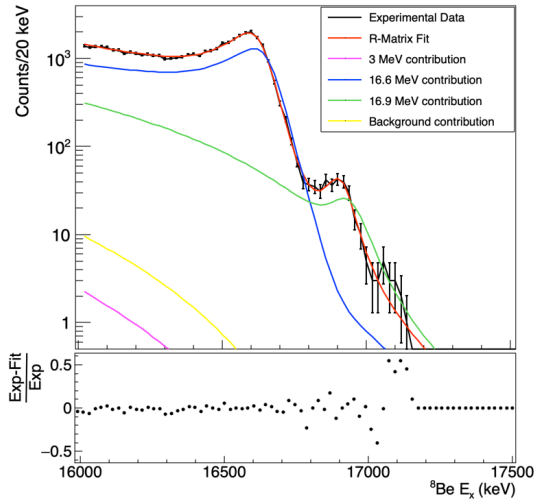

(b) Zoom at the doublet region

Figure 5.15: R-matrix fit of ^{8}B-decay full spectrum with 4 levels with the focus set on fitting the full spectrum. In the upper panel, the full range view. In the lower panel, a zoom on the doublet region. The main panels show the experimental data (black) and the result of the R-matrix fit (red). The contribution of each level is represented by different colors (see legend).

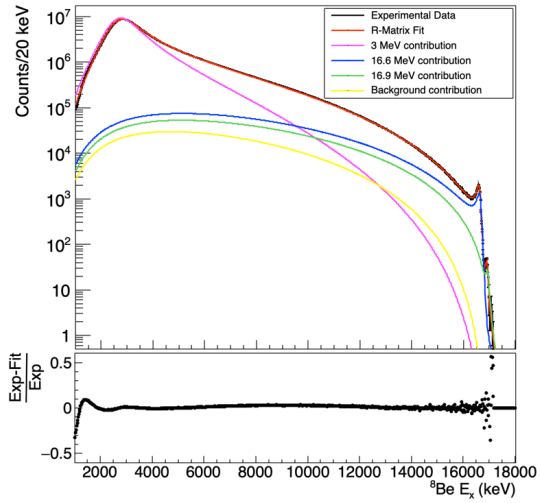

(a) Full spectrum

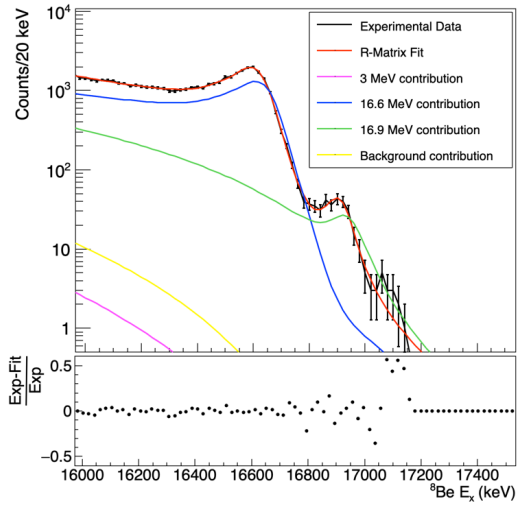

(b) Zoom at the doublet region

Figure 5.16: R-matrix fit of ^{8}B-decay full spectrum with 4 levels with the focus set on fitting the 2^+ doublet region. In the upper panel, the full range view. In the lower panel, a zoom on the doublet region. The main panels show the experimental data (black) and the result of the R-matrix fit (red). The contribution of each level is represented by different colors (see legend).

shown and discussed in comparison with the published values in [Tea04] in Sec. 5.5.6.

5.5.4 Study of the sensitivity of the parameters

To check the sensitivity of the fit to the different parameters, a study of the variation of the χ^2 value over small variations of each parameter around the fit values can provide information about the goodness of the fit and the errors associated with each parameter. This study is done over the parameters, differentiating when the fit has been done following a holistic approach (fit the full spectrum) or when it has been focused on improving the results of the doublet (fit of the high-energy region). The variations are done individually for each parameter, fixing the other parameters to the result of the R-matrix analysis, and calculating the $\chi^2/d.o.f.$ between the fit result of the R-matrix analysis and the experimental data. What is expected is that the $\chi^2/d.o.f$ found with the R-Matrix analysis is the minimum of a parabolic curve for each parameter. This study has improved the solution as one parameter, the B_{GT} of the 16.6 MeV state, was fitted to a local minimum, worsening the fit obtained with the R-matrix analysis.

For the study of the parameters obtained in the holistic fit, the 3 MeV level has been studied with the data with the statistical errors correctly propagated, however, the parameters of the doublet have been studied with the statistical errors biased as it was this set of data the one used to fix the parameters. Despite this change in studying the doublet, the χ^2 will still be dominated by the 16.6 MeV state as it has 2 orders of magnitude more statistics than the 16.9 MeV level. In the case of the doublet, the absolute value of the $\chi^2/dof = 5.35$ is a not realistic result as it has been calculated with the errors biased, however its variations will be studied in order to obtain a more realistic error estimation. For the 3 MeV level, $\chi^2/dof = 34.01$ as it has been calculated over the full energy region of 1 to 18 MeV.

For the study of the sensitivity of the parameters when fitting only the doublet, from 15 to 18 MeV, the data have the errors correctly propagated and the reference value of the $\chi^2/dof = 0.39$.

The results of the sensitivity study for the three physical levels included in the analysis are shown in the next figures. The first three figures are for the

holistic fit and the next two for the doublet study. Fig. 5.17 shows variation of the three parameters for the 3 MeV level and Fig. 5.18 and 5.19 the same for the four parameters of the doublet respectively. Fig. 5.20 and 5.21 are for the parameters obtained when fitting the doublet. In the figures, the orange point (triangle) is the resulting value of the fit and the dashed line the parabolic function that fits the data.

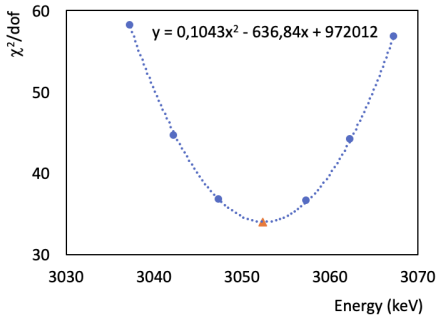

(a) Energy (keV)

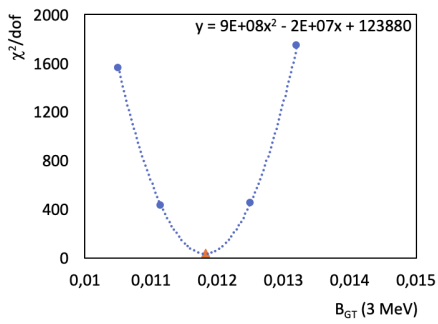

(b) B_{GT}

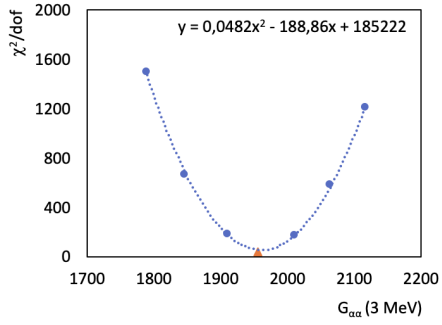

(c) $\Gamma_{\alpha\alpha}$ (keV)

Figure 5.17: Sensitivity of the χ^2 parameter of the three parameters of the 3 MeV level in the holistic fit. In orange (triangle) the reference value of the fit and the dashed line is the parabolic curve that fits the data, with the resulting equation.

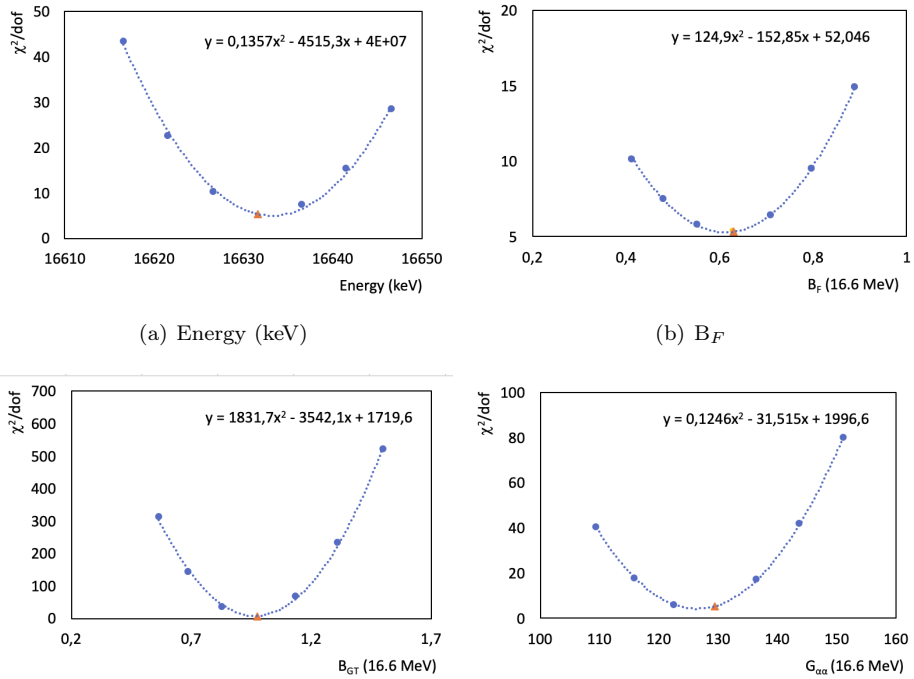

(a) Energy (keV)

(b) B_F

(c) B_{GT}

(d) $\Gamma_{\alpha\alpha}$ (keV)

Figure 5.18: Sensitivity of the χ^2 parameter of the three parameters of the 16.6 MeV level in the holistic fit. In orange (triangle) the reference value of the fit and the dashed line is the parabolic curve that fits the data, with the resulting equation.

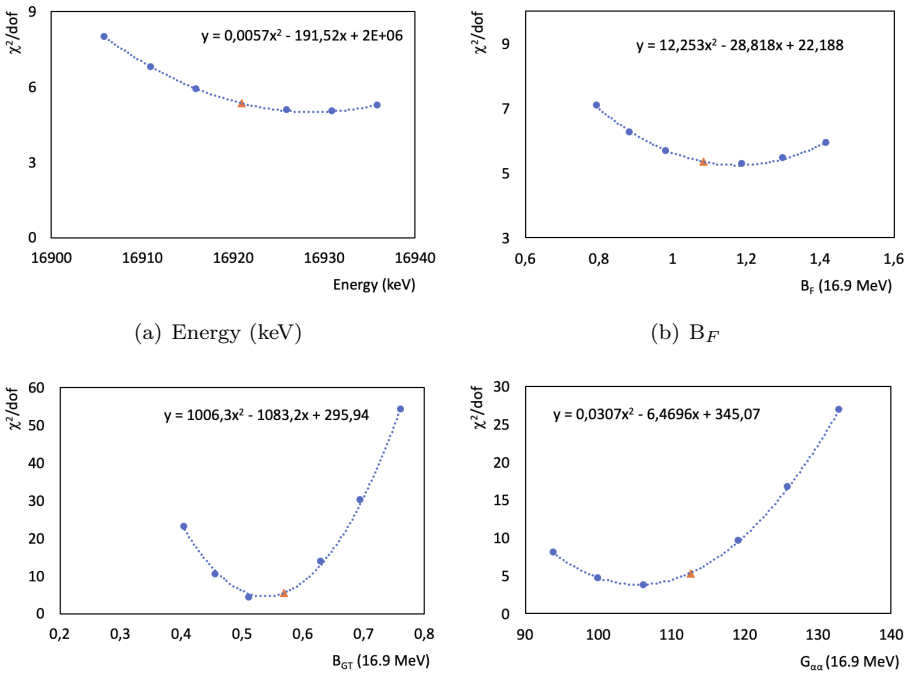

(a) Energy (keV)

(b) B_F

(c) B_{GT}

(d) $\Gamma_{\alpha\alpha}$ (keV)

Figure 5.19: Sensitivity of the χ^2 parameter of the three parameters of the 16.9 MeV level in the holistic fit. In orange (triangle) the reference value of the fit and the dashed line is the parabolic curve that fits the data, with the resulting equation.

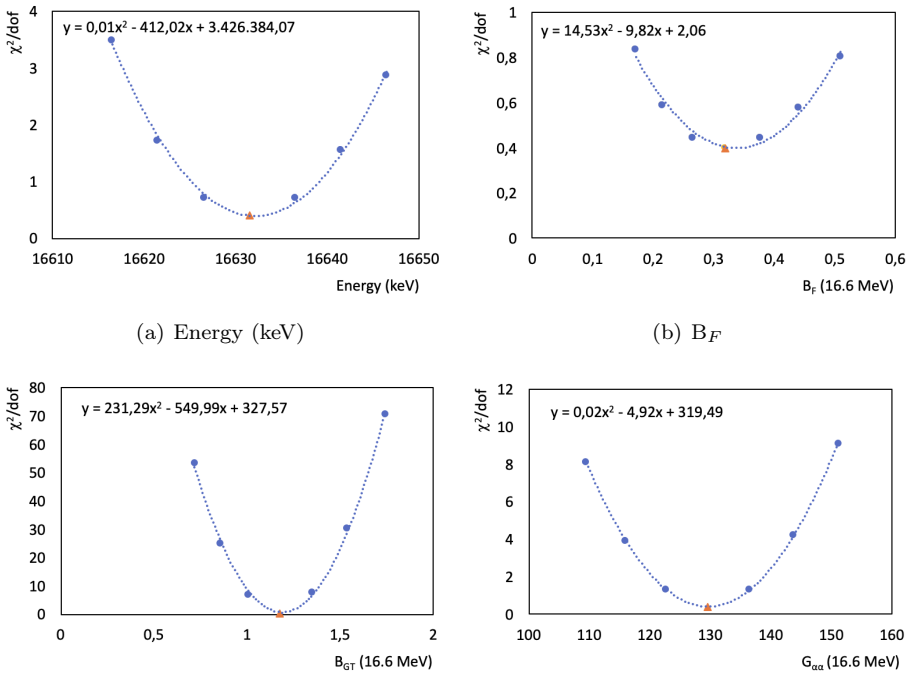

(a) Energy (keV)

(b) B_F

(c) B_{GT}

(d) $\Gamma_{\alpha\alpha}$ (keV)

Figure 5.20: Sensitivity of the χ^2 parameter of the three parameters of the 16.6 MeV level when fitting the doublet. In orange (triangle) the reference value of the fit and the dashed line is the parabolic curve that fits the data, with the resulting equation.

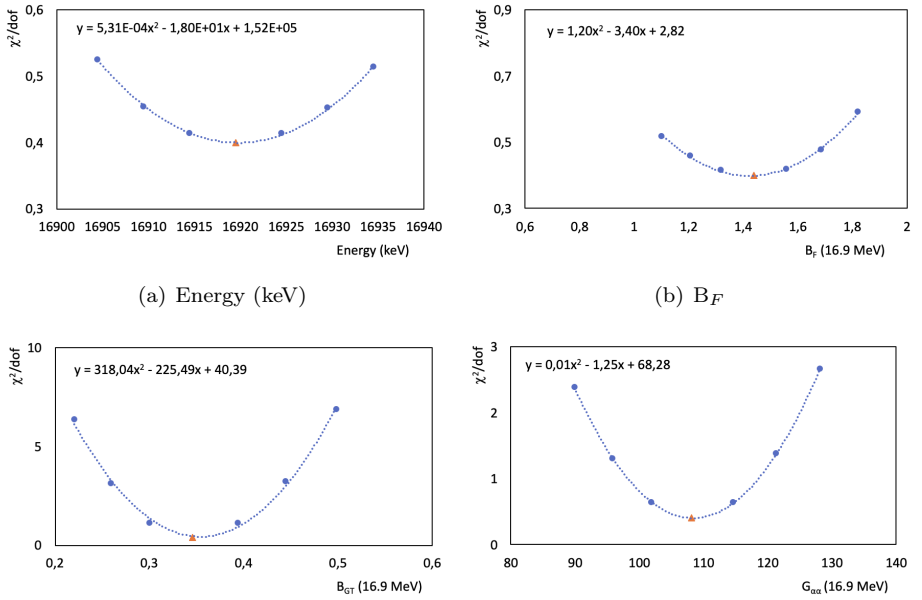

(a) Energy (keV)

(b) B_F

(c) B_{GT}

(d) $\Gamma_{\alpha\alpha}$ (keV)

Figure 5.21: Sensitivity of the χ^2 parameter of the three parameters of the 16.9 MeV level when fitting the doublet. In orange (triangle) the reference value of the fit and the dashed line is the parabolic curve that fits the data, with the resulting equation.

For the holistic fit (Fig. 5.17, 5.18 and 5.19), the study demonstrates that the program has determined the parameters that minimise the χ^2 for the 3 MeV and 16.6 MeV states. For the 16.9 MeV, it could seem that the parameters are not well defined, however a strong correlation is observed between the parameters of the levels that prevents to fit the experimental data with the minima found by this study of one single parameter variation.

When focusing on the doublet (Fig. 5.20 and 5.21), the results are similar to the holistic ones and the fit has minimized the χ^2 for all the parameters.

The sensitivity of the background level should be studied, for instance, fixing the parameters of the three physical levels to the published values and comparing the results of the background parameters with the ones obtained with the fit presented in this work.

5.5.5 Error handling

Following the prescription of chapter 39 of the *Review of Particle Physics* of the Particle Data Group [PeaPDG16], one can estimate the errors of a fit from the χ^2 value. It is said that, for example, in the case of fitting one parameter, in order to obtain a 95.5% confidence interval (2σ), one should add 4 units to the χ^2 value of the fit. With this method, the errors obtained become insignificantly small due to the large number of degrees of freedom in the fit. Moreover, this method will only give us the uncertainty of one parameter, being a long and hard method to obtain the errors associated to each parameter involved in the fit. For this reason, this method will not be used.

From each parabolic curve, the errors of each parameter can be calculated assuming a variation of the $\chi^2/d.o.f$ of 10%, which would be a very conservative error estimate. This method allows to calculate systematically the errors of each parameter independently of the χ^2 obtained by the fit, which is really useful for the case of the doublet parameters in the holistic fit as the χ^2 has no physical or statistical meaning since it was obtained scaling the errors associated to the data. Moreover, with this conservative errors we are including the large χ^2 obtained in the fit and the systematic errors of the method. However, this errors do not include the correlations between the different parameters.

Apart from the χ^2 calculation, the ORM program also provides the errors

Table 5.2: Correlation matrix between the parameters of the 2^+ doublet when fitting the region between 15 and 18 MeV (2^+ doublet fit). Parameters of 16.6 MeV level are labelled as 1 and the level at 16.9 MeV as 2.

	$\mathbf{E}_1$	$\mathbf{B}_{F,1}$	$\mathbf{B}_{GT,1}$	$\Gamma_{\alpha\alpha,1}$	$\mathbf{E}_2$	$\mathbf{B}_{F,2}$	$\mathbf{B}_{GT,2}$	$\Gamma_{\alpha\alpha,2}$
$\mathbf{E}_1$	1	-0.342	-0.311	0.745	-0.469	-0.384	0.404	-0.815
$\mathbf{B}_{F,1}$		1	0.997	-0.665	0.243	0.965	-0.987	0.511
$\mathbf{B}_{GT,1}$			1	-0.636	0.258	0.967	-0.989	0.502
$\Gamma_{\alpha\alpha,1}$				1	-0.257	-0.619	0.661	-0.728
$\mathbf{E}_2$					1	0.338	-0.344	0.629
$\mathbf{B}_{F,2}$						1	-0.969	0.520
$\mathbf{B}_{GT,2}$							1	-0.612
$\Gamma_{\alpha\alpha,2}$								1

associated to the data. The errors of the ORM program are from Minuit calculation and include the correlations between the different parameters. The correlations are larger between the B_F and B_{GT} of the doublet, also between the two states. An example of the correlations is found in Tab. 5.2, where the correlation factors when fitting the 2^+ doublet in the region above 15 MeV are summarized.

The errors given by Minuit are strongly affected also by the statistics and this leads to the errors associated to the energy to be underestimated. For example, the resolution of the setup and the binning used are not included. An example of this is the parameters of the 3 MeV level: the energy has a value of 3052 keV and the error provide by the ORM program is 0.24 keV. Considering the width of the peak, this small error is unrealistic. Tab. 5.3 compares the errors obtained with a 10% of variation in the χ^2/dof value and the errors given by Minuit.

To define the errors of the parameters of our fit, we will consider a merge between the errors: in case of the energies, since they do not show correlation with the other parameters, the errors will be defined as the one obtained varying 10% the χ^2/dof. For the other parameters, the errors will be defined as the Minuit ones except for the 3 MeV level parameters, which will be assumed to be conservative errors due to the strong correlation between the $\Gamma_{\alpha\alpha}$ and the B_{GT}.

Table 5.3: Comparison of the relative errors obtained with a 10% of variation in the χ^2/dof value and the errors given by Minuit for the two final fits: the holistic and the 2^+ doublet fits. The errors are expressed as the percentage over the value given by the fit.

Level	**Parameter**	**Holistic Fit**		**2^+ doublet Fit**	
		10% χ^2/dof	**Minuit**	**10% χ^2/dof**	**Minuit**
3 MeV	**E**	1.21%	0.01%		
	B_{GT}	0.48%	0.06%		
	$\Gamma_{\alpha\alpha}$	0.77%	0.02%		
16.6 MeV	**E**	0.33%	0.0015%	0.42%	0.02%
	B_F	13.68%	38.17%	50.32%	254.76%
	B_{GT}	3.07%	14.33%	2.68%	29.81%
	$\Gamma_{\alpha\alpha}$	5.17%	0.22%	1.33%	2.78%
16.9 MeV	**E**	0.12%	0.0045%	0.05%	0.04%
	B_F	29.55%	22.16%	13.96%	54.95%
	B_{GT}	12.11%	24.57%	4.53%	141.83%
	$\Gamma_{\alpha\alpha}$	13.33%	0.95%	2.48%	12.02%

An extra comment about the errors is that the fit focused in the doublet region from 16 to 18 MeV presents very large errors, for example for the $B_{F,16.6}$. This is a clear indication of the strong correlations with the other decay parameters. The best way to reduce those errors is including constrains on the fit to decrease the number of degrees of freedom. In our case, the logic constrain is to fix the sum of the Fermi strength to 2. However, the fit with this constrain does not converge to a reasonable result. In Sec. 6.3.2 we will see how this constrain helps a lot in the case of the unfolded data.

5.5.6 Comparison of the parameters between the holistic fit and the doublet fit

In Tab. 5.4 the results of this work are summarized and compared with the values of [Tea04]. The holistic fit is the one that best fits the full spectrum. The fit of the high-energy region is focused on obtaining the best results for the 2^+ doublet, being the initial parameters the ones of the holistic and being the

3 MeV and the background levels fixed to the holistic results.

As far as the excitation energy is concerned, the position of the three well-known states is well determined within the errors. In the adopted values from [Tea04] the width of the three physical levels are smaller than ours. Related with the intensities, both holistic and 2^+ doublet fits are in good agreement within the errors with the exception of the B_{GT} of the 16.6 MeV level. In this case, an underestimation on the uncertainty of the parameter can be the problem. The error of this parameter provided by the ORM program is one order of magnitude higher than the one estimated with the 10% variation of the χ^2.

The discussion of the results presented here is found in Sec. 8.2.

Table 5.4: Comparison of the different parameters obtained with the different approaches explained in the text. The adopted values are the values published in [Tea04]. The second column refers to the holistic fit (above 1 MeV). The third column shows the parameters when the doublet is optimized, being the initial point the holistic fit results.

Parameters		**Adopted values**	**Holistic Fit**	**2^+ Doublet Fit**
	r_0 (fm)	1.35	1.35	1.35
2_0^+	**E (keV)**	3030(10)	3052(37)	
	B_F		0	
	B_{GT}		0.011813(56)	
	$\Gamma_{\alpha\alpha}$(keV)	1513(15)	1957(15)	
2_1^+	**E (keV)**	16626(3)	16632(54)	16632(70)
	B_F		0.63(24)	0.32(81)
	B_{GT}		0.98(14)	1.17(35)
	$\Gamma_{\alpha\alpha}$(keV)	108.1(5)	129.47(28)	129.5(36)
2_2^+	**E (keV)**	16922	16921(20)	16919.5(90)
	B_F		1.08(24)	1.44(79)
	B_{GT}		0.57(14)	0.35(49)
	$\Gamma_{\alpha\alpha}$(keV)	74.0(4)	112.5(11)	108(13)
2_{Bkg}^+	**E (keV)**		21205	
	B_F		0	
	B_{GT}		1.3438	
	$\Gamma_{\alpha\alpha}$(keV)		119.11	

Deconvolution of the α spectrum

6

6.1 DECONVOLUTION OF A SPECTRUM

The deconvolution of a spectrum is an analysis technique used to extract physical information from experimental data affected by the non-perfect response of the detection device. It is used in many domains, for instance in gamma-ray spectrometry experiments [TCO07] and has the advantage of including the experimental features as the response of a detector to a certain energy deposited or to a certain particle.

Over the years, different methods of spectral deconvolution have been developed. Some of the algorithms to be mentioned are Expectation Maximization, Maximum Entropy and Linear Regularisation, see Ref. [TCO07] and references therein.

With charged particles, the deconvolution method has not been standardised yet as the interaction of the particles with the detector system is more complicated than for the case of gamma rays. As we have obtained a good characterisation and response matrix of the setup used in the IS633 experiment (Sec. 4.3.4), a door is opened to apply these methods to the α-spectrum.

6.1.1 The Richardson-Lucy algorithm

In 1972, W.H. Richardson reported the first results of applying probability methods to restoration of noisy degraded images [Ric72]. Later, in 1974, L.B. Lucy proposed a solution for a fundamental problem in statistical astronomy that consists in the estimation of the frequency distribution of a quantity, when the available measures are finite, from an infinite population [Luc74]. Both works proposed an iterative method based on Bayes' theorem.

This method became popular in particle physics after it was promoted by D'Agostini labelled as "Bayesian unfolding" [D'A95]. Nowadays it is usually known as the **M**aximum **L**ikelihood **E**xpectation **M**aximization (MLEM) in imaging reconstruction, since it was generalized by Dempster in 1977 [DLR77].

The Richardson-Lucy algorithm is extremely simple and excellently performing and it efficiently suppresses artificial high-frequency contributions, allowing to introduce known features of the true distribution [Zec13]. As our aim is to apply this method to a experimental histogram of data, the discussion and nomenclature of [Zec13] will be followed.

An event sample is defined by the variables x_1,...,x_n being the input sample a statistical distribution $f(x)$. When it is measured in a detector, the observed sample x'_1,...,x'_m is distorted due to imperfection such as the dead layers or the finite resolution of the detector, and reduced due to acceptance losses. This is the clear indicator that a regularization is needed to correlate properly the variable sample with the observed sample.

To start explaining the method, three histograms are defined:

The *true* histogram with content θ_j, with j=1,..,N. We aim to estimate this histogram from the observed (distorted) experimental data.

The *observed* (experimental) histogram contains the observed (distorted) sample with d_i events with i=1,...,M. This observed histogram is the convolution of the true one with the response function of the detector. Since we deal with discrete quantities, the two histograms are related by the linear problem to solve:

$$d_i = \sum_{j=1}^{N} A_{ij}\theta_j \tag{6.1}$$

being A_{ij} the response matrix defined as the probability to observe an event in bin i in the observed histogram that belongs to the true bin j of the true histogram.

The *unfolded* histogram with bin content $\hat{\theta}_j$, is the solution of the algorithm at each iteration.

In the Richardson-Lucy method, the corresponding matrix relation can be solved iteratively to estimate $\hat{\theta}$. Starting with a preliminary guess $\hat{\theta}^0$ (in our case, the unit) then the corresponding prediction for the observed distribution, referred to as *recalculated* histogram, at the 0 iteration t^0, is compared to the observed histogram, d, and, ideally, the ratio d/t^0 for each bin must be equal to 1. To improve the agreement, all true components are scaled proportional to their contribution $A_{ij}\hat{\theta_j}^0$ to t_i^0. The prediction t^k of the k iteration in a folding step from the true vector $\hat{\theta}^k$, the aforementioned recalculated histogram, is described mathematically as follows:

$$t_i^k = \sum_{j=1}^{N} A_{ij}\hat{\theta_j}^k \tag{6.2}$$

In the unfolding step, instead of scaling $A_{ij}\hat{\theta_j}^0$ to t_i^0 it is scaled to the ratio d/t^0 and added up into the bin j of the true distribution from which was originated

$$\hat{\theta_j}^{k+1} = \frac{\sum_{i=1}^{M} A_{ij}\hat{\theta_j}^k \frac{d_i}{t_i^k}}{\alpha_j} \tag{6.3}$$

where α is the acceptance losses or efficiency of the detector.

The result of the iteration converges to the maximum likelihood solution [VSK85] for Poisson distributed bin entries. However, as the initial step is a smooth distribution, the artefacts of the unregularized maximum likelihood estimate (MLE) occur after a certain number of iterations. The regularization is done, then, interrupting the iteration sequence based on a p-value criterion that measures the compatibility of the regularized unfolding solution with the MLE.

The p-value is defined from the χ^2 distribution for N degrees of freedom (see details in [Zec13]). For the unfolding procedure, the p-value criterion depends, in general, of the number of events, the number of bins, the resolution of the detector and the shape of the true distribution. We will not use the p-value criterion in our unfolding study but we will study the behaviour of the χ^2 depending on these different aspects that affect the p-value criterion. With this study we will determine the optimal number of iterations.

In Fig. 6.1 one can see the flow-chart of the process. The orange arrows indicate the flow of the regularitzation. In green arrows, the comparison between the equivalent histograms: the observed and the recalculated and, when it is possible, the unfolded with the true. At the end of the unfolding procedure, the unfolded spectrum should be very similar to the true distribution, and the recalculated to the observed one. For our purposes we will define the χ^2 from the divergence between the observed histogram and the recalculated one (or between the true distribution and the unfolded one):

$$\chi^2 = \sum_{i=1}^{M} \frac{(d_i - t_i)^2}{t_i} \tag{6.4}$$

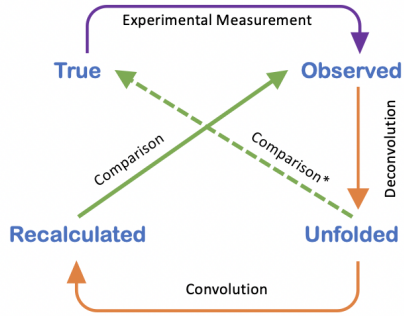

Figure 6.1: Flow-chart of the unfolding procedure. The orange arrows indicate the flow of the regularitzation. In green arrows, the comparison between the equivalent histograms.

6.1.2 Previous work on α-deconvolution

Since the 90's few studies have been focused on the deconvolution of an α-spectrum due to the difficulties involved in determining the response function of charged-particle detectors. The publications found are mainly focused on the deconvolution of plutonium spectra obtained with Silicon detectors [BTdB92] [VMC$^+$96]. In these works, the response function of the detectors were modelled with a gaussian function with left and right exponential tails. For both studies, the aim was to obtain a ratio between two Pu isotopes by reproducing the experimental fit, but not to obtain (following the notation of the previous section) the *unfolded histogram*. In [BTdB92], the deconvolution method used was based on using the χ^2 minimization using the Simplex method; in [VMC$^+$96], the work was performed using a commercially-available software developed for gamma spectrum analysis.

Lately, different approaches have been proposed for the α-spectra deconvolution. In [Aup04] it is proposed to measure actinides in environmental samples using a liquid scintillation detector (PERALS - **P**hoton **E**lectron **R**ejecting **A**lpha **L**iquid **S**cintillation). In this work, the peak shape of an isolated α was assumed to be gaussian and no information is provided about the deconvolution method. In this case, the results were the activity of each actinide but neither here an *unfolded histogram* is given.

Despite these works, there is still a lack of knowledge about the deconvolution of α-spectra. In [PPST12] it is noted the difficulty of measurement of α-spectra with semiconductor detectors: all the measurements must be done in vacuum due to the straggling in the air. However, in some applications such as continuous air monitoring, the α measurement is done in air and a deconvolution method for this type of measurements could improve the results of those experiments.

In this work, the measurements have been performed under vacuum to obtain the characterization of the DSSD as explained in Sec. 4.3.3 and once the geometric characteristics of the detectors are known, the response function can be obtained using GEANT4 simulations for different measurement conditions. For instance, we could follow the same approach in air than in vacuum for the aforementioned applications.

6.2 THE UNFOLDING CODE

We have implemented the unfolding code, based on the Richardson-Lucy algorithm, in C++ within the ROOT [roo] framework.

The program requires two inputs: the experimental data and the response function of the setup. The reading process of the input data can be done either in ROOT vectors or histograms for both objects. The output of the code is the unfolded histogram and the recalculated histogram, which is the convolution of the solution with the response function of the detector.

In the following, some checks of the program will be detailed. In these sections, the nomenclature is the one detailed in Sec. 6.1.1: the observed histogram is the data to unfold; the unfolded spectrum is the solution, the energy signal in absence of experimental effects; the recalculated histogram is the unfolded spectrum convoluted with the response matrix. For the cases where the solution is known, because it is the input of some simulated data, this input spectrum will be referred to as the true histogram.

6.2.1 Reproducibility of a simulated source

For the first test of the program, the observed histograms were simulated. The detector was simulated as a 9G-W1 DSSD facing the source at 38.9 mm. The response function was obtained simulating α-emission from 0 to 5 MeV in 20 keV steps with the geometry defined in Sec. 4.3.4. The response function used is the direct spectra corresponding to mono-energetic α.

Two α-spectra were analyzed for different purposes. The first, was a simulation of detecting non-overlapping α-particles of different energies and intensities. The second spectrum was produced with the same kind of simulation but now the detected α-particles might be overlapping due to the detector resolution. In both cases, the number of iterations to obtain the results shown is 1000.

No overlap spectrum

The upper panel of Fig. 6.2 shows the observed histogram filled in blue and the recalculated spectrum in dashed black line overlaying the input. The lower

panel are the residuals bin per bin, which have been calculated as

$$R = \frac{Observed - Recalculated}{Recalculated} \tag{6.5}$$

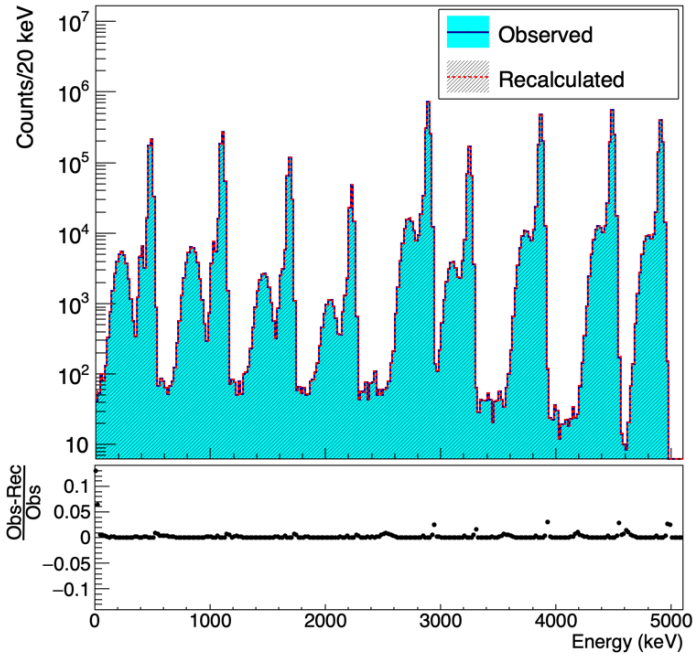

Figure 6.2: α-spectrum without overlap. In the upper panel, the observed histogram filled in blue and the recalculated spectrum in dashed black (almost indistinguishable). The lower panel are the residuals calculated as Eq. 6.5.

The solution of the algorithm and, therefore, the unfolded histogram is shown in Fig. 6.3. In the upper panel, the unfolded histogram in green that reproduces, convoluted with the response function, the input histogram (seen in the previous Fig. 6.2). The red crosses are the energies and intensities of each peak simulated, the true histogram. In the lower panel, the residuals calculated when there is information of the true histogram:

$$R = \frac{True - Unfolded}{True} \tag{6.6}$$

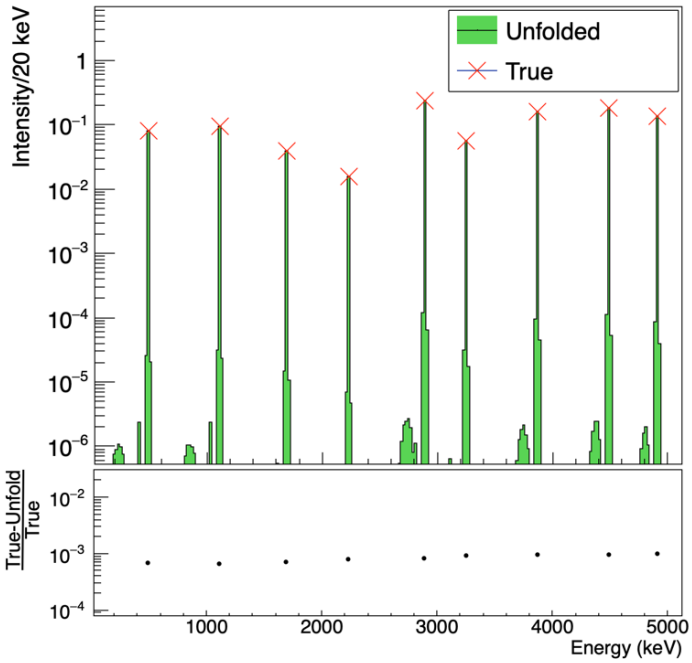

Figure 6.3: α-spectrum without overlap. In the upper panel, the unfolded histogram in green and the true histogram represented by red crosses. The lower panel shows the residuals when there is information of the true histogram calculated with Eq. 6.6.

From the results shown in the figures, we learn that the code is able to determine the relative intensity between each single-α emission with a $\chi^2 = 0.025$ for the recalculated vs observed histograms and $\chi^2 = 8.45 \times 10^{-8}$ for the true vs unfolded histogram which translates into relative errors smaller than 1% in the determination of the α intensities.

Overlap spectrum

For the second case, the results are shown in Fig. 6.4 and Fig. 6.5. In this case, the reproducibility of the histograms is determined by a $\chi^2 = 0.046$ for the recalculated vs observed histograms and $\chi^2 = 3.77 \times 10^{-7}$ for the true vs

unfolded histogram, implying relative errors smaller than 1% in the determination of the α intensities.

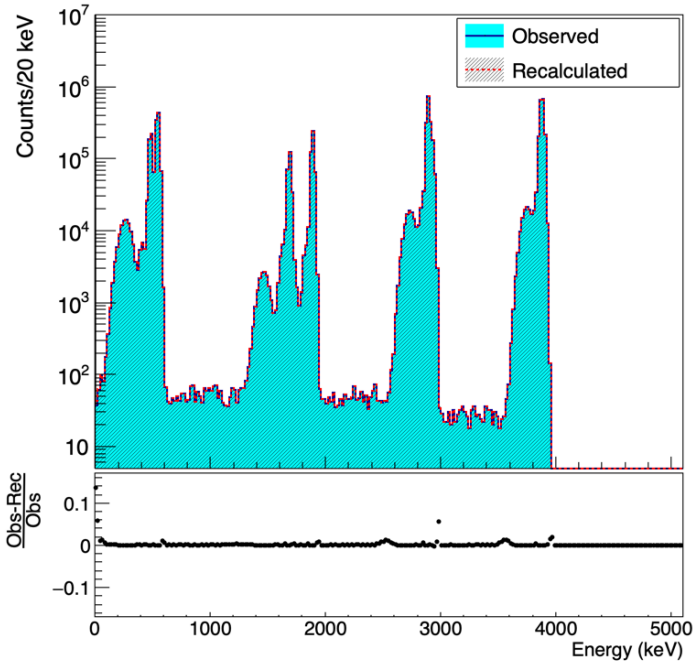

Figure 6.4: α-spectrum with overlap. In the upper panel, the observed histogram filled in blue and the recalculated spectrum in black. The lower panel are the residuals calculated as Eq. 6.5.

6.2.2 Reproducibility of an experimental source

The previous section shows really promising results but, of course, both spectra are purely simulations. In this section, the same study will be done but the input histogram is the calibration spectrum used in the IS633 experiment. For this check, the response function is the one detailed in Sec. 4.3.4 for single α detection.

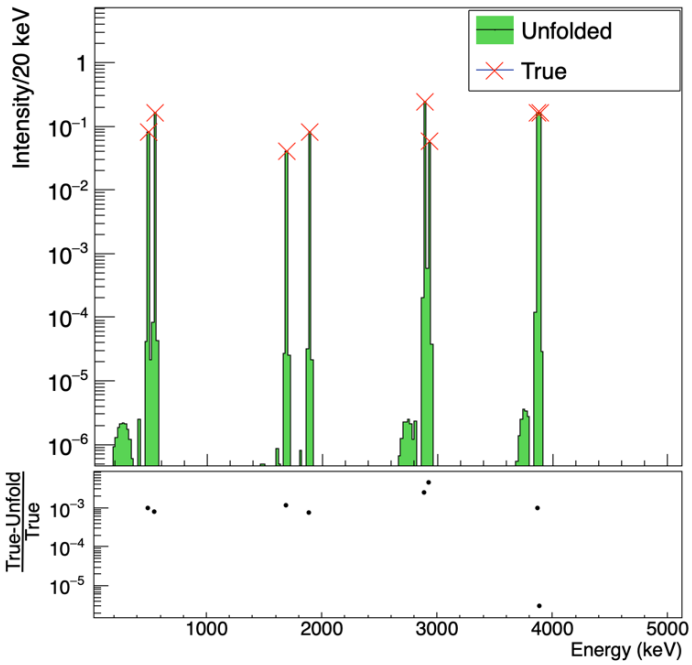

Figure 6.5: α-spectrum with overlap. In the upper panel, the unfolded histogram in green and the true histogram represented as red crosses. The lower panel are the residuals when there is information of the true histogram calculated as Eq. 6.6

The results shown in this study are for 10.000 iterations. Fig. 6.6 shows, in the upper panel, the observed histogram filled in blue and the recalculated spectrum in black line overlayed. The lower panel are the residuals bin per bin, which have been calculated using Eq. 6.5. In this case, the first channels of the spectrum have not been analysed to remove the threshold effects of the experimental setup.

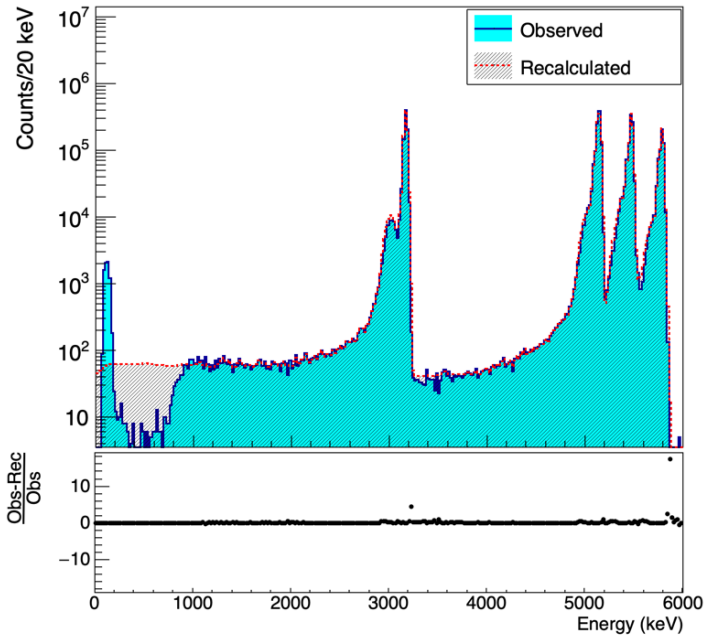

Figure 6.6: 4-α experimental spectrum. In the upper panel, the observed histogram filled in blue and the recalculated spectrum in black. The lower panel are the residuals calculated as Eq. 6.5. The discrepancies below 1 MeV are due to the electronic threshold, not included in the response function.

In this case, the true histogram is not clearly known: in Sec. 4.2.1, the data-sheet of the source specifies the activity of each nucleus of the calibration source the day of the measurement (see Tab. 4.2). However, to reproduce the experimental spectrum using GEANT4 simulations, the proportion of the nuclei

differs slightly. In Tab. 6.1 one can see the fraction of each nucleus detailed in the data-sheet and the results of the simulation. For the true histogram, the simulated proportion will be used.

Table 6.1: Isotope distribution in the 4-α source used in the IS633 experiment. The numbers from the data-sheet are calculated for the measurement day. The contributions from GEANT4 are the one that reproduces the experimental spectrum (see Sec. 4.3.3).

Isotope	**From Data-sheet**	**From GEANT4**
^{148}Gd	29%	23%
^{239}Pu	23%	30%
^{241}Am	27%	30%
^{244}Cm	21%	17%

The unfolded histogram overlayed with the true histogram are shown in the upper panel of Fig. 6.7. The green histogram is the unfolded histogram and the red crosses are the true histogram, where the different α-emissions of each isotope is distinguished. With this analysis, the different α-emissions of ^{239}Pu, ^{241}Am and ^{244}Cm are differentiate and well reproduced.

With a set of experimental data, the χ^2 values for the recalculated vs observed histograms is $\chi^2 = 2.63$ and for the true vs unfolded, $\chi^2 = 0.047$.

Of course, the discrepancies between the compared histograms are due to the lack of good reproduction of the low energetic tails of the peaks. Already in Sec. 4.3.4, the comparison of the simulated α-spectrum with the experimental one shows this discrepancy. However, the intensities recovered from the unfolded data are detailed in Tab. 6.2, where the first column is the isotope fraction obtained using GEANT4 simulations. Due to the 20 keV binning, the α-emission of 5156.6 and 5144.3 keV lie in the same channel. The solution of the unfolding is in very good agreement with the intensities simulated.

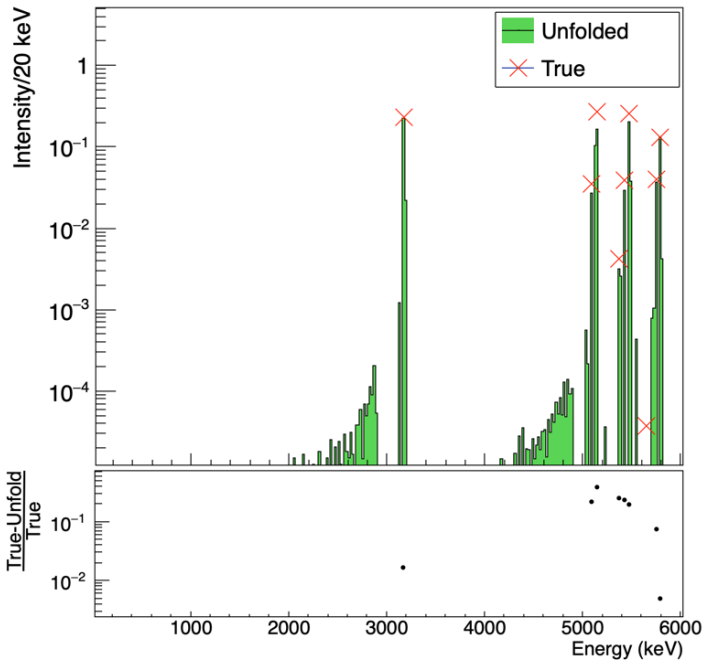

Figure 6.7: 4 α experimental spectrum. In the upper panel, the unfolded histogram in green and the true histogram represented by red crosses. The lower panel are the residuals when there is information of the true histogram calculated using Eq. 6.6

Table 6.2: Intensity of the 4-α emission of each isotope. First column are the intensities from the GEANT4 simulation (true distribution) and the second column are the results of the unfolded spectrum.

Isotope	**Energy(keV)**	**GEANT4 Intensity (%)**	**Unfolded Intensity (%)**
^{148}Gd	3182.8	23	25
^{239}Pu	5156.59 + 5144.3	27	27
	5105.5(8)	3	3
^{241}Am	5485.6	25	24
	5442.90	4	2
	5388	0.4	0.5
^{244}Cm	5804.82	13	14
	5762.70	4	3
	5664	0.004	0.1

6.2.3 Optimization of the number of iterations

The previous checks have demonstrated the reproducibility of experimental data with an extremely large number of iterations. One can think that the larger the number of iterations the better the results of the unfolding. However this is not true: it arrives an step where the algorithm tries to reproduce the statistical fluctuations, producing distortions in the unfolded histogram. In Sec. 6.1.1 p-value criterion has been presented and depends on the statistics, the number of bins, the resolution of the spectrum and the shape of the true histogram. In the following, the statistics criterion and the shape of the spectrum will be studied as a function of the regularization parameter that, for this algorithm, is the number of iterations.

Statistics criterion

We will simulate three spectra, emulating the decay of ^{8}B, with different statistics: in the first, 5×10^5 (10%) α-simulated events are analyzed. In the second, 1×10^6 (20%) and in the third, 5×10^6 (100%). The response function used is the same than in Sec. 6.2.1.

We will study the behaviour of the χ^2 as a function of the number of iterations. One might expected that the χ^2 improves with the number of iterations indefinitely or that it presents a certain minimum and ,after the minimum, the algorithm tries to reproduce the statistical fluctuations of the observed histogram distorting the unfolded spectrum increasing the value of the χ^2.

The comparison of the χ^2 for the three different analysis is shown in Fig. 6.8. Both panels show the χ^2 value obtained removing the first channels (starting at 100 keV) to reduce the uncertainty of the first channels due to artificial effects. The upper panel is the comparison between the recalculated and observed histograms and the lower panel between the true and unfolded histograms as a function of the number of iterations.

As predicted, a minimum in the χ^2 value between the true and the unfolded histogram is found. Depending on the amount of statistics, the minimum is found at the fourth iteration, for 10% of statistics, and in the fifth for the two other sets of data. In this case, also a minimum on the χ^2 value is found between the observed and the recalculated histogram. For the 10% of statistics, it is found at the 23^{rd} iteration, for the 20%, at the 16^{th} and for the 100% of statistics, at the 3^{rd} iteration.

In Fig. 6.9 one can see the comparison between the observed and recalculated histograms at different iteration numbers. In the upper panel the results for the 5^{th} iteration is shown, being the left panel the observed versus recalculated histograms and the right panel the true versus unfolded histograms. The lower panel shows the results for the 16^{th} iteration. The analysis is for the 1×10^6 statistics (20%) spectrum. The first channels (below 100 keV) are not reproduced as have been excluded of the unfolding process.

The difference between the unfolded histogram with 5 and 16 iterations is that for the second, the solution presents fluctuations at energies above 4000 keV that are not physical, to reproduce the statistical fluctuations of the observed histogram. Moreover, the peak-shape around 4700 keV losses the physical shape of a peak. This is an undesired effect so the number of iteration must be controlled to not over-fit. The results shown in Fig. 6.8 and 6.9 are crucial because they tell us that, for our experimental data, the optimum solution will be found after 5 iterations and it is important that we stop at this stage, as we will do in the next section, to avoid the appearance of distortions in the solution.

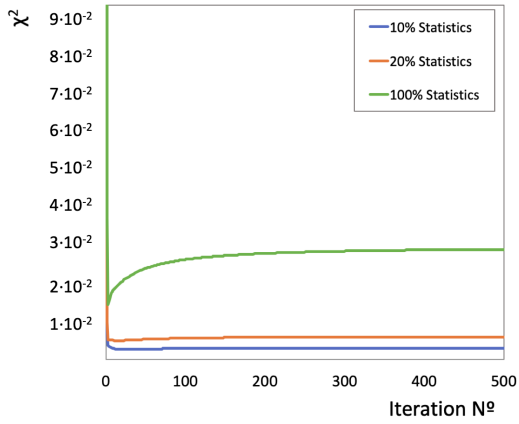

(a) Observed versus Recalculated

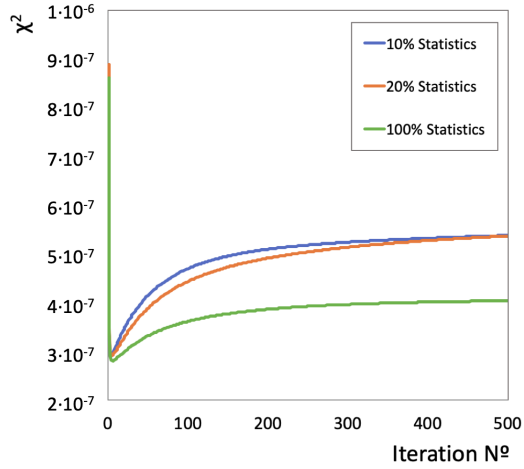

(b) Unfolded versus True

Figure 6.8: Study of the χ^2 for three spectra with different statistics as a function of the number of iterations. The spectrum with all the statistics was a simulation of 5×10^6 events.

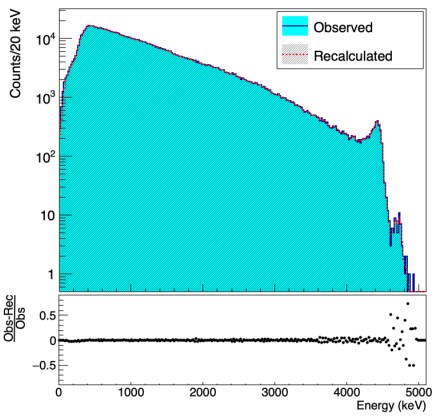

(a) 5^{th} iteration - Observed vs Recalculated

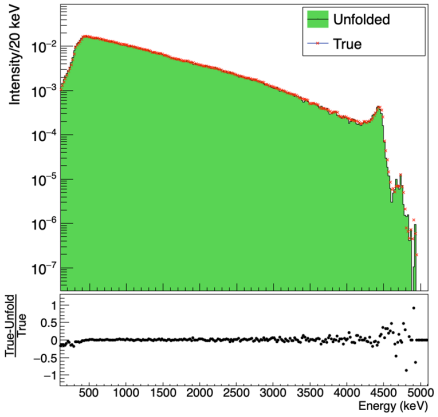

(b) 5^{th} iteration - True vs Unfolded

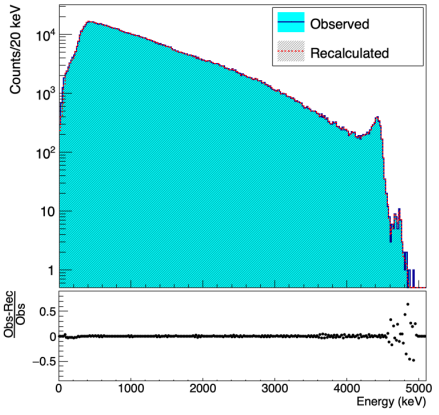

(c) 16^{th} iteration - Observed vs Recalculated

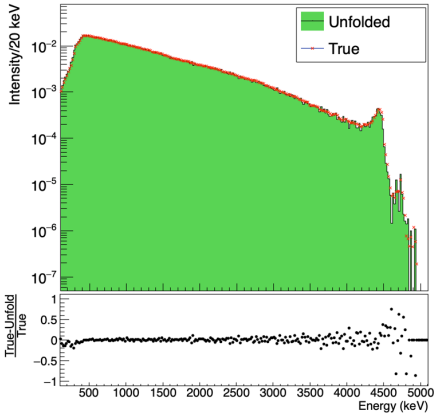

(d) 16^{th} iteration - True vs Unfolded

Figure 6.9: Comparison of the results of the unfolding process for 5 and 16 iteration numbers which corresponds to the minimum value of the χ^2 for the unfolded and true and for the observed and recalculated respectively. The set analysed is the one with 20% of statistics (1×10^6). In the left column, the observed histogram filled in blue and the recalculated spectrum in black. In the right column, the true histogram is shown by red crosses and the unfolded histogram in green. The lower plots show the residuals calculated as Eq. 6.5 and 6.6.

From this study, it is deduced that the higher the statistics, the recalculated histogram converged faster to the observed histogram as less statistical fluctuations are present, being the unfolded histogram more similar to the true decay. But with low statistics one has to cut the number of iterations down to avoid the over-fitting with the subsequent distortions in the solution.

Shape spectrum criterion

In this study we will compare the convergence of the algorithm for three different shapes of simulated spectra: discrete α emission, discrete α emission with overlap and the continuum spectrum of the previous section. In order to not get affected by the statistics, the continuum spectrum is chosen to be the 5×10^6, as the discrete spectra have similar statistics.

The upper panel of Fig. 6.10 shows the χ^2 value as a function of the iteration number for the recalculated vs observed histograms. In the lower panel, for the true vs unfolded histogram. For the comparison of the shape of the curves, the χ^2 values of the continuum spectrum have been scaled by 10 and by 100 as in the discrete spectra the χ^2 is only calculated when there is information of the true histogram.

On one hand, for the unfolded versus true histograms, the χ^2-value has a minimum for the discrete spectra at the 2^{nd} iteration and at the 5^{th} for the continuum. This can be explained because after the minima, the algorithm tries to reproduce the statistical fluctuations in the tails over-fitting.

On the other hand, for the observed versus recalculated histograms, only the continuum spectrum presents a minimum at the 3^{rd} iteration. For the discrete spectra, as larger the iteration number, the tails of each α-peak are better reproduced.

Summary of the criteria

After the exhaustive study done over the parameters involved in the p-value criterion for our case, we can conclude that:

- If the spectrum is discrete, as larger the iteration number as better the results.

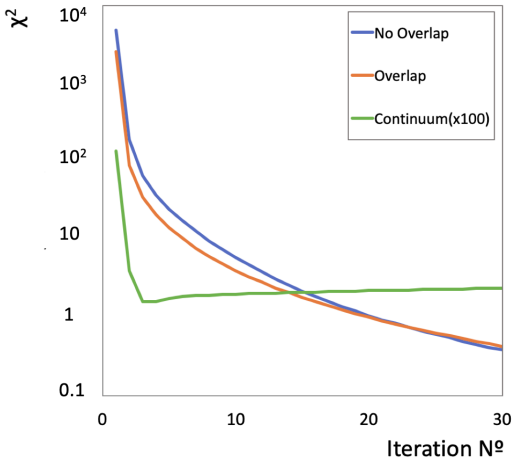

(a) Observed versus Recalculated

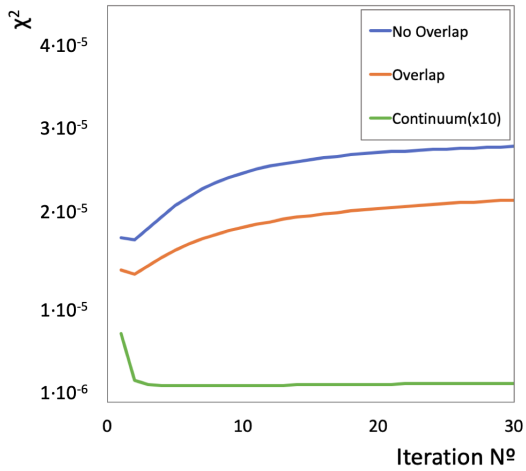

(b) Unfolded versus True

Figure 6.10: Study of the χ^2 for three spectra with different shape. The χ^2 values of the continuum spectrum are multiplied by a factor to compare within the same scale than the discrete spectra.

- If the spectrum is continuous, as higher the statistics in the whole spectrum as faster the best solution is found.
- The statistical fluctuations are important even at the first iterations, so it is important to control the unfolded spectrum in the low statistics regions to avoid the fluctuations.

6.3 UNFOLDING THE ^{8}B DECAY SPECTRUM

Once the code is tested with well-known true histograms, the unfolding process can be applied to the experimental $\alpha-\alpha$ coincidence spectrum. The solution of the unfolding (unfolded histogram) will be the β-feeding of the ^{8}B and can be used, for example, as an input for the R-Matrix analysis or as an input for a simulation to reproduce the spectrum in different conditions (another setup or another analysis).

The observed histogram has been produced only requiring the coincidence conditions explained in Sec. 5.1: the detection of the two α must be in opposite detectors and inside the cone defined by the beam-spot and the emission angle (180(5)°) and the difference in energy between the particles is defined by the polyhedron of Sec. 5.1.2.

The response function has the same analysis conditions than the experimental spectrum. It includes the energy losses at the dead layer and C-foil as well as the physics part, i.e. the effect of the recoil energy and the breakup energy of the ^{8}Be g.s. in two α ($S_\alpha = 91.84(4)$ keV).

With this approach, if the response function is properly calculated, the experimental data are less modified.

6.3.1 ^{8}B β-decay spectrum

As the β-decay of ^{8}B presents broad resonances, the true histogram is not known and therefore the optimal number of iteration can not be determined. In this case, the unfolded histogram will be the pure β-feeding to ^{8}Be nucleus. A visual check of the unfolded histogram compared with the reproducibility of the observed histogram with the recalculated histogram will give us the optimal iteration number to avoid the fluctuations at high energies and low statistics. After the previous study, as it is a continuum spectrum and with high statistics, we can assume that the χ^2-value of the recalculated and observed histograms will have a minimum and this minimum will be at an iteration number close to the one that better reproduces the true histogram.

In Fig. 6.11 one can see the χ^2-value as a function of the iteration number.

The first 20 bins (400 keV in energy) have been excluded from the analysis as they can be affected by threshold effects not considered in the response function and the aim of this work is to get focused on the high energy region. In this first channels, threshold effects and triggers efficiency can influence on the shape of the spectrum (see Sec. 7.1.4). In this case, a minimum on the χ^2 value is not seen even though it decreases quickly and gets almost stable at the 5^{th} iteration.

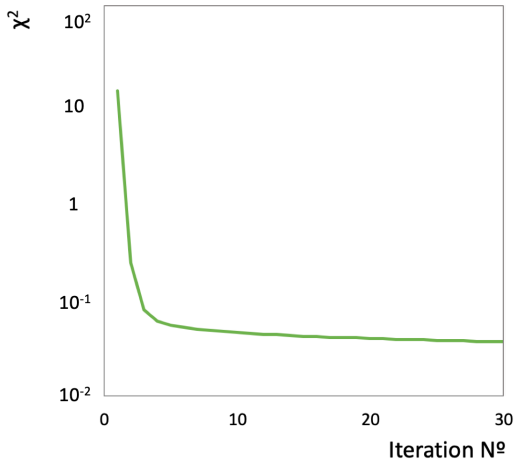

Figure 6.11: Study of the χ^2 between the observed and recalculated histograms for the α-α spectrum respect the number of iterations.

Then, the unfolded histogram will be assumed to be the one obtained at the 5^{th} iteration as it is the minimum found in the previous section and it is in good agreement with the χ^2 curve of the observed and recalculated histograms. Fig. 6.12 shows the results for this iteration. In the upper panel, the comparison between the observed and recalculated histograms with its residuals is shown. In the lower panel, the unfolded spectrum. Fig. 6.13 is the same figure but with a zoom in the high energy and low statistics region. It is clearly seen that the unfolded shape of this region is physically meaningful and the observed spectrum is well reproduced.

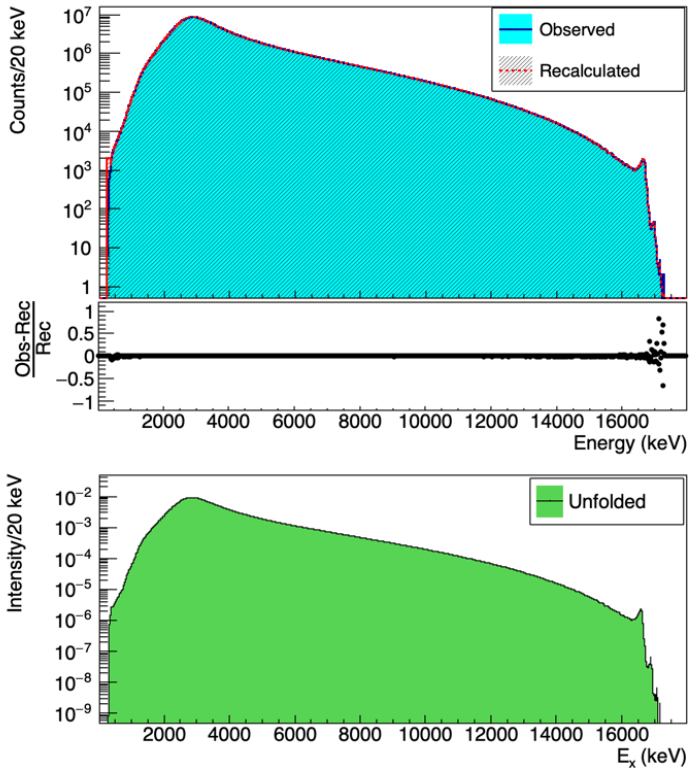

Figure 6.12: Results of the 5^{th} iteration of the unfolding procedure for the α-α coincidence spectrum from ^{8}B β-decay. The first 20 bins (400 keV in energy) are excluded of the analysis. The upper panel shows the comparison between the observed and recalculated histograms with its residuals. In the lower panel, the unfolded spectrum (β-intensity distribution).

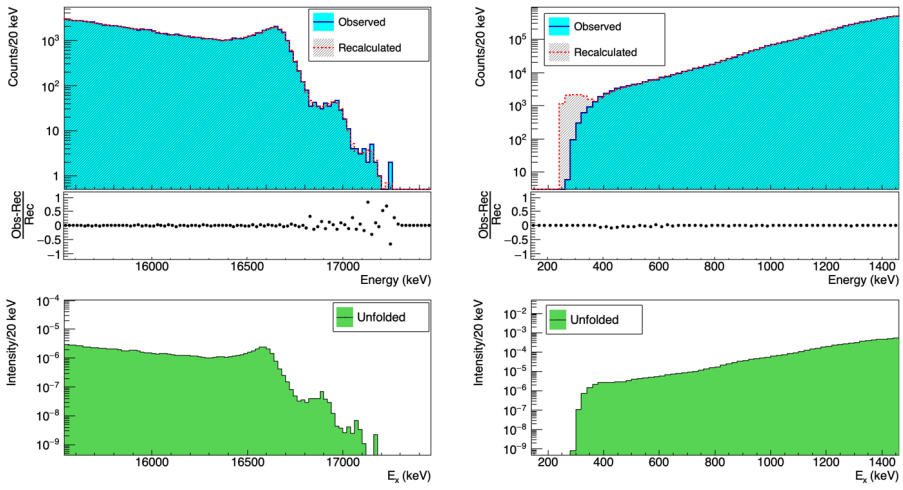

(a) High energy region

(b) Low energy region

Figure 6.13: Zoom on the high energy (left panel) and low energy (right panel) regions of the results of the 5^{th} iteration of the unfolding procedure for the α-α coincidence spectrum from ^{8}B β-decay. The first 20 bins (400 keV in energy) are excluded of the analysis. The upper panels show the comparison between the observed and recalculated histograms with its residuals. In the lower panels, the unfolded spectrum (β-intensity distribution).

6.3.2 R-Matrix analysis of the unfolded spectrum

With the unfolded histogram obtained in the previous section, we have repeated the R-matrix analysis done in Sec. 5.4 but with the purely β-feeding spectrum as the unfolded spectrum represents the β/EC-feeding of ^{8}B into ^{8}Be and has corrected recoil and experimental effects. In this case, the response function included in the ORM program is the unit, as the spectrum has all the experimental effects removed.

In this case, the starting point has been the solution adopted for the holistic approach of the experimental data analysed in Sec. 5.5. Following the same procedure, first the 2^+ doublet has been fixed reducing the region from 16 to 17.2 MeV. Once the doublet is well fitted, the fitting range is opened from 2 to 17.2 MeV and the parameters of the 3 MeV level and background are set free. Fig. 6.14 shows the resulting fit with its residuals. The χ^2/d.o.f from 2 to 17.2 MeV is 14.8, almost the same than the χ^2/d.o.f obtained in Sec. 5.5 in the same range (χ^2/d.o.f$_{holistic,2-17MeV}$=14.4).

From this last parameters, we have tried to fit the unfolded spectrum fixing the sum of the Fermi components to 2. Fig. 6.15 shows the fit obtained when this constrain is applied. In this case, the χ^2/d.o.f is 10.5, being the best fit we have obtained so far.

In Tab. 6.3 one can see the resulting parameters of each level for both fits and compared with the holistic fit obtained in Sec. 5.5. Since our error derived from the unfolding procedure does not include correlations, we have adopted the following criterion: errors in the width and the intensity parameters smaller than 10% (only statistical) have been fixed to 10% to account for correlations in the unfolding procedure and systematic errors in the fit. For the energies, the criterion assumed has been 1% of the 3 MeV level and 0.5% for the energies of the doublet. From the results presented, one can see the stability of the Gamow-Teller components for each level. These results will be further discussed in Sec. 8.2 where the isospin mixing parameters are derived from the R-Matrix fit.

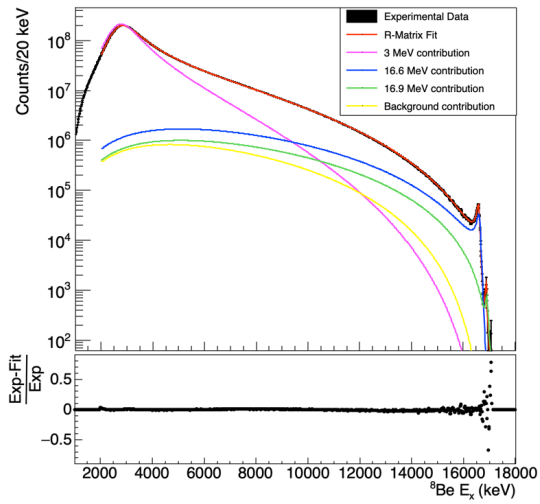

(a) Full spectrum

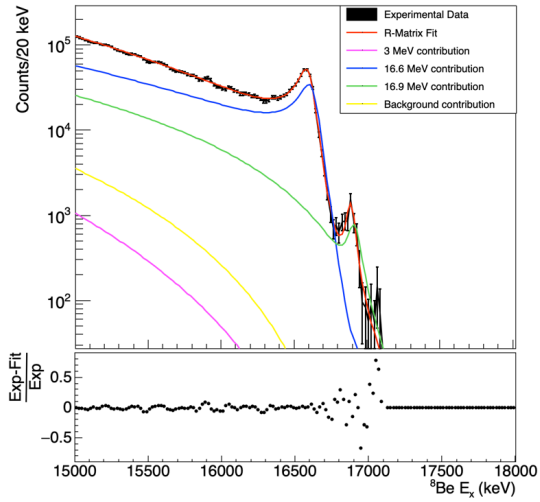

(b) 2^+ doublet region

Figure 6.14: R-Matrix analysis of the ^{8}B β-feeding distribution obtained with the unfolding procedure. The upper panel shows the experimental data (black) and the result of the R-matrix fit (red) for the full spectrum. The lower panel shows a zoom on the doublet region. The residuals are shown in the lower panel of each figure.

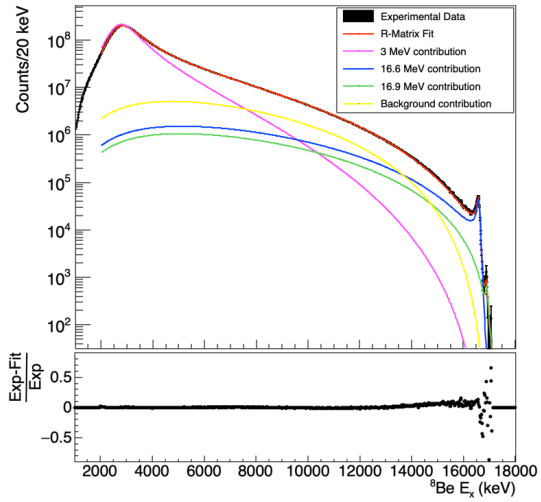

(a) Full spectrum

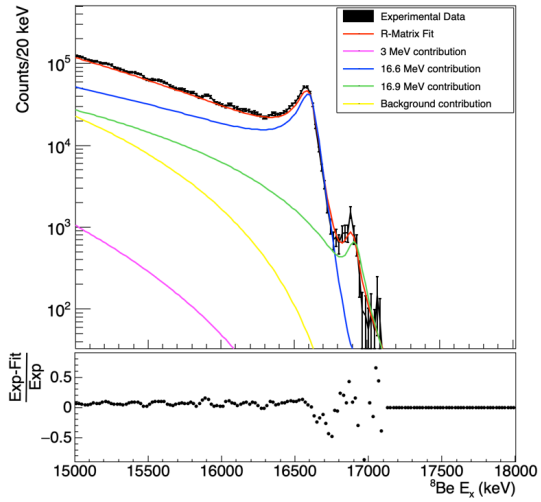

(b) 2^+ doublet region

Figure 6.15: R-Matrix analysis fixing $\sum B_F$=2 of the ^{8}B β-feeding distribution obtained with the unfolding procedure. The upper panel shows the experimental data (black) and the result of the R-matrix fit (red) for the full spectrum. The lower panel shows a zoom on the doublet region. The residuals are shown in the lower panel of each figure.

Table 6.3: Comparison of the parameters obtained from the β-feeding distribution compared with the holistic fit. The first column refers to the holistic fit (above 1 MeV). The second column shows the parameters of the β-feeding spectrum. The third column shows the results of the fit to the β-feeding spectrum when fixing the sum of the B_F=2.

Parameters		**Holistic Fit**	**β-feeding fit**	**β-feeding fit with $\sum B_F$=2**
r_0 (fm)		1.35	1.35	1.35
χ^2/d.o.f (2-17.2 MeV)		14.4	14.8	10.5
2_0^+	**E (keV)**	3052(37)	3053(31)	3058(31)
	B_{GT}	0.011813(56)	0.01064(53)	0.01055(52)
	$\Gamma_{\alpha\alpha}$(keV)	1957(15)	1884(94)	1876(94)
2_1^+	**E (keV)**	16632(54)	16629(83)	16617(83)
	B_F	0.63(24)	0.719(88)	1.052(53)
	B_{GT}	0.98(14)	0.927(46)	0.73(28)
	$\Gamma_{\alpha\alpha}$(keV)	129.47(28)	127.7(64)	118(14)
2_2^+	**E (keV)**	16921(20)	16915(85)	16918(85)
	B_F	1.08(24)	0.97(29)	0.948(47)
	B_{GT}	0.57(14)	0.587(30)	0.532(26)
	$\Gamma_{\alpha\alpha}$(keV)	112.5(11)	101.8(57)	109(58)
2_{Bkg}^+	**E (keV)**	21205	21437	21054
	B_{GT}	1.3438	0.8048	0.36804
	$\Gamma_{\alpha\alpha}$(keV)	119.11	253.9	3281

Considering as the best fits obtained with the R-Matrix analysis the holistic one and the β-feeding fit with the restriction of $\sum B_F$=2, these can be compared with the adopted values published in [Tea04] (see Tab. 6.4). One thing to remark is that in the fit of the β-feeding, the background level is wider than in the holistic fit as expected.

We have noticed that with all the fits done in this thesis, the widths of the levels differ from the published values in [Tea04] obtained from reaction studies, especially the width of the 3 MeV level. We have tried to fit the unfolded spectrum with the constrain $\sum B_F$=2 fixing the width of the 3 MeV level to a value close to the published one, namely 1500 keV. Despite our efforts, the fit obtained is worse than the ones presented previously and will not be included.

Table 6.4: Comparison of the parameters obtained from the two best R-Matrix fits with the published values in [Tea04] (the first column). The second column refers to the holistic fit. The third column shows the results of the fit to the β-feeding spectrum when fixing the sum of the B_F=2.

Parameters		**Adopted values**	**Holistic Fit**	**β-feeding fit with $\sum B_F$=2**
r_0 (fm)		1.35	1.35	1.35
2_0^+	**E (keV)**	3030(10)	3052(37)	3058(31)
	B_{GT}	0.011813(56)	0.01064(53)	0.01055(52)
	$\Gamma_{\alpha\alpha}$(keV)	1513(15)	1957(15)	1876(94)
2_1^+	**E (keV)**	16626(3)	16632(54)	16617(83)
	B_F		0.63(24)	1.052(53)
	B_{GT}		0.98(14)	0.73(28)
	$\Gamma_{\alpha\alpha}$(keV)	108.1(5)	129.47(28)	118(14)
2_2^+	**E (keV)**	16922	16921(20)	16918(85)
	B_F		1.08(24)	0.948(47)
	B_{GT}		0.57(14)	0.532(26)
	$\Gamma_{\alpha\alpha}$(keV)	74.0(4)	112.5(11)	109(58)
2_{Bkg}^+	**E (keV)**		21205	21054
	B_{GT}		1.3438	0.36804
	$\Gamma_{\alpha\alpha}$(keV)		119.11	3281

Search for the β-delayed proton

7

7.1 METHODOLOGY

The methodology followed in this chapter changes from what has been done previously. The determination of the upper limit of the branching ratio of the β-delayed proton, corresponding to the process ^{8}B$\rightarrow$ ^{8}Be*(17.6 MeV) $\rightarrow$ p + ^{7}Li, starts comparing the experimental and simulated spectrum without conditions to ensure that we can reproduce with GEANT4 the physics of the experiment. Once the simulation is validated, a set of mono-energetic protons will be simulated, processed and added to the experimental spectrum. The amount of simulated protons required to statistically identify a proton-peak that will determine the upper limit of the branching ratio.

Since the proton is emitted when the 17.6 MeV state of ^{8}Be is populated via EC with a very low branching ratio ($<3\times10^{-8}$ estimated), the data cannot be analysed as in the previous chapters as no other particle must be in coincidence with the low-energy proton of $\sim$330 keV. For this purpose, an anti-coincidence analysis has to be performed to get rid of the coincident α particles that dominate the spectrum: now only the proton should be detected. The data-sets used and the analysis applied to the experimental and simulated data are detailed in Sec. 7.1.1 and Sec. 7.1.3 respectively. Important to notice that in this case the threshold conditions will play an important role.

Moreover, due to the extremely low branching ratio estimated from the ^{7}Li

decay [BFF$^+$13], we do not expect to observe a proton peak in the spectrum and therefore the information that will be extrapolated from this analysis is an experimental upper limit of the branching ratio for the β-delayed proton. For determining this limit, a set of simulations have been performed and compared with the experimental data. The process of preparing the input of the simulation is explained in Sec. 7.1.2

Finally, the experimental effects that can be evaluated must be included in the simulations. Those effects are the efficiency of the trigger and the effect of the electronic threshold. These will be evaluated in Sec. 7.1.4.

7.1.1 Experimental Data-sets

As explained in Sec. 4.4, the experimental data are divided in three sets with different electronic thresholds and dead time. In this section and due to the low energy of the emitted proton, ∼330 keV, two of the three sets of data are used: the one with the thresholds increased up to 2.5 MeV cannot provide information for the region of interest and it has been disregarded.

The two sets of data of low thresholds will be treated individually in the analysis since they can have small differences in the thresholds because they were set manually in both cases (see Sec. 7.1.4). Fig. 7.1 shows the comparison between the two sets of data where already some discrepancies in the low energy region are seen. The name of each set has been assigned arbitrarily so the first set of data (in blue) is the set of data with the first electronic thresholds and the second (in red), the last set of data of the experiment corresponding to the third change in the electronic thresholds. The upper panel is the energy signal detected in detector U2 without analysis. The lower panel shows the residuals between both sets once they are normalized to 1.

The first data-set amounts to 72% of the total statistics analysed. The second data-set, to 28%. This proportion will be considered when applying the TDC correction to the output of the simulation, as due to the change on the electronic thresholds, the low energy region, below 500 keV, of the two data-sets is different.

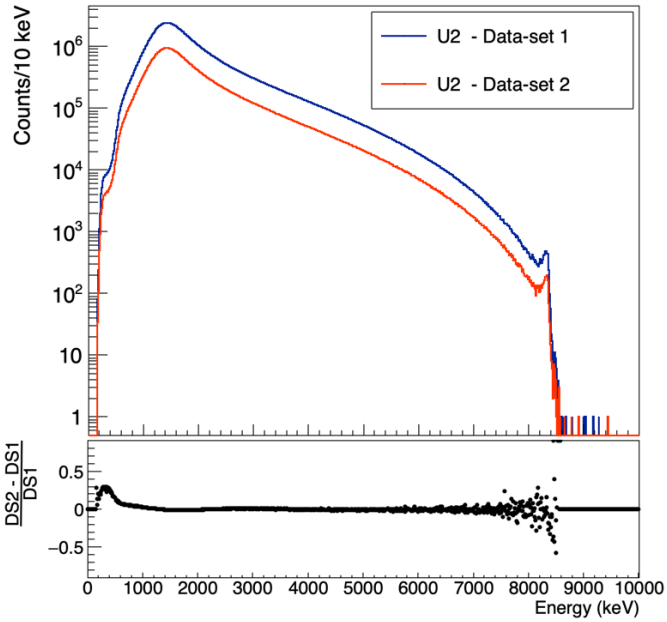

Figure 7.1: Comparison of the data-sets used for the analysis of the β-delayed proton. In blue, the data-set with the first electronic threshold configuration, arbitrarily named Data-set 1. In red, the data-set with the third electronic threshold configuration, arbitrarily named Data-set 2. No analysis is applied to the spectra. The lower panel shows the residuals when the data-sets are normalized to 1.

7.1.2 GEANT4 simulations

When simulating the decay of the ^{8}B nucleus, one has to take into account the population to the wide resonances in the daughter, however, this is not included in GEANT4. This forces us to define our radioactive decay file for both nuclei involved, ^{8}B and ^{8}Be, as the decay paths must match.

The radioactive decay file of the ^{8}B has been obtained from the solution of the unfolding procedure (Sec. 6.3). The unfolded spectrum represents the β/EC-feeding of ^{8}B into ^{8}Be and has corrected recoil and experimental effects. The spectrum has been normalized to one and discretized into 20 keV bins, obtaining the probability of β/EC-decay in each bin. Then, for each energy bin, the ratio EC/β^{+} has been calculated using the LOGFT.FOR code [nds].

GEANT4 requires a determined format for the radioactive decay files. The left panel of Fig. 7.2 shows some of the lines of the decay file of ^{8}B. The first two lines are just informative for the user and present the content of each column. The third line determines the excitation level from where the decays will occur and the half-life of the nucleus. For the ^{8}B nucleus, as there is no excitation energy it is set to 0 in the first column and the half-life is set to 0.77 s. The next lines that only have three columns represent the summary of the available decay modes and the branching ratio of each mode. The sum of the different modes must be equal to 1. The following lines with five columns are the decay to different excitation energies of the daughter nucleus. In the first column, the decay mode is specified. In our case, `BetaPlus` for β^{+}-decay and `KshellEC` for the electron capture from the K-shell. The second column is the excitation energy populated of the daughter nucleus. The fourth and fifth columns are the decay probability in percentage and the Q-value of each decay, which is calculated subtracting the excitation energy of the daughter to the Q-window of the β/EC-decay.

The radioactive decay file of the ^{8}Be has the same structure. In this case, the excitation energy from where the α decay occurs is forced to match the excitation energy of the daughter specified in the ^{8}B radioactive decay file. Each line starting with a `P` defines the excitation energy populated from ^{8}B. As the α-break-up of the ^{8}Be is instantaneous[1], the half-life is set to an extremely low value. A section of the code is shown in the right panel of Fig. 7.2, where the

[1] $\Gamma_{c.m.} = 6.8(17)eV$ [ASL74].

α breakup is defined as decaying to one α with 100% of probability.

```
# 8B ( 770 MS    )
# Excitation  flag  Halflife  Mode     Daughter Ex flag  Intensity      Q
P          0  -       0.77
                             BetaPlus       0      0.99999717
                             KshellEC       0      0.00000283
                             BetaPlus     300   -    0.000004     17679.80
                             BetaPlus     320   -    0.000028     17659.80
                             BetaPlus     340   -    0.000081     17639.80
(...)
                             BetaPlus    2840   -    0.930091     15139.80
                             BetaPlus    2860   -    0.928826     15119.80
(...)
                             BetaPlus   16040   -    0.000138     1939.80
                             BetaPlus   16060   -    0.000146     1919.80
                             BetaPlus   16080   -    0.000145     1899.80
                             BetaPlus   16100   -    0.000135     1879.80
(...)
                             BetaPlus   16800   -    0.000002     1179.80
                             BetaPlus   16820   -    0.000001     1159.80
                             BetaPlus   16840   -    0.000001     1139.80
                             KshellEC   16340   -    0.000001     1639.80
                             KshellEC   16360   -    0.000001     1619.80
                             KshellEC   16380   -    0.000001     1599.80
(...)
                             KshellEC   16920   -    0.000004     1059.80
                             KshellEC   16940   -    0.000003     1039.80
                             KshellEC   16960   -    0.000001     1019.80
```

(a) Part of the radioactive decay file of the ^{8}B nucleus created from the β-feeding spectrum

```
# 8BE ( 8.1814e-17)
# Excitation  flag  Halflife  Mode     Daughter Ex flag  Intensity      Q
(...)
P          300  -    1.30e-22
                             Alpha          0      1
                             Alpha          0  -   100     391.84
P          320  -    1.30e-22
                             Alpha          0      1
                             Alpha          0  -   100     411.84
P          340  -    1.30e-22
                             Alpha          0      1
                             Alpha          0  -   100     431.84
(...)
P         2840  -    1.30e-22
                             Alpha          0      1
                             Alpha          0  -   100    2931.84
P         2860  -    1.30e-22
                             Alpha          0      1
                             Alpha          0  -   100    2951.84
P         2880  -    1.30e-22
                             Alpha          0      1
                             Alpha          0  -   100    2971.84
P         2900  -    1.30e-22
                             Alpha          0      1
                             Alpha          0  -   100    2991.84
(...)
P        16800  -    1.30e-22
```

(b) Part of the radioactive decay file of the ^{8}Be nucleus

Figure 7.2: Part of the radioactive decay files of the ^{8}Be and ^{8}B nuclei for the GEANT4 simulation.

The setup used for the simulations is the same already defined in Sec. 4.3.3 and Sec. 4.3.4. It includes each DSSD defined with the different dead layers in their measurement position. It also includes the PAD detectors as a continuous silicon square volume with a thickness of 1000 μm and 1500 μm respectively. For the PADs, a continuous dead layer is included with the thickness defined by the manufacturer. Fig. 7.3 shows a view of the setup defined, being in blue the DSSDs and in red the PADs. The C-foil is placed in its position (Sec. 4.3.2) and in the figure it is shown in the center of the setup.

In order to compare the results of the simulation with the experimental data, a large amount of statistics is needed. Due to the solid angle covered by the detectors, a total of 10^9 ^{8}B decays have been simulated. To be able to simulate this large number of events, 1.0001 consecutive simulations of 1.000.000 events have been simulated, being the initial seed of the i-simulation the next seed of the last event of the *(i-1)*-simulation.

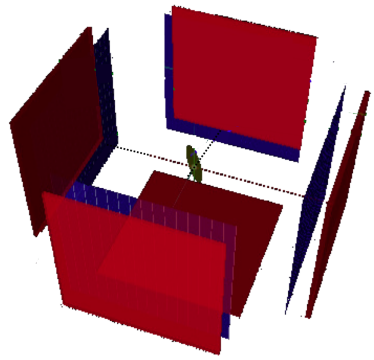

Figure 7.3: View of the setup defined in GEANT4. In blue, the DSSDs. In red, the PADs and U5. The C-foil is at the center of the setup.

7.1.3 Analysis

The physics that is studied in this chapter changes completely the methodology of the analysis. As the 17.6 MeV state is populated by electron capture, the only particle that can arrive at one detector is the 337 keV proton. Therefore, only the events where only one detector has fired will be kept. Following the notation used in Sec. 2.2.3, events with multiplicity equal to 1 will be selected. This is a restrictive condition and can reduce significant statistics since random coincidences of a *true* signal with a noise signal will be rejected. To avoid the suppression of these events, a new multiplicity is created which only increases if the signals are above the noise, roughly 150 keV. The multiplicity condition is required with this new condition.

After studying the effectiveness of the anti-coincidence analysis compared with the remaining statistics, we have decided to reduce the detectors to10×10 strips in order to ensure the detection of the both coincident α-particles. By reducing the detectors, border effects and the noisiest strips (see Sec. 4.1.3) are suppressed.

The same analysis is applied to experimental and simulated data.

7.1.4 Trigger efficiency and threshold shape

Besides the analysis, some technical issues must be handled to properly compare experimental data with simulated data.

On the experimental side, many events lose the corresponding time signal due to problems with the electronic modules used (either the leading edge discriminator or the trigger module). This produces a deficit in the multiplicity equal to 1 signals as the trigger is done with the time signal. This effect must be taken into account as this study is reduced to the events where the detector has self-triggered.

The study of the efficiency of the trigger is done per detector and for the two sets of data. Fig. 7.4 shows the trigger efficiency for each detector, in solid line for the first data-set and in dashed line for the second. The curve has been obtained dividing the *singles* spectrum[2] by the energy spectrum when time signal exists with the detectors reduced to 10×10 strips. In the figure presented (Fig. 7.4) three of the four detectors were set at similar thresholds but one, U4, has a difference on the threshold of roughly 300 keV between the first and the second data-set.

By looking in detail the low energy region of the efficiency of the trigger, the only detector that can be used for this analysis is U2, since it is the one that has the largest efficiency at low energy, above 10% at 400 keV. Traditionally, a *singles* spectrum would be produced with the energy signal connected directly to a histograming memory, with no restrictions at all. However, in our case, the *singles* spectrum is just an *'OR'* condition in the trigger module. This means that our *singles* spectrum is acquired whenever any detector has given a time signal. Fig.7.5 shows the comparison between the two spectra for detector U2 in the upper panel. In the lower panel, the ratio bin per bin that produces the trigger efficiency curve.

The correction of the trigger efficiency will be applied to the simulated data following Eq. 7.1, where the amount of statistics in each data-set is concerned. C_f is the amount of counts corrected by the efficiency bin per bin, C_0 the initial counts of the bin and eff_{DS1} and eff_{DS2} the efficiency curve of the first and second data-set respectively.

[2]See following paragraph for discussion about *singles* spectrum

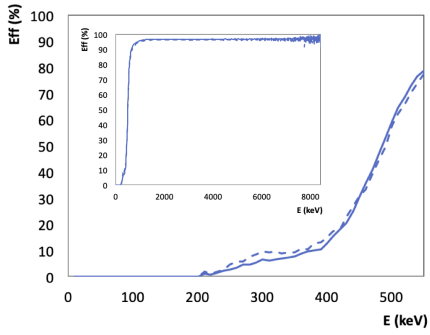

(a) Detector U2

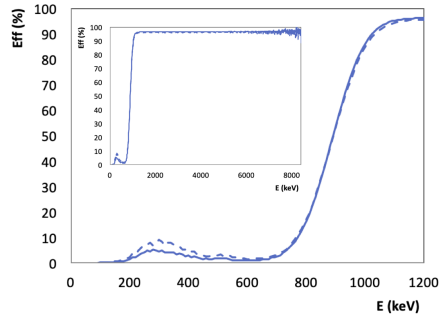

(b) Detector U6

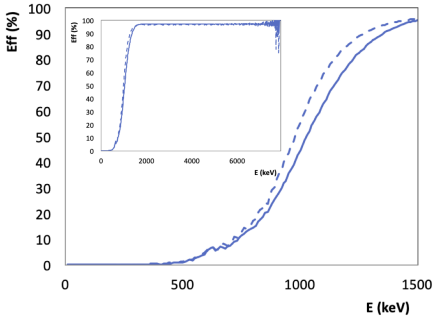

(c) Detector U3

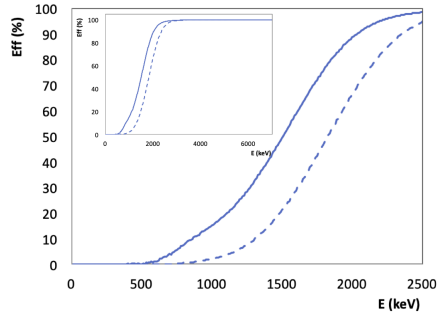

(d) Detector U4

Figure 7.4: Trigger efficiency for each detector. The solid line is the efficiency of the first data-set. The dashed line, for the second. The curves have been obtained dividing the *single* spectrum of each detector by the one that is produced with time signal associated.

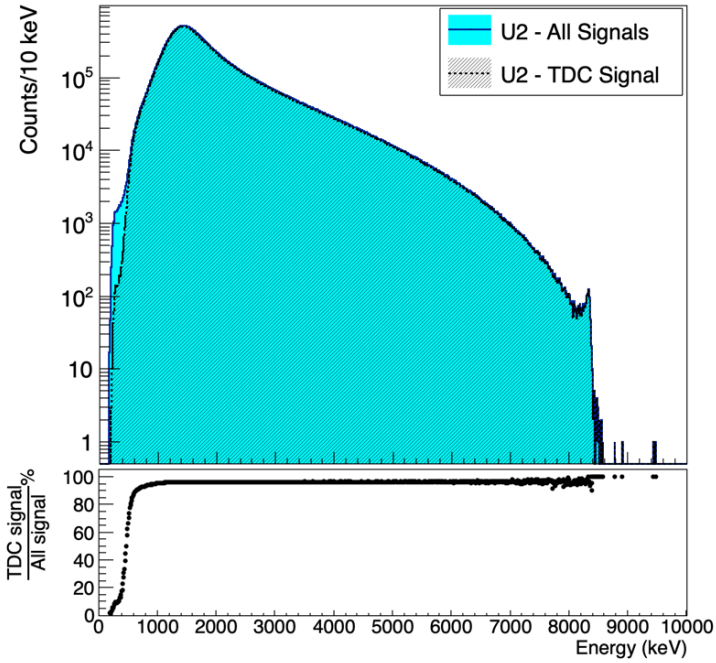

Figure 7.5: Comparison between *single spectrum* (in blue) and the spectrum with time signal associated to the detector (in grey). Both spectra are experimental data of detector U2. The lower panel is the trigger efficiency curve obtained dividing bin per bin the spectrum with time signal by the *singles* spectrum. This efficiency curve has been applied to the simulated data.

$$C_f = C_0(0.72 \times eff_{DS1} + 0.28 \times eff_{DS2}) \tag{7.1}$$

On the other hand, the fact that the threshold configuration in the experimental data is done with a leading edge module produces a non-sharp threshold. In the simulations, the threshold is included as a cut below certain energy. To correct for the experimental threshold, a curve is obtained comparing the energy spectrum of experimental and simulated data below 600 keV. The upper panel of Fig. 7.6 shows the experimental (blue) and simulated (grey) *singles* spectra of detector U2. The experimental data have been scaled to the simulated. In the lower panel is shown the ratio bin per bin between the two spectra, obtaining the curve of the electronic threshold below 600 keV.

The choice of correcting the threshold curve below 600 keV is justified as it is the region where the simulated data are over the experimental data. Moreover, the effect of the threshold at low energies should not be noticed at larger energies.

The threshold shape correction has to be applied to the simulated data without distinction on the analysis applied. The trigger efficiency only will affect to the multiplicity equal to 1 condition, so it has to be corrected only in the simulated anti-coincidence spectra.

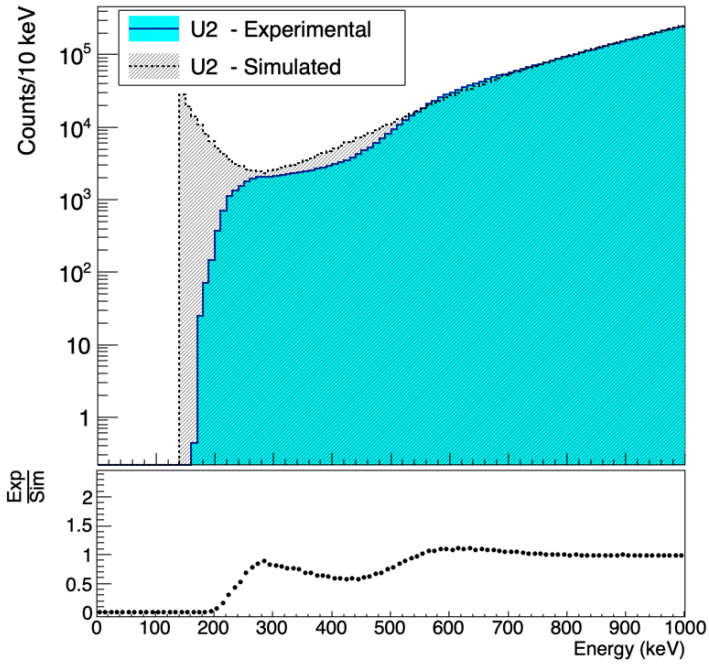

Figure 7.6: Comparison between experimental (in blue) and simulated (in grey) *singles* spectra of detector U2. The lower panel is the electronic threshold curve obtained dividing bin per bin the experimental data by the simulated data. This efficiency curve has been applied to the simulated data below 600 keV.

7.2 VALIDATION OF THE SIMULATIONS

As said previously, we need to rely on the Monte Carlo simulations to calculate the response of the detector to the EC-delayed proton and estimate the upper limit of the branching ratio of the proton. Therefore, we first need to validate the physical models used in the simulation, ensuring that the simulated data matches the experimental data.

The validation of the simulation is done with the comparison between the singles spectra: the experimental and the simulated data. In this comparison, only the threshold curve shape is corrected in the simulated data. The upper panel of Fig. 7.7 shows the comparison of both spectra, being the blue the experimental data and the grey the simulated one. In the lower panel the residuals between both spectra are shown.

Due to the correction applied, the region below 600 keV matches perfectly. Above the correction, the good agreement between the *singles* spectra demonstrates that the simulations can reproduce the physics of the experiment and also is a proof that the effect of the non-sharp threshold only affects to the corrected region below 600 keV. At higher energies, above 8 MeV, the divergences between experimental and simulated data are enhanced due to the poor statistics in the simulation in this region. However, our interest with the simulations is to reproduce the low energy region and the shape of the spectrum.

When applying the anti-coincidence analysis, which includes the trigger efficiency correction, simulation and experiment are in good agreement on the low-energy region. The comparison between the two spectra is shown in Fig. 7.8. Of course, the corrections applied do their best to reproduce all the electronic phenomena that can occur in an experiment despite there is a lack of knowledge, since even the so called *singles* spectrum is not really singles because it is acquired as an OR of the trigger module, and this requires at least one detector to fire and, therefore, it is subject to threshold effects. This last efficiency can not be estimated experimentally and we have decided to keep the simulations with the corrections explained otherwise the information from the simulation would be lost. Despite the divergence between the two anti-coincidence spectra (simulated and experimental), in the region of interest where the proton-peak can be found (from 310 to 350 keV) both are in good agreement within the statistical error.

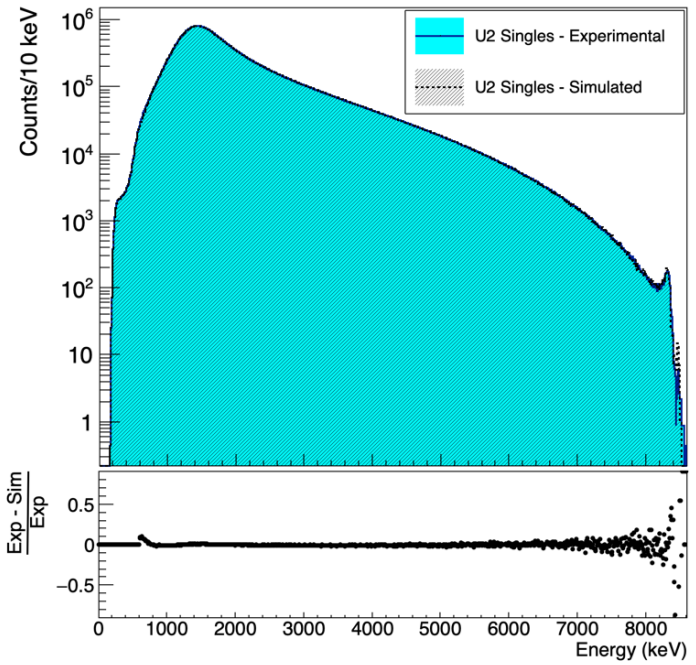

Figure 7.7: Validation of the simulations: comparison of the *singles* experimental (blue) and simulated (grey) spectra. The simulations have been corrected by the threshold curve below 600 keV. The experimental spectrum is scaled to the simulations.

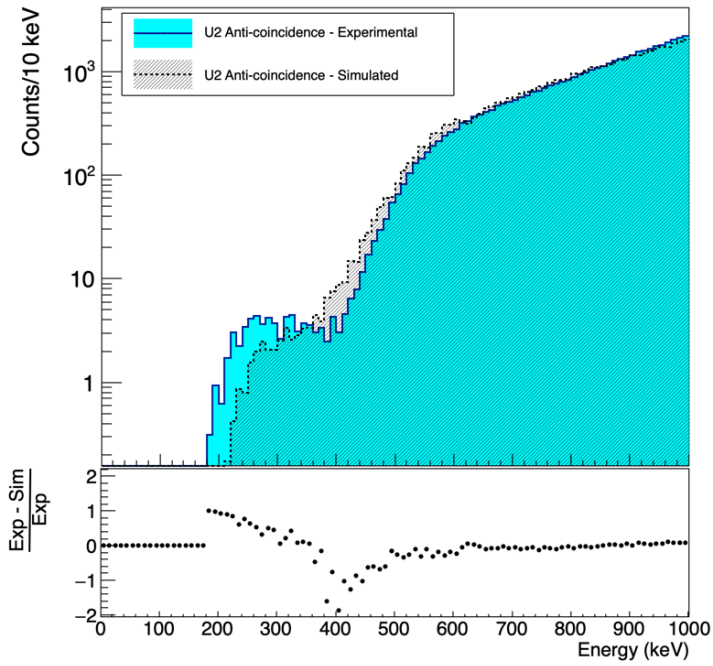

Figure 7.8: Validation of the simulations: comparison of the anti-coincidence experimental (blue) and simulated (grey) spectra. Experimental data are scaled to the simulations.

7.3 DETERMINATION OF THE UPPER LIMIT BRANCHING RATIO OF THE PROTON

Once the simulations are validated, the upper limit will be set simulating a set of 330 keV protons in 4π as a narrow distribution from the decay of the ^{8}B into the 17.64 MeV state, analysing them following the anti-coincidence analysis with the corrections explained before, and adding the resultant spectrum to the anti-coincidence experimental spectrum.

The experimental spectrum has been scaled to the simulated anti-coincidence spectrum so the total amount of decays will be assumed to be the same than the simulated ones: 10^{9} events of ^{8}B in 4π. For determining statistically the branching ratio we compare the height of the resultant proton peak with the background, the proton peak is fitted with a Gaussian over a lineal background.

To determine the experimental sigma of the background level two different approaches have been followed. The first one is based on calculating the σ by doing the square root of the original counts in the bin and then scaling the sigma as the data. For the bin centred on the maximum of the Gaussian used to fit the proton peak, this value is $\sigma = 0.54$ over 3.74 counts in the bin. The second approach consists in fitting the *plateau* in a larger region, from 270 to 390 keV, and get the standard deviations of the experimental data over the fit. This produces a $\sigma = 0.61$ over the 3.49 counts. As both methods give similar results, the second approximation will be used to determine the height of the peak. Fig. 7.9 shows the peak shape for two cases: 1000 and 2000 protons simulated. In both cases, the statistics of the protons are too low to identify a peak and therefore a Gaussian fit to the proton peak cannot be done.

Different statistics of protons are analysed and compared with the experimental data once the peak is added. Tab. 7.1 summarises the results for different cases. The remaining counts of the background are subtracted to the height of the centroid of the Gaussian that fits the peak and the result is compared with the statistical error of the experimental data.

In Fig. 7.10 one can see the comparison between the anti-coincidence experimental spectrum (blue) and the same spectrum once the proton peak is added (grey) for the cases studied when the proton peak is clearly visible over the background.

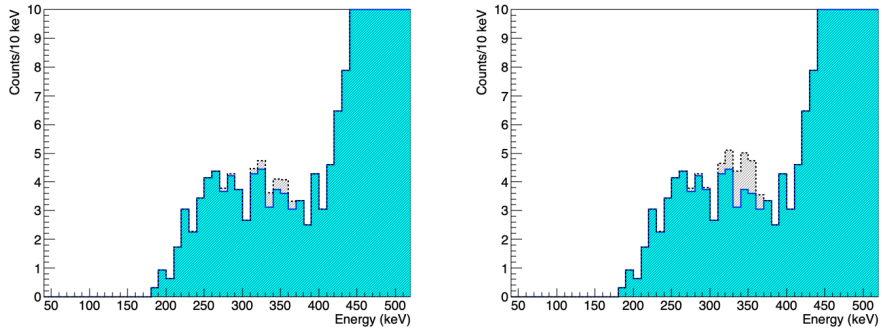

(a) 1000 protons simulated

(b) 2000 protons simulated

Figure 7.9: Comparison of the peak-shape for different amount of protons simulated where the proton peak is not visible over the background. In each figure, in blue the anti-coincidence experimental spectrum and in grey the same spectrum when the proton peak is added.

Table 7.1: Comparison of the height of the centroid of the Gaussian that fits the proton peak as a function of the protons analysed. The height is defined over the lineal background of the experimental data (a total of 3.49 counts). The value in the N_σ column is the the height of the peak expressed as a the number of σ of the experimental data, which has been calculated as the standard deviation of the data over the lineal fit ($\sigma = 0.61$).

Protons analysed	**Height**	**N_σ**	**Branching Ratio**
2500	1.66	3.0	2.5×10^{-6}
3000	2.03	3.8	3.0×10^{-6}
3500	2.58	4.8	3.5×10^{-6}
4000	3.09	5.7	4.0×10^{-6}
5000	4.05	7.5	5.0×10^{-6}

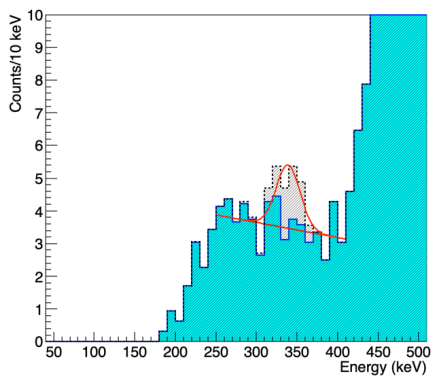

(a) 2500 protons simulated

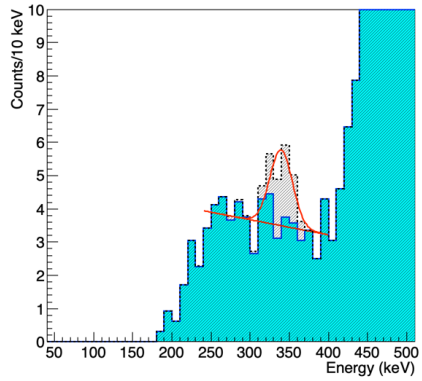

(b) 3000 protons simulated

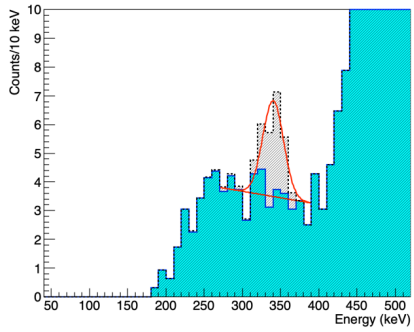

(c) 4000 protons simulated

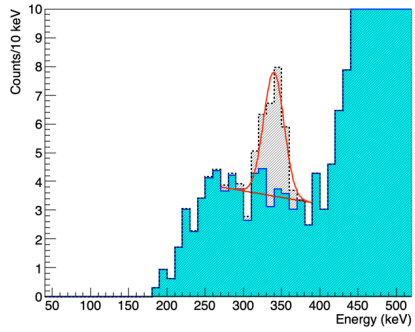

(d) 5000 protons simulated

Figure 7.10: Comparison of the peak-shape for different amount of protons simulated where the proton peak is clearly visible over the background. In each figure, in blue the anti-coincidence experimental spectrum and in grey the same spectrum when the proton peak is added.

According to the results, we determine the experimental upper limit as 2.5×10^{-6} within a confidence level of 99.9 % (3σ).

Results and Discussion

8

8.1 β-STRENGTH

8.1.1 Comparison with previous experiment

The previous experiment of β-decay of ^{8}B was performed by our collaboration in 2008 at JYFL, Jyväskylä [Kea11]. The present results are compared with this experiment for two main reasons. The first one is that the setup used was the previous version of the one used in the experiment analysed in this thesis. The main modification is that the detectors were not attached to a plastic structure at that time. The second reason is that, prior to this work, the 2008 experiment is the experiment of β-decay with the highest statistics above 16 MeV. However, only 5 counts were assigned to the 16.9 MeV level. Comparing the statistics of the two experiments, there is a factor of $\sim$70 between the new experiment and the 2008 JYFL one, which allows to properly study the upper region of the Q_{EC} window. This factor is obtained comparing bin per bin the amount of counts in the excitation spectrum in both experiments.

In order to highlight the relevance of the new information that the IS633 experiment provides to the study of the nuclear structure of ^{8}Be, Fig. 8.1 shows the comparison between the β-strength distributions[1] obtained in JYFL experi-

[1] In reality this is not a β-strength distribution but the general trend of it. The reason is that, in this section, we have calculated it from the excitation spectrum without the unfolding, therefore it includes the resolution of the detectors.

ment (red) and in the IS633 experiment (blue). In the former, the low statistics above 16 MeV prevents to obtain information of the 2^+ doublet as can be seen by the statistical fluctuations at the end of the strength distribution, while with the new experiment the two states are well distinguished and the data can now be used to disentangle the isospin mixing between the states that conform the doublet. To obtain the trend of the β-strength distribution, the data from both experiments have been normalized to one and divided by the phase space factor $f(Q_{EC}\text{-}E_x)$, which is obtained from the LOGFT.for code [nds]. From the figure it is obvious that, even though the β-decay proceeds mainly to the broad resonance at 3 MeV (due to the phase space available), in reality the β-strength peaks at 16.6 and 16.9 MeV get most of the β-decay operator strength.

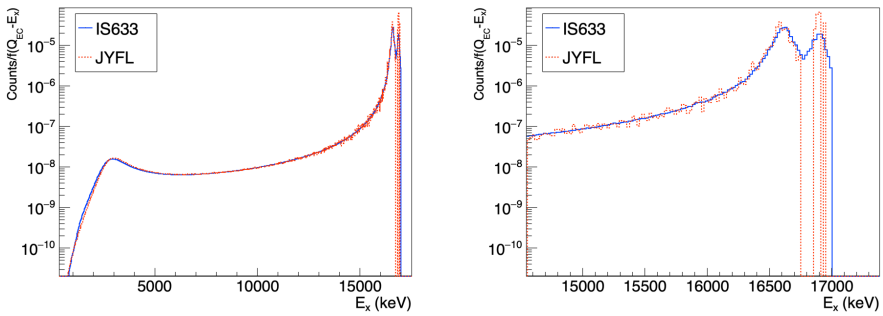

Figure 8.1: Comparison of the trend of the β-strength distribution as a function of the excitation energy of ^{8}Be. In red, the data from the experiment done in Jyväskylä in 2008 (JYFL). In blue, the data from the IS633 experiment, subject of this thesis. Both distributions have been normalized to one and divided by the phase space factor. The right panel is a zoom on the high energy region.

Apart from constants and the response function folded in the spectra, dividing the excitation spectrum by the phase-space factor and the half-life has the same trend than the β-strength, enhancing the importance of the doublet. For the JYFL experiment, the fluctuations above 16.5 MeV (see Fig. 8.1, right) produce a wrong β-strength distribution as can be seen in the region between 16.7 and 17 MeV due to the holes and the spikes produced by the 5 counts registered at the 16.9 MeV state. The wrong distribution of the β-strength prevented from drawing conclusions on the isospin mixing from the JYFL run. Moreover, an R-Matrix fit could not be done in this region as 5 counts are not enough to

produce a peak-shape. With the IS633 experiment, the two states that form the doublet are clearly seen and have a shape that can be fitted and analysed within the R-Matrix formalism, being a significant improvement on the β-decay experimental data as will be seen in the next section.

8.1.2 Obtaining the B_{GT}

In the previous section the excitation spectrum of ^{8}Be was used for the comparison with the previous experiment. This spectrum, as explained before, is the α-α coincidence spectrum corrected by the energy of the recoil, the dead layers of the detectors involved and the separation energy of the α. However, this spectrum is still distorted by the detector response, which will be removed in the following by the use of the response function and the unfolding procedure (see Sec. 6.2 and 6.3).

To properly calculate the β-strength distribution $S_\beta(E)$ and extract the B_{GT} of the decay, the starting point should be the β-feeding. From the β-feeding, one can apply Eq. 1.21 to calculate bin per bin the β-strength distribution. Thanks to the unfolding code (see Sec. 6.2) we have obtained the β-feeding of ^{8}B into ^{8}Be, which is shown in Fig. 8.2.

From Eq. 1.22, the *ft*-value is proportional to the inverse of the β-strength distribution.

$$S_\beta(E_x) = \frac{I_\beta(E_x)}{f(Q_{EC} - E_x)T_{1/2}} = \frac{1}{f(Q_{EC} - E_x)t_{1/2}} \tag{8.1}$$

Experimentally, we can obtain the *ft*-value using the LOGFT.for code [nds] and including the percentage of β-feeding of each level to properly calculate the $t_{1/2}$. The *ft*-values are obtained in 20 keV bins. Fig. 8.3 shows the β-strength distribution obtained in the IS633 experiment.

The B_F of the decay has only contribution from the 2^+ doublet and this must be, due to the sum rule, equal to 2. The B_{GT} can be calculated, then, using

$$ft = \frac{K}{B_F + g_a^2 B_{GT}} \tag{8.2}$$

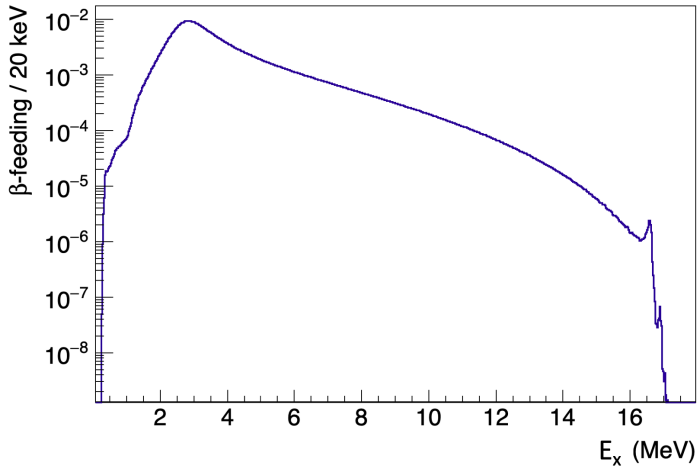

Figure 8.2: β-feeding distribution obtained of ^{8}B into ^{8}Be as a function of the excitation energy of ^{8}Be. Spectrum obtained with the unfolding code (see Sec. 6.2), normalized to 1.

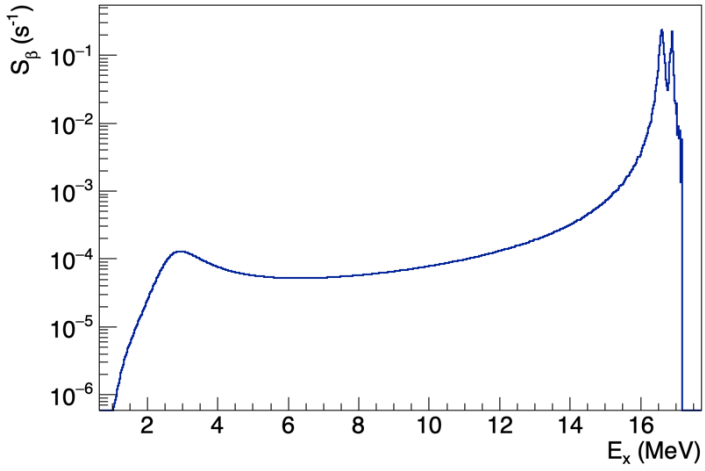

Figure 8.3: β-strength distribution obtained from the unfolded spectrum as a function of the excitation energy of ^{8}Be.

with $K = 6143.6(17)s$ [HT09], subtracting the B_F and dividing by the $g_a^2 = 1.6116(73)$ [YAA$^+$06] constant.

$$B_{GT} = \frac{KS_\beta - B_F}{g_a^2} \tag{8.3}$$

The integral of the β-strength when multiplying by K Fig. 8.3 is 3.26, which gives a B_{GT}=0.8(2)[2]. This value is model-independent. From the R-matrix analysis, the B_{GT} obtained of this decay comes mainly from the doublet and is equal to 1.55(28) from the holistic fit, 1.52(84) from the 2^+ doublet fit and 1.26(28) from the fit of the unfolded data with the constrain $\sum B_F$=2. The first two values differ from the result obtained from the β-feeding distribution and one of the reasons could be that the R-matrix results depend on the model used and the parameters are extremely correlated. Moreover, in these two fits the sum of the Fermi intensities is not equal to 2 ($\sum B_{F,hol}$=1.71(34) and $\sum B_{F,doub}$=1.8(1.1)). Then, if the B_{GT} is calculated subtracting the sum of the B_F result of the fits instead 2, the B_{GT} is 1.0(2) for the holistic fit and 0.9(2) for the doublet fit. The results still differ compared to the results of the R-Matrix. However, the B_{GT} obtained with the R-Matrix fit of the unfolded data with the constrain $\sum B_F$=2, namely $B_{GT} = 1.26(28)$, agrees well within the uncertainties with the $B_{GT} = 0.8(2)$ calculated from the integral of the β-strength distribution.

[2]The error has been estimated propagating errors on the main contribution of the integral, over 16 MeV. An accurate calculation is still to be done.

8.2 ISOSPIN MIXING OF THE 2^+ DOUBLET

As discussed in Sec. 1.2.3, the isospin mixing of the 2^+ doublet at 16.6 and 16.9 MeV of the ^{8}Be nucleus has been of particular interest since Barker promoted the use of the R-Matrix formalism to treat β-delayed particle decays and presented the treatment of the doublet [Bar69] [Bar75]. However, the mixing of these two states has been reviewed by von Brentano [vB96] through the analysis of $\alpha\alpha$ scattering data of the reaction of ^{4}He(α,α) measured by Hinterberger et al [HEvR$^+$78]. From $\alpha\alpha$ scattering, it was deduced that the two levels interfere with a background contribution in a way that depends on the measured scattering angle.

The degree of mixing between the two states that conform the 2^+ doublet at 16.6 and 16.9 MeV can be determined from the results of the R-Matrix analysis performed in this work. Due to the high statistics in the high-energy region and the quality of the fit achieved, this is the first experimental work that determines the isospin mixing of the two states from β-decay. Furthermore, the β-feeding of these two states addresses both the T=0 and T=1 component while the reaction studies mainly address the T=0. The results obtained with the holistic R-matrix analysis will be compared with the analysis focused on the 2^+ doublet (see Sec. 5.4.2).

As explained in Sec. 5.4.2, the isospin mixing parameters are the α and β that define the content of isospin 0 and 1 of each state of the doublet, and therefore, the parameters that multiply the matrix elements associated to isospin equal to 0, $M_{0,F}$ and $M_{0,GT}$, and isospin equal to 1, $M_{1,F}$ and $M_{1,GT}$, for Fermi and Gamow-Teller transitions. The relationship between the matrix elements of each state, the parameters α and β and the matrix elements of each isospin value are given in Eq. 5.12. Since the Gamow-Teller and Fermi strength are directly proportional to the square of their respective matrix elements, we can rewrite Eq. 5.12 as follows:

$$B_{16.6,F} = 2C\beta^2 \qquad B_{16.6,GT} = C'(\alpha M_{0,GT} + \beta M_{1,GT})^2 \tag{8.4}$$

$$B_{16.9,F} = 2C\alpha^2 \qquad B_{16.9,GT} = C'(\beta M_{0,GT} - \alpha M_{1,GT})^2 \tag{8.5}$$

To get rid of the C and C' constants, we will divide the equations to solve

for the ratio α^2/β^2. From the B_F, the relation is direct:

$$\frac{\alpha^2}{\beta^2} = \frac{B_{16.9,F}}{B_{16.6,F}} \tag{8.6}$$

From the B_{GT}, shell-model calculation of [War86] predicts that the matrix element $M_{1,GT}$ is negligible compared with the $M_{0,GT}$ and can be set to 0. For our study, we will consider also the possibility of $M_{0,GT}$ equal to 0, in order to check if the shell model prediction is correct. The expressions obtained for α^2/β^2 are:

$$\text{if } M_{1,GT} = 0 \rightarrow \frac{\alpha^2}{\beta^2} = \frac{B_{16.6,GT}}{B_{16.9,GT}} \tag{8.7}$$

$$\text{if } M_{0,GT} = 0 \rightarrow \frac{\alpha^2}{\beta^2} = \frac{B_{16.9,GT}}{B_{16.6,GT}} \tag{8.8}$$

Moreover, the α and β parameters can be also deduced from the width of the states. The observed width of a state λ in the Breit-Wigner approximation can be described as

$$\Gamma^0_\lambda = \frac{\sum_c 2P_c\gamma^2_{\lambda c}}{1 + \sum_c \gamma^2_{\lambda c}\frac{\partial S_c}{\partial E}|_{E=E_\lambda}} \tag{8.9}$$

where P_c is the penetration function, $\gamma^2_{\lambda c}$ the reduced width of the state λ and S_c is the shift function (explained in Sec. 5.4.1) for the c channel.

If Eq. 5.10 is rewritten as a function of the reduced widths, where for simplicity the sub-index c has been omitted as in our case there is only one breakup channel:

$$\gamma_{16.6} = \alpha\gamma_0 + \beta\gamma_1 \tag{8.10}$$

$$\gamma_{16.9} = \beta\gamma_0 - \alpha\gamma_1 \tag{8.11}$$

then, two assumptions are made. The first one is that the observed widths are purely T=0 due to the forbiddingness of the α-decay ($\Delta T = 1$), being the total decay width $\Gamma_0 = \Gamma_1 + \Gamma_2$. The second one is that the states are high above the α-decay threshold and therefore the denominator of Eq. 8.9 can be set equal to 1. This allows us to rewrite the reduced widths as

$$\gamma^2_{16.6} = \alpha^2\frac{\Gamma_0}{2P} \tag{8.12}$$

$$\gamma^2_{16.9} = \beta^2\frac{\Gamma_0}{2P} \tag{8.13}$$

Table 8.1: Results of the relation α^2/β^2 calculated from the Fermi, Gamow-Teller and widths of the 2^+ doublet for the holistic R-matrix analysis (first column), the fit focused on the doublet (second column) and the ratios obtained with the R-Matrix analysis of the unfolded data with the constrain $\sum B_F$=2.

α^2/β^2 **relation**	**Holistic**	$\mathbf{2^+}$ **doublet**	**Unfolded**
From B_F	1.72(64)	5(12)	0.902(64)
From B_{GT} with $M_{1,GT} = 0$	1.71(55)	3.4(5.0)	1.37(83)
From B_{GT} with $M_{0,GT} = 0$	0.58(31)	0.3(1.0)	0.729(72)
From Γ	1.150(11)	1.20(15)	1.08(59)

assuming the penetration function constant over the doublet. α and β can be written as:

$$\alpha^2 = \frac{\Gamma_{16.6}}{\Gamma_0} = \frac{\Gamma_{16.6}}{\Gamma_{16.6} + \Gamma_{16.9}} \tag{8.14}$$

$$\beta^2 = \frac{\Gamma_{16.9}}{\Gamma_0} = \frac{\Gamma_{16.9}}{\Gamma_{16.6} + \Gamma_{16.9}} \tag{8.15}$$

Before this experiment, no experimental information of the pure width and intensities of the 16.9 MeV state was available due to the interference with the 16.6 MeV state. With the results obtained in Sec. 5.5, the relationship between α and β is determined from Eq. 8.6, 8.7 and 8.14 and is summarized in Tab. 8.1.

The first consequence from the results is that the prediction of Warburton [War86] is proven experimentally for the first time, since when choosing $M_{1,GT} = 0$ the relation α^2/β^2 calculated from the B_{GT} is in good agreement with the calculations from the Fermi intensity and the width of the states. This also gives us the chance to restrict more the fit and improve the uncertainties of the parameters reducing the correlation between the other decay parameters as if $M_{1,GT} = 0$, the relation between the B_F and the B_{GT} of the two states can be rewritten as:

$$\frac{\alpha^2}{\beta^2} = \frac{B_{16.6,GT}}{B_{16.9,GT}} \tag{8.16}$$

Furthermore, the results indicate that the holistic fit is more accurate in the determination of the ratio than when fitting only the doublet region. The three are in good agreement within the errors in the same α^2/β^2 ratio. However, when fitting the doublet, the errors are larger and the results do not agree with

Table 8.2: Results of the isospin mixing coefficients α and β for the different R-Matrix fits.

Fit Model	α	β
Holistic fit	0.7314(24)	0.6819(24)
Doublet fit	0.738(31)	0.675(31)
Unfolded fit ($\sum B_F = 2$)	0.72(14)	0.69(13)

the ratio obtained form the widths. When calculating the ratios with the parameters obtained with the unfolded data and the constrain $\sum B_F{=}2$, the three values are in good agreement within the errors and also compatible with the results obtained in the holistic fit.

Besides the ratio, from the width of the states, one can obtain the individual α and β parameters. In the holistic case, $\alpha = 0.7314(24)$ and $\beta = 0.6819(24)$. In the study of the doublet, $\alpha = 0.738(31)$ and $\beta = 0.675(31)$. For the unfolded data, $\alpha = 0.72(14)$ and $\beta = 0.69(13)$. This allows us to conclude that the mixing of the two isospin states is almost equal. These results are summarized in Tab. 8.2.

8.3 PROTON-HALO STRUCTURE

It was already stated in Sec. 1.2.2 that ^{8}B is known to be the lightest proton-halo nucleus from the results of elastic and inelastic scattering [KaAIA^{+}18] [CGMA^{+}02] and from the measurement of reaction cross section [AMQL^{+}09], but no indication has been obtained from the β-decay. This can be explained due to the challenge that represents detecting a particle of such a low energy and with such a low branching ratio, in this case, the proton.

In general, a crucial feature of halo states is their intrinsic clustering which allows to factorize the wave-function into a halo part and a core part. For a β-decay, the wave-function can be written as:

$$\Psi_{\beta}(|c\rangle|h\rangle) = (\Psi_{\beta}|c\rangle)|h\rangle + |c\rangle(\Psi_{\beta}|h\rangle) \tag{8.17}$$

where $|c\rangle$ and $|h\rangle$ are the core and halo terms respectively [BFF^{+}13].

For the ^{8}B case, the β-decay to the state 1^{+} T=1 at 17.640 MeV of the ^{8}Be nucleus is known to proceed mainly by proton emission [Tea04]. This state is situated 385 keV above the proton threshold and from Eq. 8.17 the matrix element of the transition can be estimated to be the same as for the ground state decay of ^{7}Be into the ground state of ^{7}Li, as both are electron capture decays, and by scaling the half-life of ^{7}Be, the branching ratio of the βp transition of the ^{8}B can be estimated to be around 2.3×10^{-8}. This branching ratio is supported by three cluster calculations [GSZ00].

Experimentally, there is no firm estimation of the aforementioned branching ratio. Prior to this study, it was set an experimental upper limit of the βp decay of 2.6×10^{-5} at a 95% confidence level [BFF^{+}13]. From the results analysed in this thesis, this upper limit is reduced by one order of magnitude, being set at 2.5×10^{-6} at a 99.9% confidence level, as the proton peak from the simulation stands above the background level as much as 3σ (see Sec. 7.3).

One could suggest to look for a lower upper limit by decreasing the amount of protons simulated. However, with less than 2500 simulated protons over 4π, the peak produced cannot be fitted and we have decided to not include it. To improve our results for the upper limit of the proton emission branching ratio, a dedicated experiment should be carried out. We already tried to perform such a measurement focused on the low-energy region, however it was not suc-

cessful because the setup configuration did not allowed to perform an accurate anti-coincidence analysis. Nevertheless, from the data taken with focus on the high-energy part, we have been able to extract very valuable information on the low-energy region as well. Notice the relevance of improving both regions with only one experiment.

Summarizing this section, we have improved the experimental upper limit of the branching ratio of the rare βp decay of ^{8}B by one order of magnitude with a higher confidence level than the previous value.

8.4 SUMMARY AND CONCLUDING REMARKS

We have performed a β-decay α-spectroscopy experiment at the ISOLDE@CERN facility. The β^+/EC-decay of ^{8}B has been studied to gain deeper understanding of the structure of ^{8}Be. The aim of the experiment was to observe, for the first time with enough statistics, the 16.9 MeV state with the purpose of solving the isospin mixing of the 2^+ doublet in ^{8}Be detecting α-α coincidences of the breakup that follows the β-decay of ^{8}B. Prior to this study, only 5 counts were assigned to the 16.9 MeV level in β-decay [Kea11]. By the decay process both T=0 and T=1 components are addressed while in reaction studies only one is addressed. Moreover, from the data obtained it can be set an upper limit on the branching ratio of the rare βp decay [BFF$^+$13], which is a proof of the proton-halo structure of ^{8}B.

The setup consisted of a compact set of four ΔE-E Si-telescopes, being the ΔE detectors DSSD of 40 and 60 μm backed by Si-PADs acting as E detector. During the experiment, the average of α-particles detected after the breakup of the ^{8}Be was 25.000 counts/s.

Furthermore, we have performed a detailed characterisation of the DSSD's used as ΔE detector using GEANT4 simulations, achieving a reproduction of the calibration α-source that has allowed us to get an accurate response function of each detector. With the response function, we have implemented and run an unfolding iterative code based on the Richardson-Lucy algorithm that has been used to deconvolute the experimental spectrum to obtain the pure β-feeding to the ^{8}Be nucleus.

The β-feeding is not only interesting by itself, it has been used as the input of the GEANT4 simulation in the search for the β-delayed proton. The simulations have been compared with the *singles* spectrum obtained experimentally and once validated have been used to determine the upper limit of the branching ratio of the β-delayed proton emission.

The conclusions of this work can be listed as follows:

- The IS633 experiment provides new and meaningful information on the β-decay of ^{8}B compared with previous experiments. With the statistics obtained it has been possible to identify and differentiate with enough statistics the two states that conform the 2^+ doublet at 16.6 and 16.9

MeV.

- As analysis technique, we have implemented an unfolding code that has allowed to obtain the pure β-feeding of ^{8}B into the ^{8}Be nucleus. The code has been tested over different simulated distributions and has demonstrated to be very useful, for example, to obtain the composition of an α-source.

- The accurate response functions obtained with the characterization of the DSSDs used open the door to improve the neutrino spectrum at low energies. In this work, as the experiment has other purposes, the calibration at low energies is not accurate enough to proceed with this analysis.

- From the β-feeding spectrum obtained with the unfolding code, it has been obtained the β-strength distribution and the total B_{GT} has been determined to be 0.8(2) which is in good agreement within the uncertainties with the results of R-Matrix analysis of the unfolded data with the constrain $\sum$B$_F$=2, B$_{GT}$=1.26(28).

- From the α-α coincidence analysis, an improvement on the half-life of the nucleus has been achieved, reducing the uncertainty of the last published value [ASL74] by a factor of 3.1. The half-life has been obtained from three independently analysed measurements and once it is weighted with the prior value, the result is 771.95(95) ms.

- From the R-Matrix analysis of the α-α coincidence spectrum, the isospin mixing of the 2^+ doublet of ^{8}Be has been solved for the first time. The mixing coefficients α and β are assigned to the T=0 and T=1 isospin states and have been determined form the width of the states to be $\alpha = 0.7314(24)$ and $\beta = 0.6819(24)$ for the holistic fit and $\alpha = 0.72(14)$ and $\beta = 0.69(13)$ for the fit of the unfolded data with $\sum$B$_F$=2. These results demonstrate that the two states are completely mixed in isospin.

- Moreover, from the R-Matrix analysis, it has been confirmed the shell model prediction of M$_{1,GT}$=0, since when the ratio α^2/β^2 is calculated

using this condition gives compatible results with when it is calculated with the B_F, B_{GT} and the widths of the states.

- Finally, we have analysed the data of the experiment to look for the rare βp emission with no success due to the extremely low branching ratio of this decay ($> 2.3\times10^{-8}$ [BFF$^+$13]) and that it was not the main purpose of the experiment. However, we have been able to determine an experimental upper limit of the branching ratio of 2.5×10^{-6} at a 99.9% confidence level (3σ).

Summaries

9

9.1 EXECUTIVE SUMMARY

9.1.1 Motivation and objectives

The β-decay of the proton halo nucleus ^{8}B into ^{8}Be has been studied in detail several times in the last decade. In the framework of this thesis, we have performed an experiment in 2016 at ISOLDE@CERN with the aim of determining the β-strength for decays to the highly excited states of ^{8}Be. Of particular interest is the population in the decay of the 2^{+} doublet at 16.6 and 16.9 MeV. Reaction studies indicated that the nature of these two states is of full mixture of isospin T=0 and T=1. The β-decay process is the only that allows to simultaneously address the two isospin components of the states and has not been measured before. The second objective is to determine the branching ratio of the so far unobserved electron-capture delayed-proton-emission branch expected to proceed via the 17.6 MeV state.

The objectives of this thesis are not only to determine the isospin mixing parameters of the 2^{+} doublet and determine the branching ratio of the rare βp branch at 17.6 MeV. In addition, a more accurate determination of the half-life has been done. In order to obtain reliable results, we have characterized the set-up used in the experiment using Monte Carlo simulations with the GEANT4 tool and we have implemented an innovative unfolding code to obtain the β-feeding of ^{8}B nucleus into ^{8}Be.

9.1.2 Physics background and state-of-the-art

The β^+/EC-decay of ^{8}B is one of the steps in the hydrogen-burning processes that takes place in the sun and, moreover, this decay is the main source of high energy solar neutrinos, above 2 MeV.

Apart from the astrophysical interest, the decay of ^{8}B gives access to the nuclear structure of ^{8}Be. The excited states of ^{8}Be accessible via allowed β^+/EC-transitions are unbound and due to their width the spectrum is dominated by a broad resonance at 3 MeV, which has been, for many years, subject of R-matrix analysis. The two states at 16.6 and 16.9 MeV form a 2^+ doublet being the only case in which one can expect more than a few percent of isospin mixing. Moreover, the ^{8}Be cluster structure made that its 2^+ resonant states break into two α.

However, from the nuclear structure perspective ^{8}B is very interesting. The ^{8}B nucleus is the only nucleus known for exhibiting a proton-halo configuration in its ground state. The β^+/EC-decay to the 17.6 MeV state is expected to be enhanced by the proton-halo structure of ^{8}B and is known from reaction studies to decay mainly via proton emission.

9.1.3 Experimental procedure and data analysis

The detection set-up consisted in a "diamond" configuration of four Si-telescopes. The telescopes were composed by a thin ΔE-Double-sided Silicon Strip Detector (DSSD) with 16 strips on each side, backed by a thicker Si-detector. An additional DSSD of 1000 μm thickness was placed at the bottom of the set-up and it was mainly used as a β monitor. Two different front detector thicknesses were used in the telescopes; the thicker ΔE-DSSD of 60 μm assured the full detection of the highest energy of the α emitted in the breakup of the ^{8}Be. The thinner ΔE-DSSD of 40 μm were used to test if the set-up could be useful for the second goal of the experiment: the detection of the delayed-proton emission from the 17.6 MeV populated via EC. The observation of this branch, estimated to be $\sim 10^{-8}$ will be an evidence of the p-halo structure of the ^{8}B nucleus, where accurate knowledge of the β-response and low background is mandatory.

From the detection of the α particles of the break-up of the ^{8}Be nucleus, the α-α coincidence spectrum is obtained and corrected for different experimental effects, namely the recoil-energy, the dead layers of the detectors and the energy separation of the 2α. To correct for these effects, an accurate Monte Carlo simulation have been done using the GEANT4 package. The DSSDs have been characterized and as part of this work, the response function of each detector has been obtained, being a crucial information for the posterior R-Matrix analysis and unfolding procedure.

For the study of the β-delayed proton branch, an anti-coincidence analysis has been performed. To determine the upper limit of the branching ratio, first a simulation of the β-decay of ^{8}B was performed, validating it with the *singles* spectrum obtained directly from what was measured (without analysis). Once the simulations are validated, a proton peak is simulated over 4π to determine the limit where it would be seen over the experimental background.

Furthermore, for the development of the unfolding code, a systematic study has been done, checking the goodness of the solution obtained comparing the results with simulations and with experimental data.

9.1.4 Results

The results derived from this thesis are:

From the α-α coincidence analysis

- The half-life of the ^{8}B nucleus has been determined from three independently analysed measurement reducing by a factor of 3.1 the uncertainty of the last published value.

- The isospin mixing parameters have been determined using an R-Matrix analysis, being $\alpha = 0.7314(24)$ and $\beta = 0.6819(24)$ the mixing coefficients for the holistic fit and $\alpha = 0.72(14)$ and $\beta = 0.69(13)$ for the fit of the unfolded data with $\sum B_F{=}2$, confirming that the isospin mixing between the two states is complete according to shell-model calculations.

From the unfolding procedure

- We have implemented the Richardson-Lucy unfolding algorithm in a C++ program. It has been tested over different simulated distributions and has demonstrated to be meaningful, for example, for obtaining the composition of an α-source.

- From the β-feeding spectrum obtained with the unfolding code, the β-strength distribution has been obtained and the B_{GT}-value is determined to $B_{GT} = 0.8(2)$ which is in very good agreement within the uncertainties with the results of R-Matrix analysis of the unfolded data with the constrain $\sum B_F=2$, $B_{GT}=1.26(28)$.

- Using the β-feeding spectrum as a simulation input, the GEANT4 simulations of the set-up have been validated comparing the result of the simulations with the *singles* experimental α-spectrum.

From the anti-coincidence analysis

- With the simulations validated, we have determined an experimental upper limit of the branching ratio of the rare βp-emission to 2.5×10^{-6} within a confidence level of 99.9% (3σ).

9.2 BREVE RESUMEN

9.2.1 Motivación y objetivos

La desintegración β del núcleo halo de protón ^{8}B en ^{8}Be se ha estudiado en detalle en diversos experimentos durante las últimas décadas. En el marco de esta tesis, realizamos un experimento en 2016 en ISOLDE@CERN con el objetivo de determinar la intensidad β para las desintegraciones a los estados excitados del ^{8}Be. De particular interés es el doblete 2^{+} a 16.6 y 16.9 MeV, el cual se supone, basado en estudios de reacciones, que presenta una mezcla total de isospín T=0 y T=1. Siendo éste el único caso conocido con una mezcla máxima de isospín. La desintegración β es el único mecanismo por el cual se pueden estudiar ambos isospines de los estados del doblete y, hasta ahora, no ha sido medida. El segundo objetivo es determinar la razón de ramificación de la emisión de protones retardada poblada por captura electrónica, que no había sido observada hasta ahora. Dicho canal de desintegración se espera que ocurra a través del estado de 17.6 MeV y la estimación de su razón de ramificación está basada en la estructura de halo del ^{8}B.

Los objetivos de esta tesis son fundamentalmente determinar los parámetros de mezcla de isospin del doblete 2^{+} y determinar o establecer una cota superior experimental a la razón de ramificación de la desintegración βp a 17.6 MeV, no observada previamente. Además, se ha determinado de forma más precisa la vida media del núcleo ^{8}B. Para alcanzar estos resultados con la máxima precisión, hemos caracterizado de forma precisa los detectores usados en el experimento utilizando simulaciones Monte Carlo con la herramienta GEANT4 y se ha implementado un código de desconvolución que se ha usado para obtener la población β del núcleo ^{8}B en ^{8}Be.

9.2.2 Contexto físico y "estado del arte"

La desintegración β^{+}/EC del ^{8}B es uno de los pasos en el proceso de combustión de hidrógeno que tiene lugar en el Sol y, además, esta desintegración es la principal fuente de neutrinos solares de alta energía, por encima de 2 MeV.

Además de su interés astrofísico, la desintegración β^{+} del ^{8}B da acceso a la estructura nuclear del ^{8}Be. Éste tiene un continuo de estados 2^{+} debido a una amplia resonancia a 3 MeV, que ha sido, durante muchos años, objeto de

análisis con *Matriz R*. Los dos estados a 16.6 y 16.9 MeV forman un doblete 2^+, siendo el único caso en el que uno puede esperar más que un pequeño porcentaje de mezcla de isospín. El núcleo ^{8}Be presenta una estructura de clúster α-α que hace que sus estados excitados resonantes 2^+ se rompan con la emisión de dos partículas α.

Desde la perspectiva de su estructura nuclear, el núcleo ^{8}B también es interesante: es el único núcleo conocido cuya configuración de halo de protón en su estado fundamental está bien establecida. Se espera que la desintegración β al estado de 17.6 MeV se vea incrementada por la estructura de halo de protón del ^{8}B. Este estado se sabe, por estudios de reacciones, que decae principalmente a través de la emisión de un protón.

9.2.3 Medida experimental y procesado de datos

El montaje experimental consistió en una configuración en forma de "diamante" de cuatro telescopios de detectores de Si. Los telescopios estaban compuestos por un detector fino doblemente segmentado ΔE (DSSD) con 16 bandas a cada lado. Detrás, un detector de Si más grueso. Se colocó un DSSD adicional en la parte inferior con un grosor de 1000 μm y con la finalidad principal de ser detector β. Se utilizaron dos espesores diferentes para el detector frontal de los telescopios; dos ΔE-DSSD más gruesos de 60 μm para asegurar la detección completa de las α más energéticas emitidas en la ruptura del ^{8}Be y dos ΔE-DSSD de 40 μm que se optimizaron para el segundo objetivo del experimento: la detección de la emisión retardada de protones del estado 17.6 MeV poblado a través de EC y evidencia de la estructura halo de protón del núcleo ^{8}B, donde la respuesta precisa frente partículas β y el bajo fondo son necesarios.

A partir de la detección de las α emitidas en la rotura del núcleo hijo ^{8}Be, se obtiene y corrige el espectro de coincidencia α-α para diferentes efectos experimentales, como por ejemplo, la energía de retroceso del núcleo hijo, las capas muertas de los detectores utilizados y la diferencia de energía de las 2α frente al estado fundamental del ^{8}Be. Para corregir estos efectos, se ha realizado una simulación Monte Carlo lo más fidedigna posible utilizando el paquete GEANT4. Los DSSDs se han caracterizado y, a partir de este trabajo, se ha obtenido la función de respuesta de cada detector, siendo una información crucial para el análisis posterior de *Matriz R* y el procedimiento de desconvolución.

Para el estudio de la desintegración de protones retardados, se realizó un análisis de anti-coincidencia, cuyo objetivo era la determinación de una cota experimental superior de la razón de ramificación. Primero, se ha realizado una simulación de la desintegración β del ^{8}B, validando con el espectro *singles* que se midió sin análisis previo. Una vez validadas las simulaciones, se ha simulado la emisión en 4π de un pico de protones para determinar el límite en el cual el pico sería visible sobre el fondo experimental.

Para el desarrollo del código de desconvolución se ha realizado un estudio sistemático, verificando la bondad de la solución obtenida comparando los resultados con simulaciones y con datos experimentales.

9.2.4 Resultados

Los resultados que se derivan de esta tesis son:

Del análisis de coincidencia α-α

- La vida media del núcleo ^{8}B se ha determinado a partir de tres medidas analizadas independientemente, reduciendo en un factor 3.1 la incertidumbre del último valor publicado.

- Los parámetros de mezcla de isospin se han determinado usando un análisis de *Matriz R*, siendo $\alpha = 0.7314(24)$ y $\beta = 0.6819(24)$ los coeficientes de mezcla para el ajuste holístico y $\alpha = 0.72(14)$ y $\beta = 0.69(13)$ para el ajuste con los datos desconvolucionados fijando $\sum B_F = 2$, confirmando que la mezcla de isospin entre los dos estados es completa de acuerdo con el cálculo de modelo de capas.

Del procedimiento de desconvolución

- Hemos implementado el algoritmo de Richardson-Lucy en C++. Ha sido probado en diferentes distribuciones simuladas y ha demostrado ser significativo, por ejemplo, para obtener la composición de una fuente α.

- Del espectro de población β obtenido con el código de desconvolución, se ha obtenido la distribución de intensidad β y se ha determinado que el valor de B_{GT} es 0.8(2), en buena concordancia dentro del error con los resultados del ajuste de *Matriz R* de los datos desconvolucionados (B_{GT}=1.26(28)). La contribución a B_{GT} viene dominada por los estados del doblete 2^+, ya que al dividir por el espacio fásico estos dominan el espectro.

- Usando el espectro de población β, las simulaciones GEANT4 del montaje experimental se han validado comparando el resultado de las simulaciones con el espectro experimental *singles*.

Del análisis de anti-coincidencia

- Con las simulaciones validadas, se ha determinado una cota superior experimental para la razón de ramificación para el canal exótico de emisión de βp de 2.5×10^{-6} con un nivel de confianza de 99.9% (3σ).

Bibliography

[AAA+03] S. Agostinelli, J. Allison, K. Amako, J. Apostolakis, H. Araujo, P.. Arce, M. Asai, D. Axen, S. Banerjee, G. Barrand, F. Behner, L. Bellagamba, J. Boudreau, L. Broglia, A. Brunengo, H. Burkhardt, S. Chauvie, J. Chuma, R. Chytracek, G. Cooperman, G. Cosmo, P. Degtyarenko, A. Dell'Acqua, G. Depaola, D. Dietrich, R. Enami, A. Feliciello, C. ferguson, H. Fesefeldt, G. Folger, F. Foppiano, A. Forti, S. Garelli, S. Giani, R. Giannitrapani, D. Gibin, J.J. Gómez-Cadenas, I. González, G. Gracia-Abril, G. Greeniaus, W. Greiner, V. Grichine, A. Grossheim, S. Guatelli, P. Gumplinger, R. Hamatsu, K. Hashimoto, H. Hasui, A. Heikkinen, A. Howard, V. Ivanchenko, A. Johson, F.W. Jones, J. Kallenbach, N. Kanaya, M. Kawabata, Y. Kawabata, M. Kawaguti, S. Kelner, P. Kent, A. Kimura, T. Kodama, R. Kokoulin, M. Kossov, H. Kurashige, E. lamanna, T. Lampén, V. Lara, V. Lefebure, F. Lei, M. Liendl, W. Lockman, F. Longo, S. Magni, M. Maire, E. Medernach, K. Minamimoto, P. Mora de Freitas, Y. Morita, K. Murakami, M. Nagamatu, R. Nartallo, P. Nieminen, T. Nishimura, K. Ohtsubo, M. Okamura, S. O'Neale, Y. Oohata, K. Paech, J. Perl, A. Pfeiffer, M.G. Pia, F. Ranjard, A. Rybin, S. Sadilow, E. Di Salvo, G. Santin, T. Sasaki, N. Savvas, Y. Sawada, S. Scherer ans S. Sei, V. Sirotenko, D. Smith, N. Starkov, H. Stoecker, J. Sulkimo, M. Takahata, S. Tanaka, E. Tcherniaev, E. Safai Tehrani, M. Tropeano, P. Truscott, H. Uno, L. Urban, P. Urban, M. Verderi, A-Walkden, W. Wander, H. We-

ber, J.P. Wellisch, T. Wenaus, D.C. Williams, D. Wright, T. Yamada, H. Yoshida, and D. Zschiesche. Geant4 - a simulation toolkit. *Nuclear Instruments and Methods in Physics Research A*, 506:250–303, 2003.

[AMQL+09] E.F. Aguilera, E. Martinez-Quiroz, D. Lizcano, A. Gómez-Camacho, J.J. Kolata, L.O. Lamm, V. Guimarães, R. Lichtenthäler, O. Camargo, F.D. Becchetti, H. Jiang, P.A. DeYoung, P.J. Mears, and T.L Belyaeva. Reaction cross sections for ^{8}B , ^{7}Be and ^{6}Li + ^{58}Ni near the Coulomb barrier: Proton-halo effects. *Physical Review C*, 79(021601), 2009.

[ASL74] F. Ajzenberg-Selove and T. Lauritsen. Energy levels of light nuclei A=5-10. *Nucelar Physics A*, 277(1):1–243, 1974.

[Aup04] J. Aupiais. Deconvolution of alpha liquid scintillation spectra for quantitative analysis of actinide elements in water samples. *Radiochimica acta*, 92:125–132, 2004.

[aus] Ausalib package.

[Bar66] F.C. Barker. Intermediate coupling shell-model calculation for light nuclei. *Nuclear physics*, 83(2):418–448, 1966.

[Bar69] F.C. Barker. 2^{+} states of ^{8}Be. *Australian Journal of Physics*, 22(3):293 – 316, 1969.

[Bar75] F.C. Barker. Isospin mixing in nuclear levels. *Physical Review Letters*, 35(9):613–614, 1975.

[BAS06] M. Battacharya, E.G. Adelberger, and H.E. Swanson. Precise study of the final-state continua in ^{8}Li and ^{8}B decays. *Physical Review C*, 73(055802), 2006.

[BCDJR85] JN Bahcall, BT Cleveland, R Davis Jr, and JKi Rowley. Chlorine and gallium solar neutrino experiments. *The Astrophysical Journal*, 292:L79–L82, 1985.

[BCE66] C.P. Browne, W.D. Callender, and J.R. Erskine. Interference between the 16.62 and 16.92 MeV levels in ^{8}Be. *Physics letters*, 23(6):371–373, 1966.

[BCF+16] M.J.G. Borge, J. Cederkall, P. Díaz Fernández, L.M. Fraile, H.O.U. Fynbo, A. Heinz, J.H. Jensen, H.T. Johansson, B. Jonson, O.S. Kirsebom, R. Lica, S. Lindberg, I. Marroquin, M. Munch, E. Nacher, T. Nilsson, A. Perea, J. Refsgaard, K. Riisager, J. Snall, and O. Tengblad. Electron capture of ^{8}B into highly excited states in ^{8}Be. Proposal to the ISOLDE and Neutron Time-of-Flight Commitee CERN-INTC 2016-052, European organization for nuclear research, 2016.

[BFF+13] M.J.G. Borge, L.M. Fraile, H.O.U. Fynbo, B. Jonson, O. S. Kirsebom, T. Nilsson, G. Nyman, G. Possnert, K. Riisager, and O. Tengblad. Rare βp decays in light nuclei. *Journal of physics G: nuclear and particle physics*, 40(035109), 2013.

[BM69] A. Bohr and B. Mottelson. *Nuclear Structure*, volume 1. W.A. Benjamin inc., 1969.

[BSD+18] J. Ballof, C. Seiffert, Ch.E. Düllmann, M. Delonca, M. Gai, A. Gottberg, T. Kröll, R. Lica, M.Madurga Flores, Y.Martínez Palenzuela, T. Mendoca, J.P. Ramos, S. Rothe, T. Stora, O. Tengblad, and F. Wienholtz. Radioactive boron beams produced by isotope online mass separation at CERN-ISOLDE. *The European Physical Journal A*, 55(5):65, 2018.

[BTdB92] C.J. Bland, J. Truffy, and T. de Bruyne. Deconvolution of alpha-particle spectra to obtain plutonium isotopic ratios. *International journal of Radiation Applications and instrumentatios. Part A. Applied Radiation and Isotopes*, 43(1/2):201–209, 1992.

[CGMA+02] D. Cortina-Gil, K. Markenroth, F. Attallah, T. Baumann, J. Benlliure, M.J.G. Borge, L.V. Chulkov, U. Datta Pramanik, J. Fernandez-Vázquez, C. Forssén, L.M. Fraile, H. Geissel, J. Gerl, F. Hammache, K. Itahashi, R. Janik, B. Jonson, S. Karlsson, H. Lenske, S. Mandal, M. Meister, X. Mocko, G. Münzenberg, T. Ohtsubo, A. Ozawa, Y. Parfenova ans V. Pribora, K. Riisager, H. Scheit, R. Schneider, K. Schmidt, G. Schrieder, H. Simon, B. Sitar, A. Stolz, P. Strmen, K. Sümmerer, I. Szarka, S. Wan, H. Weick, and M. Zhukov. Experimental evidences for the ^{8}B ground state configuration. *Physics Letters B*, 549:36–41, 2002.

[D'A95] G. D'Agostini. A multidimensional unfolding method based on Bayes' theorem. *Nuclear Instruments and Methods in Physics Research A*, 362:487–498, 1995.

[DJHH68] Raymond Davis Jr, Don S Harmer, and Kenneth C Hoffman. Search for neutrinos from the sun. *Physical Review Letters*, 20(21):1205, 1968.

[DLR77] Arthur P Dempster, Nan M Laird, and Donald B Rubin. Maximum likelihood from incomplete data via the EM algorithm. *Journal of the Royal Statistical Society: Series B (Methodological)*, 39(1):1–22, 1977.

[FC60] B.J. Farmer and C.M. Class. Alpha spectra from the decays of ^{8}Li and ^{8}B. *Nuclear physics*, 15:626–635, 1960.

[Fer34] Enrico Fermi. An attempt of a theory of beta radiation. 1. *Z. phys*, 88(161):19, 1934.

[Fre07] M. Freer. The clustered nucleus-cluster structures in stable and unstable nuclei. *Reports on Progress in Physics*, 70(12):2149, 2007.

[Gad18] A. Gad. An experimental study of ^{8}B beta decay. Master's thesis, Department of Physics and Astronomy, Aarhus University, June 2018.

[GFT+14] L. Grassi, J. Forneris, D. Torressi, L. Acosta, A. Di Pietro, P. Figueroa, M. Fischella, V. Grilj, M. Jakšić, M. Lattuada, T. Mijatović, M. Milin, L. Prepolec, N. Skukan, N. Soić, V. Tokić, and M. Uroić. Study of the inter-strip gap effects on the response of double sided silicon strip detectors using proton micro-beams. *Nuclear Instruments and Methods in Physics Research A*, 767:99–111, 2014.

[Gil54] F.C. Gilbert. Range distribution of alpha particles following the decays of ^{8}Li and ^{8}B. *Physical Review*, 93(3):499–501, 1954.

[GM48] Maria Goeppert-Mayer. On closed shells in nuclei. *Phys. Rev*, 74(1):235–239, 1948.

[GSZ00] L.V. Grigorenko, N.B. Shul'gina, and M.V. Zhukov. Three-cluster states in the spectrum of ^{8}Be: (1)structure and β-decay of ^{8}B to 16.6 MeV state. *Nuclear Physics A*, 665:105–121, 2000.

[HEvR+78] F. Hinterberger, P.D. Eversheim, P. von Rossen, B. Schüller, R. Schönhagen, M. Thenée, R. Görgen, T. Braml, and H.J. Hartmann. The α+α to ^{8}Be double reasonance at the 16.6 and 16.9 MeV levels. *Nuclear Physics A*, 299:397–411, 1978.

[HT09] John C Hardy and IS Towner. Superallowed 0+ - 0+ nuclear β decays: A new survey with precision tests of the conserved vector current hypothesis and the standard model. *Physical Review C*, 79(5):055502, 2009.

[Hyl10] S. Hyldegaard. *Beta-decay studies of ^{8}B and ^{12}C.* PhD thesis, Department of Physics and Astronomy, Aarhus University, 2010.

[Jon95] B. Jonson. Halo nuclei and other exotics. *Nuclear Physics, A*, 583:733–746, 1995.

[KaAIA+18] G.A. Korolev, A.V. Dobrovolsky anbd A.G. Inglessi, G.D. Alkhazov, P. Egelhof, A. Estradé, I. Dillmann, F. Farinon, H. Geissel, S. Ilieva, Y. Ke, A.V. Khanzadeev, O.A. Kiselev, J. Kurcewicz, X.C. Le, Yu.A. Litvinov, G.E. Petrov, A. Prochazka, C. Scheidenberger, L.O. Sergeev, H. Simon, M. Takechi, S. Tang, V. Volkov, A.A. Vorobyov, H. Weick, and V.I. Yatsoura. Halo structure of ^{8}B determined from intermediate energy proton elastic scattering in inverse kinematics. *Physics Letters B*, 780:200–204, 2018.

[Kea11] O Kirsebom and et al. Precise and accurate determination of ^{8}B decay spectrum. *Phys. Rev. C*, 83(6):065802–065822, 2011.

[Kir10] O. S. Kirsebom. *^{8}B neutrinos and ^{12}C Resonances.* PhD thesis, Department of Physics and Astronomy, Aarhus University, Denmark, 2010.

[Kno79] Glenn F Knoll. Radiation detection and measurement(book). *New York, John Wiley and Sons, Inc., 1979. 831 p*, 1979.

[LCD+97] J. Lettry, R. Catherall, P. Drumm, P. Van Duppen, A.H.M. Evensen, G.J. Focker, A. Jokinen, O.C. Jonsson, E. Kugler, H. Ravn, and ISOLDE Collaboration. Pulse shape of the ISOLDE radioactive ion beams. *Nuclear Instruments and Methods in Physics Research B*, 126:130–134, 1997.

[Lic17] Răzvan Lică. *Development of the ISOLDE Decay Station and γ spectroscopic studies of exotic nuclei near the N=20 "Island of Inversion"*. PhD thesis, University "Politehnica" of Bucarest, Faculty of Applied Sciences "Horia Hulubei" National Institute for Research and Development in Physics and Nuclear Engineering, 2017.

[LT58] A.M. Lane and R.G. Thomas. R-matrix theory of nuclear reactions. *Reviews of Modern physics*, 30(2):257 – 353, 1958.

[Luc74] L. B. Lucy. An iterative technique for the rectification of observed distributions. *The Astronomical Journal*, 79(6):745, 1974.

[MKR] M. Munch, O. S. Kirsebom, and J. Refsgaard. Open r-matrix.

[MPRS64] E. Matt, H. Pfander, H. Rieseberg, and V. Soergel. Beta decay from ^{8}B to the 16.67 MeV level in ^{8}Be. *Physics Letters*, 9(2):174–175, 1964.

[MUH+14] T. Myo, A. Umeya, K. Horii, H. Toki, and K. Ikeda. Shell and alpha cluster structures in ^{8}Be with tensor-optimized shell model. *Progress of Theoretical and Experimental Physics*, 33, 2014.

[nds] International atomic energy agency: Nuclear data services.

[PeaPDG16] C. Patrignani and et al. (Particle Data Group). Review of particle physics. *Chinese Physics C*, 40(10):100001, 2016.

[PPST12] R. Pöllänen, K. Peräjärvi, T. Siiskonen, and J. Turunen. High-resolution alpha spectrometry at ambient air pressure - Towards new applications. *Nuclear Instruments and Methods in Physics Research A*, 694:173–178, 2012.

[RFHJ15] K. Riisager, H.O.U. Fynbo, S. Hyldegaard, and A.S. Jensen. Broad resonances and beta-decay. *Nuclear Physics A*, 940:119–137, 2015.

[Ric72] W. H. Richardson. Bayesian-based iterative method of image restoration. *Jounal of Optical society of America*, 62(1):55–59, 1972.

[roo] Root data analysis framework.

[RSP80] F Reines, HW Sobel, and E Pasierb. Evidence for neutrino instability. *Physical Review Letters*, 45(16):1307, 1980.

[Tan90] Isao Tanihata. Neutron halos and exotic modes. *Nuclear Physics, A*, 520, 1990.

[TBF+04] O. Tengblad, U.C. Bergmann, L.M. Fraile, H.O.U. Fynbo, and S. Walsh. Novel thin window design for a large-area silicon strip detector. *Nuclear Instruments and Methods in Physics Research A*, 525:458–464, 2004.

[TCO07] José Luis Taín and Daniel Cano-Ott. Algorithms for the analysis of β-decay total absorption spectra. *Nuclear Instruments and Methods in Physics Research Section A: Accelerators, Spectrometers, Detectors and Associated Equipment*, 571(3):728–738, 2007.

[Tea04] D.R. Tilley and et al. Energy levels of A = 8, 9, 10. *Nuclear Physics A*, (745):155 – 362, 2004.

[THH+85] I Tanihata, H Hamagaki, Oe Hashimoto, Y Shida, N Yoshikawa, K Sugimoto, O Yamakawa, T Kobayashi, and N Takahashi. Measurements of interaction cross sections and nuclear radii in the light p-shell region. *Physical Review Letters*, 55(24):2676, 1985.

[vB96] Peter von Brentano. On the mixing of two bound and unbound levels: Energy repulsion and width attraction. *Physics Reports*, (264):57–66, 1996.

[VMC+96] L. León Vintró, P.I. Mitchell, O.M. Condren, M. Moran, J. Vives i Batlle, and J.A. Sánchez-Cabeza. Determination of the ^{240}Pu/^{239}Pu atom ratio in low activity environmental samples by alpha spectrometry and spectral deconvolution. *Nuclear Instruments and Methods in Physics Research A*, 369:597–602, 1996.

[VSK85] Y. Vardi, L.A. Shepp, and L. Kaufman. A statistical model for positron emission tomography. *Journal of the American Statistical Association*, 80(389):8–20, 1985.

[War86] E.K. Warburton. R-matrix analysis of the $\beta^{\pm}$-delayed alpha spectra from the decay of ^{8}Li and ^{8}B. *Physical Review C*, 33(1):303–313, 1986.

[WAW+12] Meng Wang, G Audi, AH Wapstra, FG Kondev, M MacCormick, X Xu, and B Pfeiffer. The ame2012 atomic mass evaluation. *Chinese Physics C*, 36(12):1603, 2012.

[Wea95] R.E. Warner and et al. Evidence for a proton halo in ^{8}B: Enhanced total reactions cross section at 20 to 60 MeV/nucleon. *Phys. Rev. C*, 52(3):1160–1170, 1995.

[Whe41] J.A. Wheeler. The alpha-particle model and the properties of the nucleus Be 8. *Physical Review*, 59(1):27, 1941.

[Won99] Samuel S.M. Wong. *Introductory Nuclear Physics*. Wiley-VCH; 2 edition, 1999.

[YAA+06] Wei-Ming Yao, CD Amsler, David M Asner, RM Bamett, J Beringer, PR Burchat, CD Carone, C Caso, Orin I Dahl, Giancarlo D'Ambrosio, et al. Review of particle physics. *Journal of Physics G: Nuclear and Particle Physics*, 33(1):001, 2006.

[Zec13] G. Zech. Iterative unfolding with Richardson-Lucy algorithm. *Nuclear Instruments and Methods in Physics Research A*, 716:1–9, 2013.

[ZZB10] J.F. Ziegler, M.D. Ziegler, and J.P. Biersack. SRIM - the stopping and range of ions in matter (2010). *Nuclear Instruments and Methods in Physics Research B*, 268:1818–1823, 2010.